Title
Understanding ultrafast magnetization dynamics in magnetic thin films

Author
Jeppson, Spencer David

Publication Date
2022

Peer reviewed|Thesis/dissertation

Understanding ultrafast magnetization dynamics in magnetic thin films

By

SPENCER JEPPSON
THESIS

Submitted in partial satisfaction of the requirements for the degree of

MASTER OF SCIENCE

in

Materials Science and Engineering

in the

OFFICE OF GRADUATE STUDIES

of the

UNIVERSITY OF CALIFORNIA

DAVIS

Approved:

Roopali Kukreja, Chair

Yayoi Takamura

Jeremy Mason

Committee in Charge

2022

Abstract

The ability to manipulate magnetic properties over ultrafast timescales has great potential for applications in magnetic memory and spintronic devices. Advances in pump-probe spectroscopy have enabled the excitation and observation of magnetization dynamics on femtosecond to picosecond timescales in a variety of magnetic materials, including ferromagnets and complex oxides. However, an understanding of the underlying physical processes and mechanisms that govern magnetism at ultrafast timescales remains a challenge. In this thesis, I studied the magnetization dynamics of epitaxial and amorphous Fe thin films excited by an ultrafast THz pump and simulated these dynamics with a Landau-Lifshitz-Gilbert (LLG) model. The dynamics of the Fe films were found to be independent of the film crystallinity. Both epitaxial and amorphous films showed a magnetization response that was coherent with the field of the THz pulse with no demagnetization observed at longer timescales. This behavior was modeled using an overdamped LLG equation. The observed dynamics were found to be dependent on the THz pulse properties rather than the crystallinity of the films. I also investigated the dynamics of a complex oxide $La_{0.7}Sr_{o.3}CoO_3$ (LSCO) thin film with optical pump-probe spectroscopy across its ferromagnetic to paramagnetic phase transition at 200 K. For LSCO, a similar ultrafast response in both the ferromagnetic and paramagnetic phases was observed. An oscillating component in optical reflectivity was also observed which was attributed to either an acoustic phonon or polariton-phonon mode. However, as the temperature of the film approached the Curie temperature, the relaxation timescales of the film increased dramatically, indicating a slowing down of spin-lattice relaxation processes. These studies highlight the complex behavior observed following excitation in metallic heterostructures and correlated oxides at ultrafast timescales.

Acknowledgements

I first of all must give a huge thank you to my advisor, Roopali Kukreja, for her expert guidance throughout my master's program. She was a constant source of knowledge and new ideas and she helped me adapt my experiments during the uncertainty of the COVID-19 pandemic. This project would not have been possible without her. Likewise, I would like to thank the members of the Kukreja group who assisted in my experimental work and education. The THz work especially was driven by the experimental work done by Rahul Jangid and Meera, and I would still be lost in the optics lab without the help of Saeed Yousefi and Scott Smith. Jugal Mehta was also instrumental in the collection of static data for each of the samples in this thesis.

I owe my gratitude to the other members of my thesis committee, Dr. Yayoi Takamura and Dr. Jeremy Mason as well. Their feedback was extremely useful in helping me think about my research from different perspectives and in communicating my thoughts clearly. Their comments have greatly improved the quality of my writing and the presentation of the data in this thesis.

Finally, I would like to thank my family for their support throughout the entire process of working on my degree. They helped keep me afloat whenever the going got tough.

Table of Contents

Chapter 1

Introduction

Magnetic materials play a critical role in modern data storage technology and memory devices. In these devices, electron spin is used as a logical bit for data storage i.e., in hard disk drives (HDD) or computing i.e., in magnetic random access memory (MRAM). For example, information stored on HDD used in data centers consists of magnetic bits, whose magnetic orientation determines the value of the bit (1 or 0). The alignment of the magnetism within a bit can be determined using a read-head which tracks the magnetic field produced by this bit, allowing data to be read in a HDD. The application of a magnetic field to these magnetic bits can also flip the direction of their magnetization, allowing data to be written. In the past two decades, it has been shown that magnetic bits can be also controlled via spin-polarized currents via spin transfer torque (STT). In this case, electric current traversing through a magnetic layer gets spin filtered due to the difference in conductance for minority (spin down) and majority (spin up) electrons. This spin-polarized current can result in switching of a thin magnetic layer by applying a magnetic torque to the magnetic layer which has been dubbed STT [1, 2]. The emergence of electrical control of magnetization has paved the way for non-volatile MRAM. Everspin have developed one of the first MRAMs and is currently developing MRAM with 1 GB storage size [3]. However, the timescales of magetization switching by spin-polarized currents is limited to 100's picoseconds (ps) to nanoseconds (ns) [4]

Recently, optical laser manipulation of magnetic materials has emerged as a unique way to access and control spin at femtosecond (fs) timescales. Using ultrafast infrared laser pulses, it has been shown that a magnetic material undergoes demagnetization (loss of magnetization) within $\approx$100 fs, 3-4 orders of magnitude faster than current devices. In these studies, ultrafast magnetization dynamics has been induced by pumping a system with an ultrashort pulse of energy such as laser excitation. This pulse causes rapid changes in the electronic and magnetic, as well as structural state of the material. Additionally, at such ultrafast timescales,

magnetic materials can exhibit far-from equilibrium properties that are not observed in more conventional measurements. However, in spite of a decade of experimental and theoretical exploration, the microscopic mechanism underlying magnetization dynamics is still debated and there is no consensus in the magnetism community over key questions such as: what is the mechanism through which a magnetic system can dissipate angular momentum at such fast timescales (100 fs) and what are the recovery processes involved? Is the excitation limited to optical frequencies or can other frequencies such as terahertz (THz) be used to induce magnetization dynamics and spin reversal?

A significant amount of research has been performed in the past two decades to answer some of these questions. The dynamics observed at ultrafast timescales are often described by quasi-particle interactions. For instance, upon pumping a semiconductor with greater-than-bandgap light, electrons can be moved from the valence band to the conduction band. This process creates a quasi-particle known as an exciton, which describes the interaction between an electron-hole pair. Laser-excited electrons in a crystalline material can interact with the lattice, releasing their energy as a phonon, or coherent vibration of the atoms within the lattice. However, these excited states can only be measured by techniques that have sufficient time-resolution to capture the behavior before the system relaxes back to a stable ground state. Thus, a variety of optical or x-ray pump-probe techniques have been developed to investigate magnetization behavior at fs-ps timescales. In pump-probe studies, experiments are performed in a time-resolved manner where a "pump" is used to excite the sample and a "probe" is used to measure the magnetic response of the sample. The pump laser is typically a near-infrared fs laser pulse (800 nm), which excites the magnetization dynamics, and the probe is a weaker fs optical or x-ray pulse to measure the sample behavior. The experiment is conducted stroboscopically, and the time delay between the pump and probe pulse is varied to map out material behavior as a function of time. Due to the stroboscopic nature of the technique, materials studied in pump-probe experiments must exhibit fully reversible dynamics, as the system must return to equilibrium before the subsequent pump pulse arrives. The temporal resolution of the experiment is limited by the pulse width of the probe and pump pulse, and thus, a shorter pulse width is critical for accessing fs timescales of electron–electron, electron–phonon, and electron–magnon coupling.

The ability to understand and control the magnetic behavior of a material on an ultrafast timescale may lead to the development of new devices with significantly greater operation speed than currently possible. For instance, the ability to switch magnetic states on an ultrafast timescale using lasers could lead to much faster read and write times resulting in the development of next generation computing devices. In this thesis, I will focus on understanding laser-induced dynamics in magnetic materials including metallic thin films and complex oxides such as perovskites.

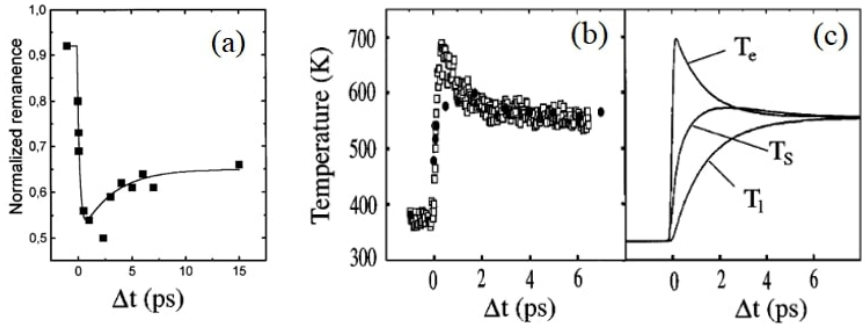

Figure 1.1: Optically-induced ultrafast demagnetization: a) The first observation of ultrafast demagnetization of a Ni thin film. About 60% of the magnetic moment is lost within 2 ps. b) Experimentally measured spin (solid dots) and electron (open squares) temperatures compared to those determined experimentally c) by the three temperature model. Here, T_e is the electron temperature, T_s is the spin temperature, and T_l is the lattice temperature [5].

1.1 Ultrafast magnetization dynamics

The field of ultrafast manipulation of magnetization began when Beaurepaire *et al.* [5] observed a rapid loss of magnetization within a ps, followed by a slower relaxation back to the initial magnetization state for a Ni thin film after pumping with an ultrashort near infrared (NIR) laser pulse (Figure 1.1). The loss of magnetization and subsequent recovery process was described using three temperature model. The ultrafast decrease in magnetization was attributed to an ultrafast heating of the electron system, which transferred energy to the spin system, causing it to transiently rise above the Curie temperature. The slow relaxation and increase in magnetic moment was associated with transfer of energy from the spin-system to the lattice system. The ultrafast decrease in magnetization followed by slow recovery was later observed in a variety of metallic ferromagnets and ferrimagnets of many chemical compositions [6, 7, 8, 9, 10, 11]. Furthermore, in 2007, all optical magnetic switching was reported in GdFeCo ferrimagnetic thin films [12] where optical pulses were used to reverse the magnetization direction of the thin film. Since 2007, all optical switching has since been shown on other materials such as TbCo [13] and FePt [14, 15].

However, for both ultrafast demagnetization and all optical switching, several challenges remain in elucidating the fundamental physical mechanisms behind these processes. For instance, current debate exists as to whether ultrafast demagnetization and all optical switching are caused by direct excitation of the material by the electric field of the laser or indirectly by the rapid heating caused by absorption of the laser energy. Questions also remain about the flow of angular momentum within the material during ultrafast demagnetization. Mechanisms involving electron-phonon spin-flip scattering [16, 17] and superdiffusive spin currents [18, 19] have been proposed. In the spin-flip scattering mechanism, hot electrons and phonons which have been excited by the laser pump interact, causing the spin of the electron to flip, transferring angular

momentum into the lattice of the material. Superdiffusive spin currents are caused by the laser pulse creating a spin-polarized current within the system, which drives spin-polarized electrons deeper into the material, causing the observed demagnetization. The choice of material system also seems to influence the observed mechanisms of ultrafast demagnetization.

While optical pump-probe techniques have been the most widely employed to study these phenomena, new methods to control magnetization as well as new techniques to study unique aspects of ultrafast magnetization dynamics are being continuously developed. On the technique side, the advent of x-ray free-electron lasers and tabletop high-harmonic generation sources have allowed the generation of intense, tunable, and ultrashort x-ray and extreme ultraviolet pulses. These pulses offer unique advantages in the study of ultrafast magnetization dynamics due to their ability to distinguish between the magnetic dynamics of each element within multi-element systems, such as alloys and multilayers. In addition to high-temporal resolution, ultrashort x-ray pulses also give access to nanometer spatial resolutions because of their short wavelengths. These advances open the door to coherent magnetic imaging and magnetic x-ray scattering techniques to measure the spatial and temporal evolution of magnetization at ultrashort and ultrafast frontier. While this thesis does not consider such x-ray probes, the reader is directed to a recent review I authored for a more detailed overview of the field [20].

1.2 THz-driven magnetization dynamics

In the laser manipulation of magnetic materials, optical pulses in NIR regime have been most commonly employed. While ultrashort optical pulses are a powerful tool for driving ultrafast dynamics in magnetic materials, they also cause significant heating within the material. This becomes an issue for potential device applications as the temperature increase of the system relaxes over a relatively slow timescale compared to the excitation, limiting the frequency at which these dynamics can be exploited for applications. An emerging method to control ultrafast magnetization dynamics is pumping the system with an ultrashort THz pulse. THz radiation is electromagnetic radiation with a frequency in the 100s of GHz to 10 THz. Previously, the lack of THz radiation sources had strongly limited the field of THz excitation and spectroscopy. However, recently, nonlinear processes have been used to generate single-cycle THz pulses to bring THz radiation to the ultrafast domain for pump-probe studies.

The development of single and few-cycle THz pulses has been used to drive coherent magnetization dynamics over few ps timescales. A few studies have shown that the intense B-field of these THz pulses can modulate the magnetization of thin ferromagnetic films. THz pulses offer unique insights into magnetization at such fast timescales due to the fact that THz radiation is not resonant with vibrations within the

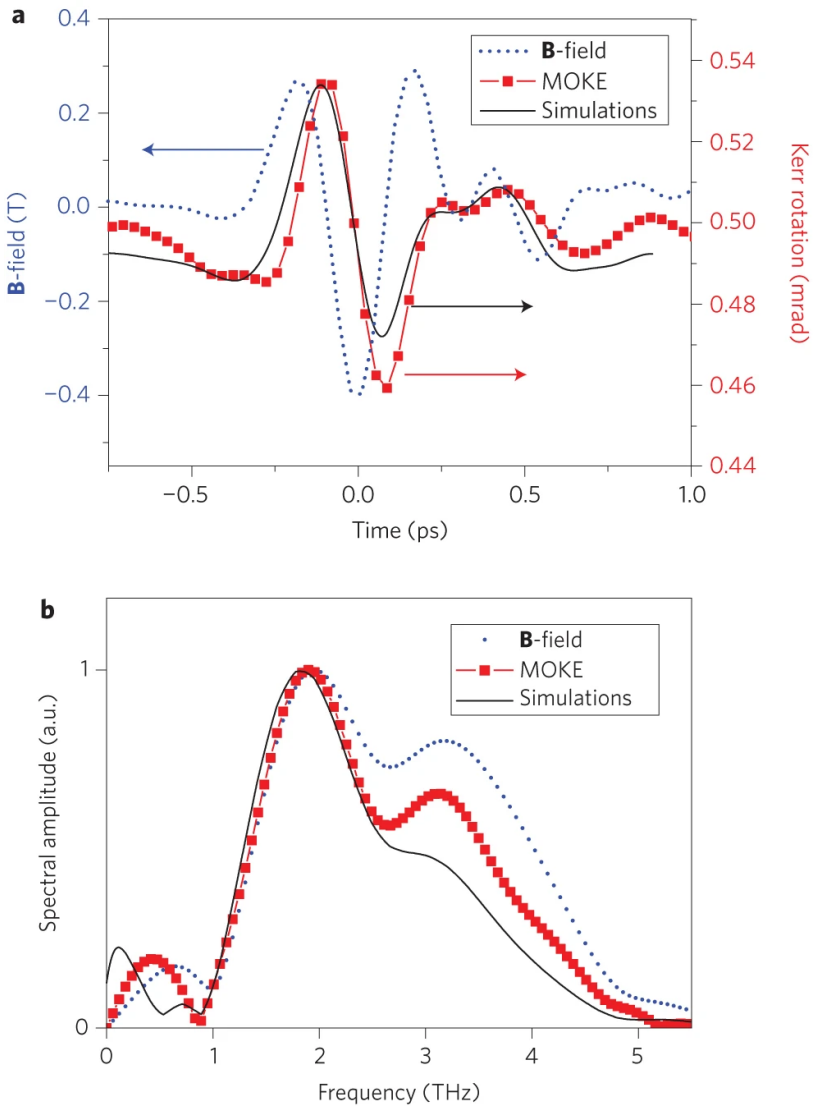

Figure 1.2: Ultrafast THz-induced magnetization dynamics in a Co thin film: a.) Ultrafast magnetization dynamics of a thin Co film pumped with an ultrashort THz pulse are measured by time-resolved magneto-optic Kerr effect spectroscopy. The magnetization is considered coherent, or phase-locked, to the THz pulse as the response closely follows the shape of the THz field, although it is offset by a small time delay. b.) A fourier transform analysis of the THz pulse and the magnetization response show that they share very similar frequency components, indicating the coherent nature of the dynamics [21].

material, resulting in very little absorption-caused thermal effects in the dynamics. This is in contrast to optically-pumped magnetic systems, where strong absorption causes significant increase in temperature >100 K resulting in thermally-driven dynamics. A study performed by Vicario *et al.* on a thin Co film showed that a single-cycle THz pulse with a B-field intensity of 0.4 T can drive magnetization dynamics phase-locked to the THz field [21]. Other studies have shown THz-pump induced demagnetization in FeCoB [22, 23] and CoPt [24] with B-field strengths as low as 0.1 T. The lack of heating observed in these system during the THz pulse has generated significant interest in understanding physical processes underlying magnetization dynamics following THz excitation. This lack of heating coupled with the observation of the coherent nature of the excitation of magnetization with the THz B-field, makes these dynamics of great interest for future spintronic devices requiring rapid and reversible control of magnetization.

Vicario *et al.* [21] were the first to observe magnetization dynamics excited by a strong, single-cycle THz pulse. They observed that the magnetization of a 10 nm thick Co film was influenced by this THz pump in a phase-locked or coherent manner. This means that the dynamics were driven not by the pulse envelope, but by the field of the pulse itself, with the magnetization direction moving with the peaks and troughs of the electromagnetic field as seen in Figure 1.2. This behavior is in contrast to optical excitation of magnetic materials, where the dynamics appear to be principally driven by the energy delivered by the pulse envelope. This coherent evolution of magnetization in metallic thin films pumped with ultrashort THz pulse has since been observed in several other ferromagnetic systems [22, 23, 24].

However, several substantial gaps in our fundamental understanding of THz-driven magnetization dynamics remain that must be addressed before such processes can be put to practical use. For instance, while ultrashort THz pulses have been shown to coherently excite magnetization in ferromagnetic metals, questions remain as to how these dynamics can be controlled, and what causes demagnetization to be observed in some studies, and not in other studies. Vicario *et al.* [21] did not observe demagnetization while measuring magnetization dynamics in Co thin films following THz excitation. On the other hand, Bonetti *et al.* [22] only observed demagnetization in amorphous FeCoB, but not in crystalline Fe films. It should be noted that Vicario *et al.* [21] used a stronger THz field than Bonetti *et al.* [22] but still didn't observe demagnetization. Thus, the observation of demagnetization in amorphous FeCoB [22, 23] and CoPt [24] even at lower THz fields could be related to either composition or crystallinity of the sample. However, the effect of crystallinity without changing the chemical identity of the sample has not yet been explored.

In this thesis, I will consider the effect of crystallinity on the THz-pumped magnetization dynamics of Fe thin films. I will compare the behavior of both amorphous and crystalline Fe thin films both experimentally and theoretically. THz-driven dynamics in amorphous and crystalline Fe thin films were experimentally measured in collaboration with Rahul Jangid and Meera in the Kukreja group and Dr. Matthias Hoffman

at SLAC National Accelerator Laboratory (SLAC). I developed micromagnetic simulations to theoretically obtain THz-driven behavior in Fe thin films and compared them with the experimentally measured behavior at SLAC.

1.3 Micromagnetic simulations

Theoretical modeling of magnetic materials typically falls under two different methods. Atomistic simulations which account for the spin of each magnetic atom, or phenomonological micromagnetic models, which divides magnetic moments into discrete cells which interact only with the magnetic moments of the other cells in the system and external magnetic fields. Atomistic models such as spin density functional theory are useful for gaining insight on magnetization processes at the atomic level, whereas micromagnetic simulations are advantageous for studying systems larger than a few nanometers in any direction. Phenomonological micromagnetic models are usually based on the Landau-Lifshitz(LL) or Landau-Lifhsitz Gilbert (LLG) equation. The LL equation is used to describe magnetic precession and damping, and is given by

$$\frac{d\mathbf{m}}{dt} = \underbrace{\gamma(\mathbf{m} \times \mathbf{H})}_{precession} + \underbrace{\frac{\alpha\gamma}{m}[\mathbf{m} \times (\mathbf{m} \times \mathbf{H})]}_{damping} \tag{1.1}$$

with $\mathbf{m}$ being the magnetic moment vector, $\mathbf{H}$ is the effective field, γ is the gyromagnetic ratio of a free electron (-1.76×10^{11} rad/sT), α is a unitless damping parameter, and m is equal to the magnitude of the magnetization vector [25]. The first term on the right-hand side of this equation describes the precession of the magnetic moments about the effective field. The second term describes the damping, or relaxation of the moments towards that field. Figure 1.3 illustrates the dynamics given by the LL equation. This was the first equation to describe magnetic precession and damping dynamics. However, an analysis by Gilbert and Kelly on eddy currents in thin ferromagnetic sheets produced a similar equation for describing these dynamics, which is now known as the LLG equation [26, 27] and is given by,

$$(1 + \alpha^2)\frac{d\mathbf{m}}{dt} = \gamma(\mathbf{m} \times \mathbf{H}) + \frac{\alpha\gamma}{m}[\mathbf{m} \times (\mathbf{m} \times \mathbf{H})] \tag{1.2}$$

At low values of α, these equations yield similar results; however, as the damping increases, they diverge substantially. Micromagnetic simulations typically use the LLG equation. There are several well-tested open source software packages, such as OOMMF, Ubermag, Mumax, and Fidimag based on the LLG equation. Both the LL and LLG equation have been extremely effective in predicting magnetization dynamics and magnetic textures on the typical timescale of ferromagnetic precession (hundreds of ps - ns.)

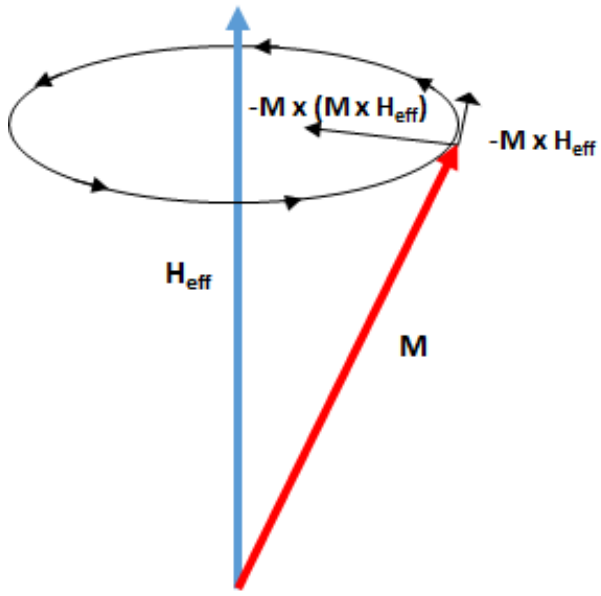

Figure 1.3: Illustration of LL motion: The LL equation describes dynamics of a magnetic moment about an effective field. The blue arrow is the effective field and the red arrow is the magnetic moment. The (first) precession term of the LL equation causes the moment to rotate around the effective field, while the (second) damping term describes the motion of the moment towards the field. Note that the direction of precession and damping term are opposite to the cross product direction because of the negative sign of the gyromagnetic ratio of an electron (γ).

In recent years, micromagnetic simulations have expanded beyond the LL and LLG equation in order to model phenomena that are not well described within the boundaries of this model. For instance, the LLG equation assumes a fixed magnitude of the magnetic moment of each cell, implying that optical laser-driven ultrafast demagnetization which decreases the magnitude of magnetic moment cannot be modeled. In this scenario, Landau-Lifshitz-Bloch (LLB) equation has been developed, which can be used to model laser-driven ultrafast demagnetization observed in magnetic metals [28, 29, 30] and some oxides [31, 32]. In the LLB equation, an additional temperature-dependent term for longitudinal magnetic relaxation is added. This term when coupled to a two-temperature model with the electron and lattice temperatures, laser-induced demagnetization in magnetic metals can successfully be modeled.

Modifications to the LL and LLG equation have also been introduced to model dynamics observed under intense, single-cycle THz pulses. For instance, THz-induced demagnetization has been modeled by including a similar longitudinal relaxation term as the LLB equation, but dependent on the THz field strength rather than temperature [23]. Another example is a modification to include an inertial term for modeling the ultrafast dynamics observed after THz pumping [33]. THz pump induced magnetization dynamics have also been modeled by overdamping the LL equation when the magnetization is perpendicular to the THz

B-field [34]. These modifications to the LLG equation to simulate THz behavior are still in the very early stages of development. The fundamental understanding underlying these modifications as well as which modification should be applied based on experimental or sample conditions are still not clear. The addition of the longitudinal relaxation term [23] results in demagnetization of the system. In this thesis, we focused primarily on an overdamped LLG equation, which was used to model THz response when no demagnetizaton was observed in experimental studies. Similar adaptation of the LLG equation has been used to closely model the coherent dynamics observed in ferromagnetic metals pumped with ultrashort THz pulses [21, 22]. A further discussion of the micromagnetic methods used to model the THz magnetization dynamics of Fe thin films is given in Chapter 2.

1.4 Ultrafast control of complex oxides

The ability to rapidly trigger a phase transition in complex oxide materials is also very attractive for future sensors and memory devices. In complex oxides, a metal-insulator transition where the conductivity changes by orders of magnitude or a ferromagnetic-paramagnetic transition in response to a trigger provide attractive candidates for future oxide electronics. In these correlated systems, charge, spin, orbital, and lattice degrees of freedom have competing interactions resulting in an extremely rich phase diagram with novel functional properties such as superconductivity, ferromagnetism, and antiferromagnetism. These functionalities in competing ground states can be utilized as an ON-OFF switch through a laser excitation at ultrafast timescales. For instance, an optically-driven metal-insulator transition in VO_2 has been studied at ultrafast timescales, with potential applications in memory devices [35, 36] (see Figure 1.4). Similarly, the speed at which the magnetic state of a material can be modified plays a key role in determining the speed of future spintronic devices [37]. Ultrafast optical pulses can trigger these dynamics on much faster timescales than other external stimuli, and have therefore been utilized to understand the fundamental dynamics and mechanisms at play during such transitions. In addition, laser absorption not only heats a system, but the electric field of the laser can directly interact with the electrons in a material, giving rise to thermally inaccessible states that may have properties unique from equilibrium phases. Thus, laser-driven behavior of complex oxides offers a rich field to explore and understand the competing interactions and dynamics associated with it. In the second part of this thesis, I will focus on understanding optical laser-driven behavior of perovskite cobaltite thin films across its ferromagnetic-paramagnetic phase transition.

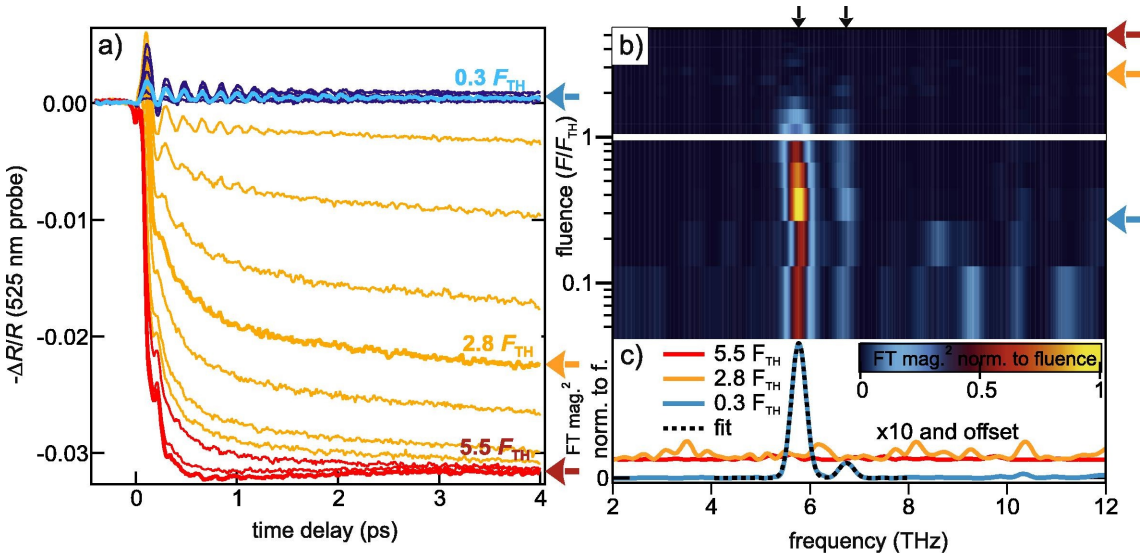

Figure 1.4: The ultrafast dynamics of the metal-insulator phase transition in VO_2: a) the transient reflectivity of VO_2 as a function of pump fluence relative to the phase transition threshold fluence, F_{TH}. A clear decrease in reflectivity can be seen as the VO_2 transitions from the insulating to metallic phase, once the fluence passes the threshold. b) The transient reflectivity of VO_2 below F_{TH} shows a coherent phonon mode present in insulating VO_2 that disappears when the material transitions to the metallic state. c) The fourier transform of specific pump fluences above and below F_{TH}. For those below, the coherent phonon modes can be fit with a two-gaussian function. The blue, yellow, and red arrows on each figure represent the dynamics observed at 0.3, 2.8, and 5.5 times F_{TH}. These figures are from experiments done by Wegkamp *et al.* [36]

1.4.1 Perovskite oxides and $La_xSr_{1-x}CoO_3$

Perovskite oxides are a class of materials with the general chemical formula ABO_3, in which A and B are generally metallic elements. The A cation occupies the corners of the unit cell, with the B cation in the center of the cell and the oxygen anions on the face centers (Figure 1.5.) Perovskite oxides have been the subject of significant research interest as they are strongly correlated systems, meaning there is significant overlap between the charge, orbital, spin, and lattice degrees of freedom. This means that changes in one of these degrees of freedom will often result in changes of one or more of the others. Strongly correlated systems often have unique properties that may be useful for implementation in future devices. For example, one of the most widely studied perovskite oxides is $LaMnO_3$, which when doped with $CaMnO_3$, $BaMnO_3$, or $SrMnO_3$, exhibits colossal magnetoresistance (CMR). CMR effects refers to a strong influence of electrical resistance caused by magnetization in a material (coupling between spin and charge [38].)

The strong interest in CMR has lead to significant investigation of the lanthanum manganites, however, a related class of materials, the lanthanum cobaltites, such as $La_{1-x}Sr_xCoO_3$ (LSCO), have received significantly less attention. LSCO is a perovskite oxide which has been investigated for its interesting spin states and electronic-spin state transitions [40] as well as high oxygen ion mobility [41, 42]. Most notable among

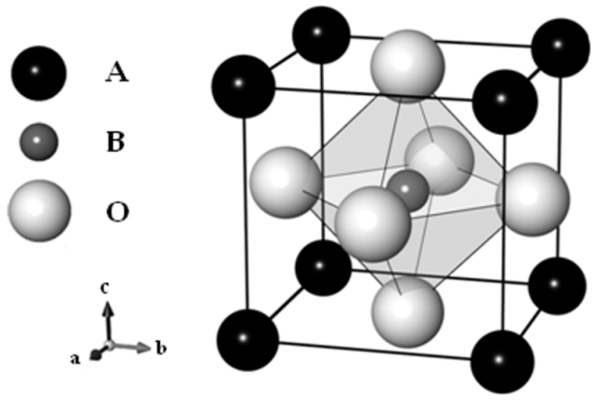

Figure 1.5: The crystal structure of perovskite oxides: A and B are metal cations, and O are the oxygen anions [39].

the spin state transitions is the transition between a spin glass state at low Sr doping concentrations to a ferromagnetic state at higher doping (percolated ferromagnetic state). The presence of several unique spin states is attributed to the small splitting between the Co t_{2g} and e_g levels [43, 44]. In this thesis, LSCO with a composition of $La_{0.7}Sr_{0.3}CoO_3$ will be investigated. This composition exhibits a transition from a ferromagnetic metallic state to a paramagnetic semiconductor state near 200 K in bulk (see Figure 1.6). In this thesis, epitaxial LSCO thin films were studied which might slightly differ from bulk in terms of transition temperature due to size effects and lattice strain.

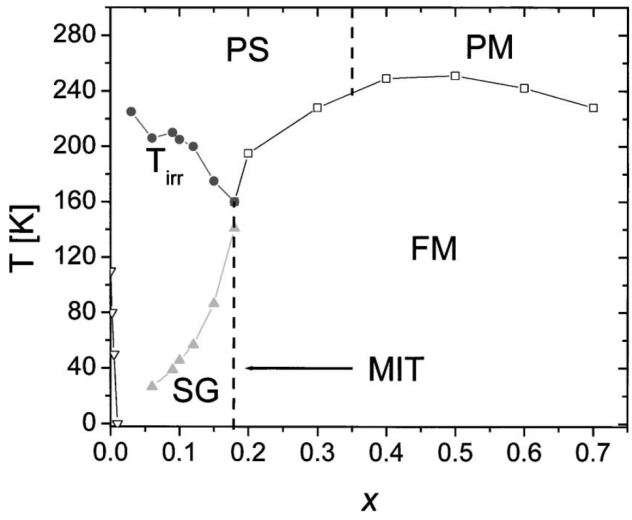

Figure 1.6: Phase diagram for bulk $La_{1-x}Sr_xCoO_3$: The phases of LSCO are given as a function of Sr concentration and temperature, as determined by Wu et al [40]. The composition that will be considered in this thesis is x = 0.3, which exhibits a ferromagnetic metal (FM) to paramagnetic semiconductor (PS) transition near 220K in bulk. The other phases shown are paramagnetic metal (PM) and spin glass (SG). MIT refers to the metal to insulator transition, PM stands for paramagnetic metal and T_{irr} indicates the irreversible temperature below which the spin glass state can exist.

In LSCO, the variable concentration of Sr atoms (as shown in 1.6) leads to systems with a wide array of differing electronic, magnetic properties and spin-state transitions. However, many of these effects have not been explored at ultrafast timescales. While systems like vanadates [35, 36], manganites [45, 46], nickelates [47, 48, 49] and magnetite [50] have been explored using optical/x-ray pump-probe, until now no studies have been performed on LSCO to investigate the evolution of magnetic and electronic degrees of freedom at fs-ps timescales. In this thesis, I focus on performing optical pump-probe studies on an LSCO thin film to study the evolution of the ferromagnetic and paramagnetic phases following optical laser excitation. This allowed us to characterize the fundamental timescales associated with the excitation and recovery of electronic and magnetic degrees of freedom in cobaltites.

The layout of this thesis is as follows. Chapter 2 details the experimental and modeling techniques used to investigate THz-driven magnetization dynamics in magnetic multilayers and optically-driven behavior in LSCO. Chapter 3 discusses the results of micromagnetic simulations of single-crystal and amorphous Fe films pumped by single-cycle THz pulses and compares them to experimental results. Chapter 4 presents optical pump studies on the magnetic phase transition in $La_{0.7}Sr_{0.3}CoO_3$ in the fs-ps regime. Chapter 5 contains a summary and conclusion, as well as an overview of potential future experiments that could be performed on these systems to further understand ultrafast behavior of electronic and magnetic degrees of freedom.

Chapter 2

Methods and techniques

This chapter focuses on the experimental and theoretical techniques utilized in this thesis to study the dynamics of magnetic materials at the ultrafast timescale. First, an overview of magnetic characterization and pump-probe techniques used to study ultrafast dynamics is provided, with an explanation of the different sources for pumps and probes and the advantages and unique capabilities of each. Next, more details about the specific techniques used in this thesis including optical pump-probe transient reflectivity and THz-pump optical probe magneto-optic Kerr effect (MOKE) spectroscopy will be given, along with a description of the experimental setup. Finally, a description of micromagnetic finite difference simulations, which were used to study magnetization dynamics in single-crystsal and amorphous Fe thin films, is discussed.

2.1 Magnetic characterization using vibrating sample magnetometry

Vibrating sample magnetometry (VSM) was used to determine the magnetic properties of the Fe and LSCO thin films. Magnetization as a function of applied field (hysteresis loops) and magnetization as a function of temperature were collected using a VSM. An example of a hysteresis loop for an amorphous Fe thin film is shown in Figure 2.1 which allows us to measure remnant magnetizaton, saturation magnetization and coercive field. Ferromagnetic materials exhibit a remnant magnetization after being exposed to a magnetic field. Saturation magnetization refers to highest degree of magnetization achieved by ferromagnetic material. Coercive field is the field required to switch the direction of the magnetization. In this thesis, both Fe films were soft magnetic thin films, with very low coercivities. Coercivity relates to the magnetic "hardness" of the materials. In magnetic read heads, for example, an antiferromagnetic film is used to maintain magnetism

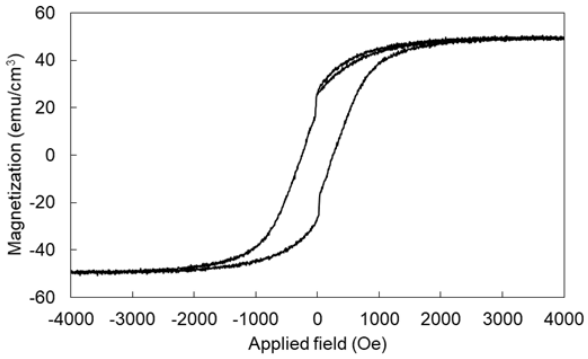

Figure 2.1: Hysteresis loop of a 50 nm amorphous Fe thin film: This M vs H curve was collected using VSM. The maximum magnetization achieved by the sample occurs at the saturation field. The applied field at which the magnetization is zero is known as the coercive field.

in a certain direction by exchange bias, and a soft magnetic material is used to read the memory by flipping its moment to align with that of the nearest bit. The relative orientation of the pinned layer and soft the soft film is then exploited to determine the orientation of the bit. In our case, lower coercivity films were grown to investigate if THz field is able to switch the magnetization direction. For LSCO, magnetization vs temperature measurements were performed to determine the temperatures associated with magnetic state transitions. As the temperature is varied, the magnetization of a material will begin to change if it undergoes a magnetic phase transition. Thus, magnetization vs temperature curves can be used to determine the temperature at which such a phase transition occurs.

2.2 Pump-probe techniques

Pump-probe or time-resolved techniques are required to measure dynamics at ultrafast timescales (fs-ps.) These timescales are beyond the range of typical electronics (such as lock-in amplifier or GHz oscilloscope) to measure, and thus require special setup for both exciting the sample as well as measuring the excited state of the sample. One of the key requirements is high temporal resolution in 10-50's fs along with the ability to probe electronic and magnetic behavior. Optical pump-probe techniques have been established to measure ultrafast dynamics. Optical pump-probe techniques involve two optical pulses, a pump and a probe, offset by a certain time delay. A schematic of the setup is shown in Figure 2.2. The pump pulse (optical laser, THz etc.) is used to excite a sample and the probe pulse (typically a weaker optical pulse) is used to measure a certain parameter (such as reflectivity) of the system. The time delay between the pump and probe is determined by the difference in path length between the two pulses, and can be adjusted by changing the path length of the probe pulse. In order to obtain a delay curve (reflectivity vs time delay)

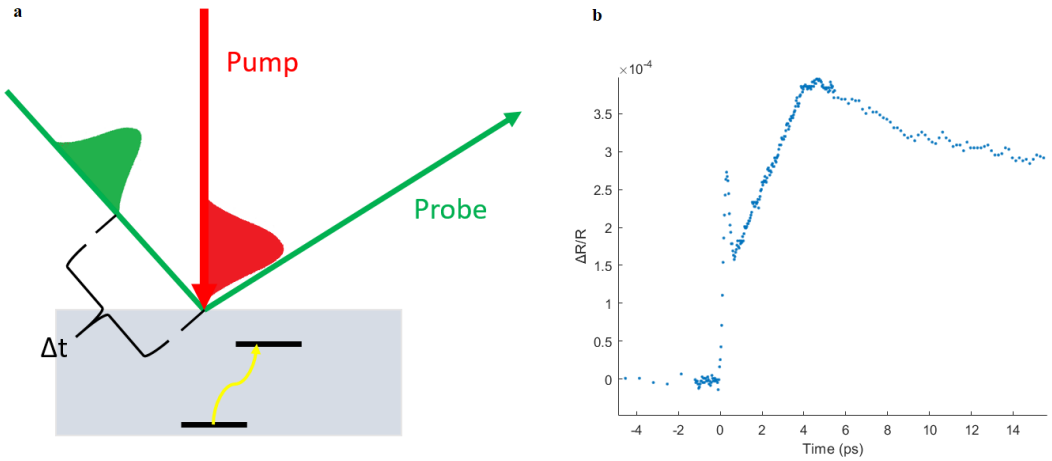

Figure 2.2: pump-probe technique for measuring ultrafast dynamics: a) A pump pulse (red) is incident on a sample to excite dynamics, and a probe pulse (green) arrives at a certain time delay, determined by the difference in path length between the probe and pump. The probe pulse is then measured after interacting with the sample to collect information about that time delay. The time delay can then be varied, so as to collect time-resolved dynamics of the system. b) Transient reflectivity of LSCO collected by optical pump-probe spectroscopy. Each point represents the average reflection of the probe pulse at a certain time delay relative to the pump pulse.

such as shown in Figure 2.2(b), a time delay between pump and probe is chosen (such as 2 ps), and pump and probe are stroboscopically pulsed and information from the probe pulse is averaged over a period of time (i.e., milliseconds to seconds) to achieve high signal to noise ratio. Then, a second time delay between pump and probe is chosen (i.e., 3 ps), and same process is repeated. In this manner, a series of information at different time delays is collected and put together to map out the evolution of the sample as a function of time delay. As mentioned in Chapter 1, it is important for the material dynamics to be reversible within the timescale of subsequent pump pulses. The temporal resolution of the experiment is determined by the convolution of pulse width of optical pump and probe pulses which is typically around 50 fs, resulting in a resolution of 70-100 fs.

In a typical optical pump-probe setup, a pump pulse in the optical regime with a wavelength of 800 nm is used along with a weaker probe pulse of the same wavelength or frequency-doubled i.e., 400 nm. However, in recent years, a variety of pump and probe wavelengths have been developed to selectively excite and probe a certain type of behavior. Examples of pump wavelengths include THz excitation which results in minimal heating or using mid infrared pulses to selectively excite certain phonon modes in complex oxides. Similarly, a variety of probe methods have been developed to measured electronic behavior using optical reflectivity or x-ray spectroscopy, as well as magnetic behavior such as magneto-optic Kerr effect (MOKE) or magnetic circular dichroism.

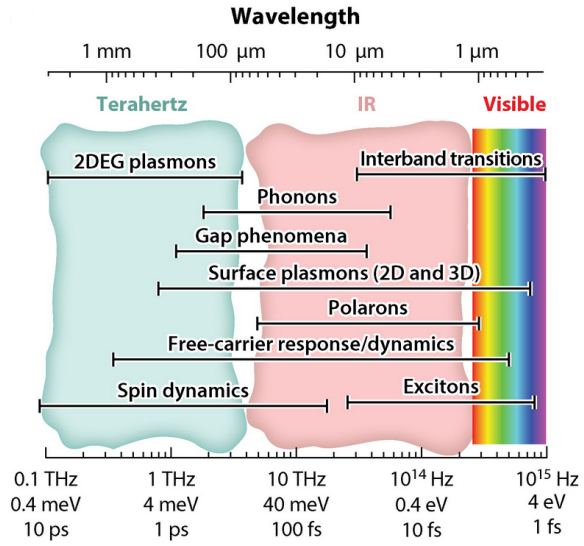

Figure 2.3: Fundamental excitations in materials and the pump wavelengths used to access them [51]: In this thesis, both NIR and THz pumps are considered.

2.2.1 Pumping schemes: types of pump wavelengths

Figure 2.3 shows a variety of pump wavelengths which have been used to excite fundamental excitations in materials. In this thesis, I will focus on two different pumping regimes: optical and THz. Ultrafast optical pumps are generally Ti:sapphire laser systems. Ti:sapphire laser was used in this thesis to generate 800 nm pump wavelength. It was chosen as it has a large and tunable bandwidth, which allows for generation of pulses as fast as a few fs. Such ultrashort pulses are critical for pump-probe techniques as they allow for precise timing of the delay between the pump and probe pulses. The central wavelength of a Ti:sapphire laser pulse is generally around 800 nm, corresponding to the NIR spectrum, however, this can be modified with optical parametric amplification (OPA) to produce pulses with optical or ultraviolet wavelengths. Optical pulses are primarily used for exciting electronic and magnetic transitions in the valence band of a material, which in turn can also cause significant thermal effects. In this thesis, optical pump was used to excite dynamics in LSCO thin films.

THz radiation is a relatively new type of pump pulse. THz generation is typically achieved by optical rectification of fs laser pulses which results in a single-cycle pulse of broadband THz radiation with an electric field peak intensity in the MV/cm range. Optical rectification is a non-linear optical process whereby intense optical light is incident in a non-centrosymmetric crystal resulting in difference-frequency generation i.e., THz emission. If the beam is fully monochromatic, a DC current is generated, however, if the light is sufficiently broadband, as in an ultrashort pulse, then the small differences in frequency results in an ultrashort pulse with frequencies in the THz range. These THz pulses are distinct from ultrashort optical pulses as they

are much lower in energy and are not associated with electronic or vibrational transitions in ferromagnetic metals. Thus, THz pulses deposit little to no energy in ferromagnetic systems. The lack of absorption combined with the very high electric and magnetic fields of single cycle THz pulses implied that THz pulse can be used to coherently excited the material without heating effects playing a role. In this case, the electric or magnetic fields of the pulse excites the spin or electronic degree of freedom providing direct control over the functionalities of the sample. In this thesis, THz pump pulse was used to excite magnetization dynamics in Fe thin films.

2.2.2 Probing schemes: types of probe wavelength

The selection of the probe pulse determines the type of material behavior (electronic, magnetic or structural) studied following the excitation. A critical factor for a probe pulse is the temporal duration of the pulse, as this determines the temporal resolution of the measurement. Due to the widespread availability of ultrafast laser systems, optical pulses are the most commonly used type of probe. Optical pulses with photon energies in the range of 1-4 eV are typically used, which probes the electronic structure of a material between the valence and conduction bands. Optical pulses can be employed in a variety of ways, depending on the information desired from a material. In this thesis, optical probes are used for transient reflectivity and time-resolved MOKE. In transient reflectivity, the reflected probe pulse is measured using a detector such as a photodiode as a function of time delay. The reflectivity of the sample at different time delays can then yield dynamic information about the electronic behavior or the excited state . In strongly correlated systems such as complex oxides, this information can also be correlated to other changes in the material, such as crystal structure or spin state due to strongly coupled nature of spin, electronic and structural degrees of freedom. Optical probes can also be used to measure the evolution of magnetization in a sample via MOKE. In this case, the probe pulse is incident with a known polarization (in this thesis, p-polarized), and the polarization of the reflected pulse is measured. The rotation between the incident and reflected pulse corresponds to the magnetization of the sample. In this thesis, transient reflectivity with an optical probe is used to investigate ultrafast phase transitions in LSCO and optical MOKE measurements were performed to map out the evolution of magnetism in Fe thin films.

2.3 Optical pump-probe setup used for transient reflectivity studies of LSCO

Ultrafast transient reflectivity was used to investigate ultrafast phase transitions in LSCO thin films. Optical pump-probe transient reflectivity is a commonly used method to measure carrier dynamics in materials at ultrafast timescales (fs to ps.) In this technique, an intense, ultrashort probe pulse excites carriers from the ground state to an excited state. A probe pulse is then incident on the sample at a specific time delay. The probe pulse must be more tightly focused than the pump pulse, with a radius at the surface no greater than 1/3 the radius of the pump pulse to ensure that the dynamics measured by the probe are entirely affected by the pump. The probe pulse must also be much less intense than the pump, to ensure that it does not excite the system again and only probes the system. The time delay between the pump and probe pulses is then varied in order to collect a time-dependent delay curve. The response observed by this technique depends on the energy landscape of the material and the photon energy of the pulses.

The experimental setup (shown in Figure 2.4 consists of a Ti:sapphire oscillator (SpectraPhysics Tsunami) pumped by a Nd:YLF laser (SpectraPhysics Millenium.) The oscillator was tuned to a central wavelength of 806 nm with a pulse width of 60 fs. A 25 nm thick (001)-oriented LSCO film on a $La_{0.18}Sr_{0.82}(Al_{0.59}Ta_{0.41})O_3$ (LSAT) substrate was mounted within a cryostation (Montana Instruments). A 34 nm LSCO film was also investigated, but with no temperature dependence as it was outside of the cryostation. The initial beam is split by an 80:20 beam splitter, with the stronger beam serving as the pump. The pump beam is modulated by an optical chopper at 970 kHz and directed along a fixed pathlength towards the sample at normal incidence. The probe beam path length is varied using a retroreflector mounted on a motorized stage. The probe beam is focused onto the sample at a 20° angle. The focusing lenses for the pump and probe beams are 10 cm and 5 cm, respectively. The reflected pump beam is then collimated and refocused onto a photodiode connected to a lock-in amplifier. The lock-in amplifier is used to only detect signals that are modulated at the 970 kHz of the pump beam, allowing the relatively weak signals to be detected. Half wave plates and polarization filters are used to make the pump beam p-polarized and the probe beam s-polarized, with the p-polarized signal filtered out before the detector to minimize pump interference.

In optical pump-probe scheme, if the system being studied is semiconducting and the pump pulse photon energy is equal to or greater than the bandgap of the material, the pump can excite electrons from the ground state to an excited state. The weaker probe pulse will also cause the same excitation, but with more carriers already excited when the probe arrives, the absorption of the probe will be decreased. The Kramers-Kronig relations indicate that a decrease in absorption corresponds to a decrease in reflectivity, hence the reflectivity observed in this case will decrease at probe delays after the pump pulse. This is known

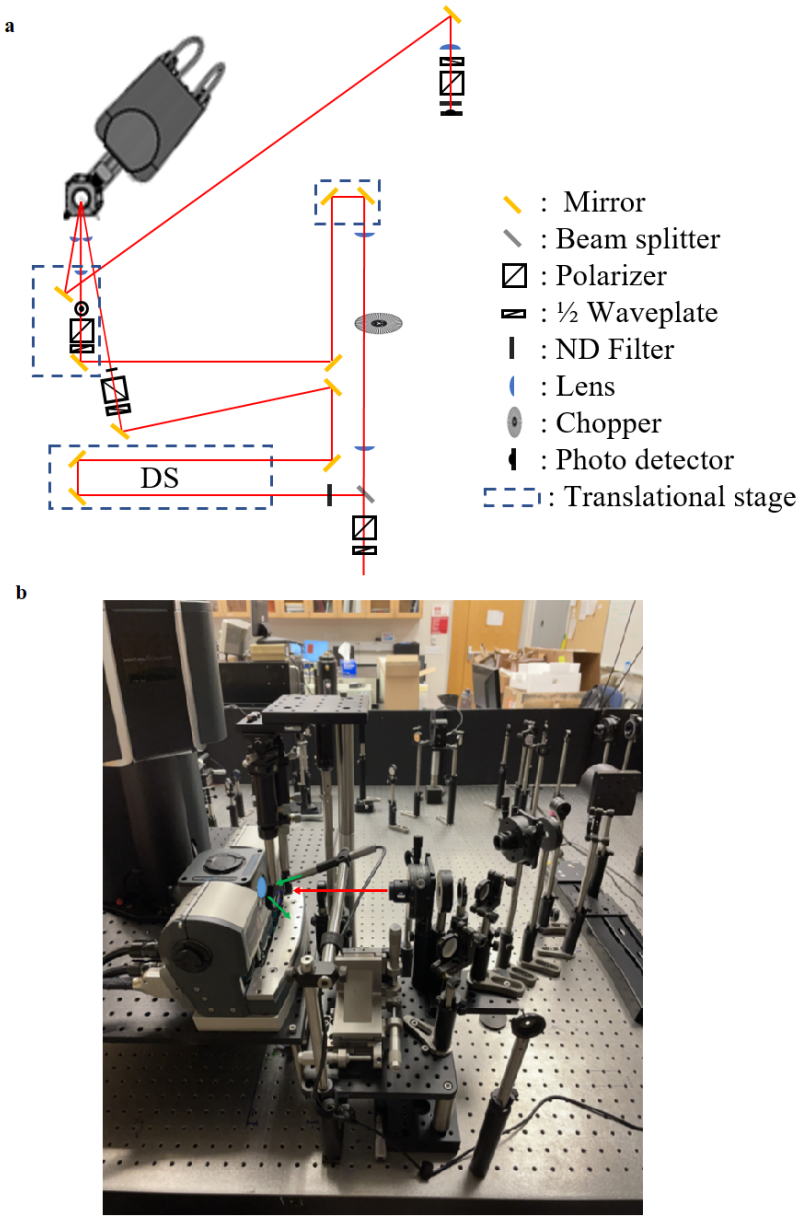

Figure 2.4: Ultrafast optical pump-probe setup: a) Schematic of the optical pump-probe schematic used in this thesis. An ultrafsat 800 nm laser pulse is polarized with a 1/2 waveplate and a polarization filter. The beam is then split 80:20 into a pump and probe segment. The pump beam is focused through a chopper at 970 kHz and moved along a fixed path length until being focused onto the sample at a 90° angle. The probe beam is passed through a variable delay stage and focused onto the sample at a 20° angle. Before hitting the sample, both beams are passed through a waveplate/polarization filter combination to ensure that the pump is p-polarized and the probe is s-polarized. The reflected probe beam is then directed towards another waveplate/polarization filter combination to filter out any p-polarized light from the probe and is focused onto a photodetector. b) A photo of the optical pump-probe setup. The area near the sample chamber is shown here. The red arrow shows the path of the pump beam and the green arrows show the incident and reflected probe beams (note that both pump and probe are 800 nm; the color shown is only to differentiate the two). The blue ellipse shows the location of the sample.

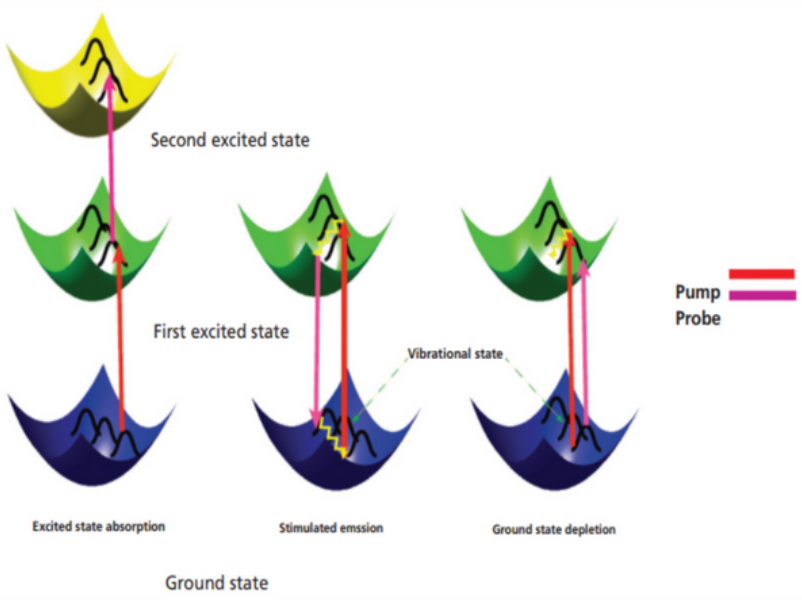

Figure 2.5: Optical pump-probe dynamics: The processes of excited state absorption, ground state depletion, and stimulated emission can occur during pump-probe experiments [52]. Excited state absorption causes an increase in reflectivity/absorption, whereas ground state depletion and stimulated emission cause a decrease in reflectivity/absorption.

as ground-state depletion, or bleach. If a transition from the excited state to the ground state with the same energy as the probe pulse is optically allowed, the probe pulse may cause stimulated emission from the excited to ground state. Because stimulated emission causes the emission of another photon coherent with the incident photon in the direction of propagation, this will also cause the absorption/reflection to decrease. Another possibility is that the carriers already in an excited state from the pump are further excited to a second excited state by the probe pulse. The increased excited state population by the pump pulse will then cause more excited carriers to be excited to the second state by the probe pulse, leading to an increase in absorption/reflection. These processes are illustrated in Figure 2.5. In metallic systems, the dynamics can be more complex, typically being treated as free carrier excitation. The two-temperature model has been used to describe the fs-timescale excitation of electrons and the slower electron-phonon thermalization describing the relaxation back to equilibrium. For LSCO with x = 0.3 composition, a ferromagnetic metallic state is observed at low temperature and a paramagnetic semiconducting state is observed at high temperature. Thus, depending upon the ground state (based on the sample temperature), differences in optical reflectivity can be potentially observed for LSCO thin films.

2.4 THz-pump with MOKE-probe for capturing magnetization dynamics in Fe thin films

To study the evolution of magnetism in Fe thin films pumped with THz pulses, 50 nm Fe thin films were grown by the Kukreja group using DC magnetron sputtering. A single-crystal Fe (200)-oriented thin film was deposited on an MgO (200)-oriented substrate and an amorphous Fe thin film was deposited on a SiO_2 substrate. Both crystalline and amorphous samples were capped with 5 nm of Au to prevent oxidation. Film deposition for the amorphous film was performed at room temperature, while the deposition for the crystalline film was performed at 500 °C. THz-pump excitation with MOKE as a probing method was used to capture the magnetization dynamics. These studies were performed at SLAC National Accelerator Laboratory in collaboration with Dr. Matthias Hoffman and Rahul Jangid and Meera in the Kukreja group. The THz pump was generated by optical rectification of a NIR pulse from a Ti:sapphire laser in a $LiNbO_3$ (LNO) crystal. Emitted THz pulses from the LNO crystal were polarized by a wire-grid polarizer to orient the electric and magnetic fields of the pulse. This pulse was incident on the Fe films at an angle of 45° in the xz-direction. Figure 2.6 shows the THz measurement schematic along with the coordinate system. The transient magnetization was probed using a portion of the same NIR beam used to generate the THz pump pulse. The probe optical pulse was temporally offset to either arrive at the sample at the same time as the maximum field strength of the THz pulse or delayed by a particular amount to map out the evolution as a function of time delay. The reflected probe pulse was then passed through a Wollaston prism to analyze the rotation of the probe beam. The resulting beam from the Wollaston prism was detected using a balanced diode to measure the polarization rotation of the pulse. In addition to the THz excitation, a static magnetic field was applied along the easy magnetization axis of the sample using electromagnets. Both the pump and probe pulses could be polarized such that the E-field (B-field) of the probe (pump) was parallel or perpendicular to the applied magnetic field in the sample plane.

As mentioned above, MOKE spectroscopy was performed to measure the evolution of magnetization following THz excitation. MOKE spectroscopy is generally performed in one of three main experimental geometries: polar, longitudinal, and transverse (Figure 2.7.) In the polar MOKE geometry, the sample is magnetized in an out-of-plane direction and the probing beam is incident at a near-normal angle. In the longitudinal geometry, the sample is magnetized in-plane along the direction of propagation of the probing beam, with the incidence angle being much further from normal than that used for polar MOKE. In the transverse geometry, the sample is magnetized in-plane perpendicular to the direction of propagation of the probe, also with a steep incidence angle. For both polar and longitudinal MOKE, the dielectric tensor of a magnetized material indicates that the reflected beam will experience a rotation of polarization relative to the

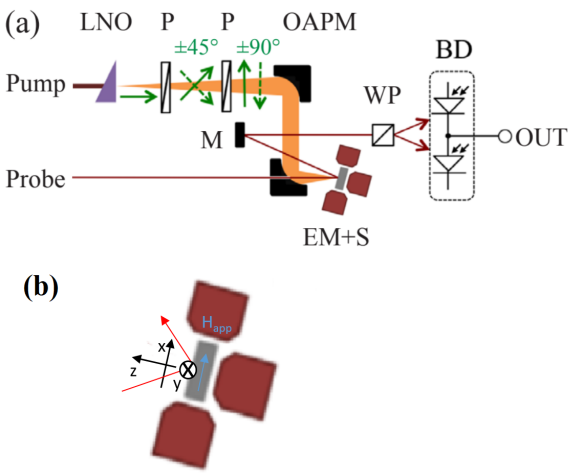

Figure 2.6: A schematic of the experimental setup used to measure magnetization dynamics of Fe thin films following THz excitation: a) An ultrafast optical laser is passed through an $LiNbO_3$ (LNO) crystal to generate a single-cycle pulse of THz frequency radiation by optical rectification. The resulting THz pulse is passed through wire grid polarizers (P) and directed onto the sample using off-axis parabolic mirrors (OAPM). The NIR probe pulse from the same initial pulse is directed onto the sample at the same angle (45°) to probe the magnetization dynamics using MOKE. MOKE signal is obtained from the reflected probe pulse by passing it through a Wollaston prism (WP) and onto a balanced diode detector (BD). The sample is held in a magnetic sample holder consisting of electromagnets, allowing an in-plane magnetic field to be applied. M represents a standard optical mirror, and EM + S represents the electromagnets and the sample [22]. b) The coordinate axes used in this experiment. X is taken as the direction of the applied, in-plane magnetic field, y is the orthogonal in-plane direction, and z is the out-of-plane direction. The THz pulse is incident at a 45° angle to the sample plane. The applied field is shown in blue.

component of magnetization in the corresponding direction for that geometry. In the transverse geometry, no rotation in polarization is observed, rather a change in reflectivity relative to the magnetization vector occurs. Typically, one of the three geometries are used in a MOKE measurement.

For our experimental setup, with a THz pump at a 45° angle to the sample plane in the xz direction, a portion of the in-plane magnetization can be driven out-of-plane by the strong magnetic field of the pulse. Thus, the assumption that the measured MOKE signal depends solely on the longitudinal MOKE response is insufficient and polar MOKE also needs to be included in the description. A study by You *et al.* [53] derived expressions for Kerr rotation of systems with magnetization components in both the polar and longitudinal directions for arbitrary probe incidence angle. These expressions were then compared to experimental results by Deeter *et al.* [54] and found to be in good agreement. These expressions are given by equations 2.1 and 2.2,

$$\theta_K^p \equiv \frac{r_{sp}}{r_{pp}} = \frac{cos\theta_0(m_z + m_y tan\theta_1)}{cos(\theta_0 + \theta_1)} \cdot \frac{in_0 n_1 Q}{(n_1^2 - n_0^2)} \tag{2.1}$$

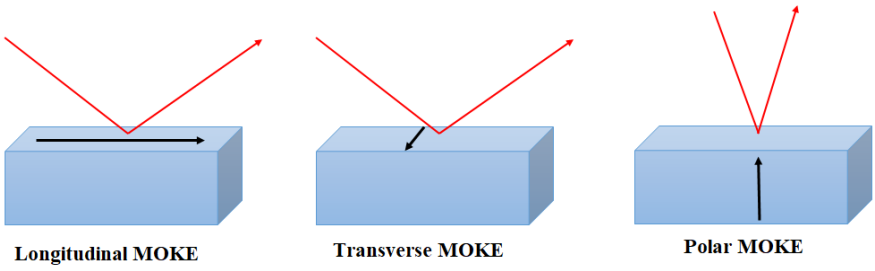

Figure 2.7: The three primary MOKE geometries: The black arrow indicates the direction of the magnetization and the red arrow is the optical path. Both polar and longitudinal geometries induce a polarization rotation on the reflected beam, whereas in the transverse geometry, a change in reflectivity is observed.

$$\theta_K^s \equiv \frac{r_{ps}}{r_{ss}} = \frac{cos\theta_0(m_z - m_y tan\theta_1)}{cos(\theta_0 - \theta_1)} \cdot \frac{in_0 n_1 Q}{(n_1^2 - n_0^2)} \tag{2.2}$$

It can be seen that Kerr rotation (θ_K^p or θ_K^s) depend solely on the magneto-optic constant (Q) of the material, the incident angle (θ_0) of the probe, the index of refraction of the material (n_1, and the polar and longitudinal magnetization components (m_z and m_x). θ_1 and n_0 are the refracted angle of the beam and the index of refraction of the first medium (in this case air). Here s and p refer to the incident polarization of the light.

2.5 Finite difference simulations of magnetization dynamics

This thesis uses Mumax to model ultrafast magnetization dynamics of Fe thin films pumped with an ultrashort THz pulse. Mumax is a micromagnetics package that uses the finite difference method to solve the LLG equation. It can also be used in a static manner to minimize the energy of a system with given starting parameters.

2.5.1 Energy minimization in Mumax

There are two different functions for energy minimization used in Mumax, minimize() and relax(). Minimize utilizes the steepest gradient method, whereby the energy of the system is lowered by evolving the system in the direction of the steepest decrease of energy until a local minimum is reached. This method is relatively quick, however, there is potential for the system to reach a local minimum in the energy landscape that is not the true energy minimum of the system. The relax() function is more robust, and relies on the total magnetic torque of the system, rather than the energy. With the relax() function, the system is allowed to evolve according to the LLG equation, but with precession disabled, such that only damping is considered. This allows for systems that are in far from equilibrium states to be minimized, and is the method used in

this thesis for simulating static hysteresis in Fe thin films.

2.5.2 Magnetization dynamics using Mumax

The finite difference method is a technique for modeling the evolution of a system with a governing differential equation. For micromagnetic simulations in Mumax, this equation is the LLG equation. A group of equidistant points are considered, and the location and values assigned to each of these points determines the state of the system at any given moment, $F(t)$. For micromagnetic simulations, each point contains a vector with a magnitude equal to the saturation magnetization of the material considered. The state of the system can be calculated by the relationship between the magnetization vectors and an effective field (H_{eff}). The effective field itself is a function of the exchange field, demagnetizing field, magnetocrystalline anisotropy, and Zeeman field. Both the LLG equation and the equation for effective field are given by equations 2.3 and 2.4.

$$\frac{d\mathbf{M}}{dt} = \frac{\gamma}{1+\alpha^2}(\underbrace{\mathbf{M}\times\mathbf{H_{eff}}}_{\text{precession}} + \underbrace{\alpha(\mathbf{M}\times(\mathbf{M}\times\mathbf{H_{eff}}))}_{\text{damping}}) \tag{2.3}$$

$$\mathbf{H_{eff}} = \mathbf{H_{exchange}} + \mathbf{H_{demag}} + \mathbf{H_{anisotropy}} + \mathbf{H_{Zeeman}} \tag{2.4}$$

Details on how Mumax calculates each of these terms is provided in VanSteenkiste *et al.* [55]. Given the current H_{eff} and the direction and location of each magnetization vector, the change for each discrete magnetization vector is calculated for a specific time step, τ using the LLG equation and the entire system is allowed to evolve simultaneously to a new state, $F(t+\tau)$. The effective field of the new state can then be calculated as before, and the system is allowed to evolve again. This method relies on the assumption that as the size of the time step approaches 0, this discrete solution will approach the actual solution to the differential equation. In the simplest case, a finite difference system can be allowed to evolve in this manner, known as the Euler solver. However, small errors may eventually accumulate and cause a substantial difference between the true and calculated solutions to the equation. To correct for these, a Heun solver may be used. In this case, the equation of motion is solved as before, however, after solving for the slope of the second state, $\frac{\Delta F(t+\tau)}{\tau}$, this slope is applied to the first state, $F(t)$. The evolved state is then considered to be halfway between the evolved state calculated by the two different slopes. This can be extended by using the RungeKutta (RK) solver. This solver is similar to the Heun solver, except instead of averaging only the slopes before and after the time step, additional slopes are calculated in between these points and added to the average. The Euler and Heun solvers are compared in Figure 2.8.

Both the LL [21, 34] and LLG [22, 23] equations have been used to model the ultrafast magnetization response of ferromagnetic thin films to intense THz pulses. However, as the observed magnetization response

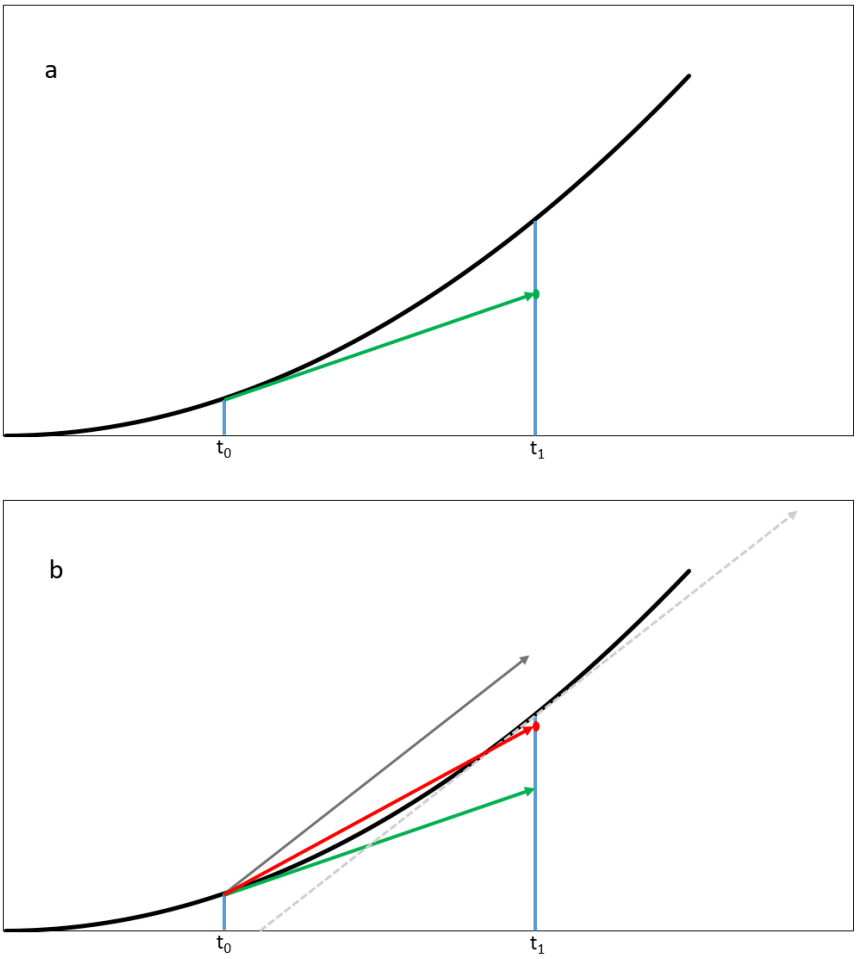

Figure 2.8: Comparison of Euler and Heun solver: The exact solution to a governing differential equation is given by the black line. a) The Euler solver takes the slope of the governing function at a given time and propagates this slope for the duration of the time step. This endpoint of this line becomes the value for the function at the new time (green.) b) The Heun solver avoids the propagation of error that can occur with the Euler solver by taking the slope at the new point (dashed gray), and reapplying that slope to the original point (solid gray.) The new value for the function is taken from the slope that bisects these two slopes (red.)

of ferromagnetic thin films to THz pulses is extremely fast, an overdamped LL equation has been proposed to model THz-driven phenomenon. In this scenario, a stronger damping parameter causes the magnetic moment of the material to more quickly relax to the direction of the effective field. Thus far, this has been applied by Ruchert *et al.* [34] to geometries where the B-field of the THz is perpendicular to the static field applied to the sample. As the THz field considered in this thesis is at a 45° angle to the sample magnetization, an overdamped LL equation will be utilized in this thesis, similar to Ruchert *et al.* [34]. Overdamping in the LL equation is achieved by increasing the Gilbert damping parameter, α. However, Mumax natively uses the LLG equation, in which the total magnetic torque is normalized by a factor of $\frac{\gamma}{1+\alpha^2}$. This means that as α is increased, the total torque (and thus precession) on the system by a certain applied field is reduced by a factor of α^2. This can be circumvented by utilizing the LL equation, where modifying the damping parameter only modifies the second damping term and not the first precession term. Note that you can also consider a damping-dependent parameter $\gamma' = \gamma(1+\alpha^2)$, and utilize the LLG equation. This equation of motion is exactly equivalent to the LL equation, however, in this thesis, the parameters used for the overdamped simulations describe α and γ as given in the LL equation and for normally damped simulations, α and γ as given in the LLG equation. Note that for normal damping, while the results presented are for the LLG equation, for the normal damping parameter (0.0018) of a metal such as Fe, both the LLG and LL equation lead to the same results.

2.6 Conclusion

Pump-probe techniques are powerful tools for measuring dynamics in materials at fs-ps timescales. In this thesis, optical pump-probe transient reflectivity will be considered to investigate the ultrafast dynamics of the ferromagnetic to paramagnetic phase transition in LSCO. Additionally, micromagnetic simulations will be performed to model experimentally observed magnetization behavior of Fe thin films during ultrafast THz pumping. Chapters 3 and 4 will show the results obtained using these experimental methods and a discussion of the magnetization dynamics observed in these materials at ultrafast timescales.

Chapter 3

THz-driven magnetization dynamics for Fe thin-films

This chapter presents the ultrafast magnetization dynamics of Fe thin films using THz pump and MOKE probe as well as the modeled behavior using Mumax simulations. The central question is how the crystallinity of the film (single-crystal vs amorphous) influences the THz-driven dynamics. Additionally, simulations are used to determine the role of magnetization precession in the observed dynamics, and whether an over-damped LL equation can accurately model these dynamics as observed in Co films [34]. The chapter begins by discussing appropriate parameters for the systems being modeled including how to differentiate between amorphous and crystalline materials in micromagnetic simulations. This was done by comparing experimentally measured static hysteresis loops with simulated hysteresis loops. I then explore the THz-driven magnetization dynamics as a function of time and compare the results to those obtained experimentally. Finally, the THz-driven behavior under a static applied field is considered and compared with the experimental measurements.

3.1 Determining the material parameters of Fe thin films

Two films are considered in this chapter: the single-crystal film is 50 nm thick (200)-oriented Fe grown on a (200)-oriented MgO substrate and the amorphous film is 50 nm Fe grown on 100 nm SiO_2 deposited on a Si substrate. The XRD of each of these films is shown in Figure 3.1. In order to understand the dynamics that occur on an ultrafast timescale in Fe thin films excited by a THz pulse, a dependable model must first be developed to describe the static properties of these films. In the framework of micromagnetism,

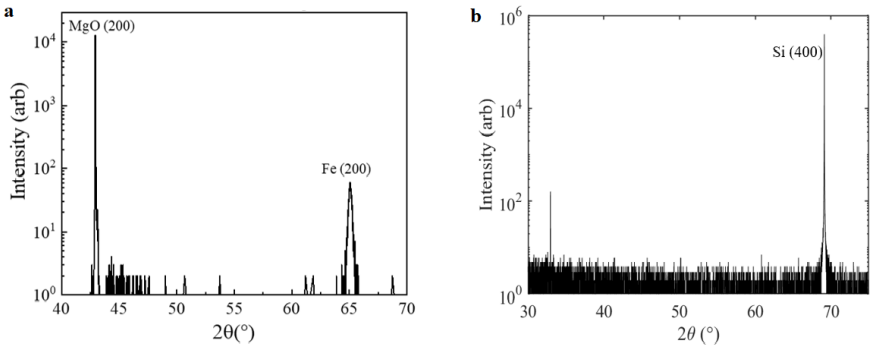

Figure 3.1: XRD of Fe thin films: a) XRD of single-crystal Fe (200) on MgO (200). The separation between the substrate and film peaks is due to the fact that the [100] direction of the Fe is grown along the [110] direction of the MgO, separating the length of the [200] directions by a factor of $\sqrt{2}$. b) XRD of amorphous Fe on SiO_2. No Fe peaks can be observed, indicating the amorphous nature of the film. The strong peak at 69° is the (400) peak of the Si substrate.

this means determining the parameters that will be used to determine the magnetization vector and the effective field. These materials parameters are the saturation magnetization (M_{sat}), the magnetocrystalline anisotropy magnitude (K) and direction (u), and the exchange stiffness A_{ex}. M_{sat} is equal to the greatest magnetic moment that the material can achieve in a strong applied field. The uniaxial magnetocrystalline anisotropy direction (u) describes the easy axis of the film, i.e., the direction of magnetization which is most energetically favorable in a crystalline material. The magnitude (K) describes the size of the energy benefit from having a magnetic moment aligned along the u direction. A_{ex} is a parameter of ferromagnetics that is related to the atomic exchange integral J_{ex} but which is averaged across a crystal lattice. This parameter describes the energy benefit for magnetic moments in a ferromagnet to be aligned parallel to each other. The experimental determination of these micromagnetic parameters for a specific system is not trivial and is not considered in this thesis. Instead, I begin with the bulk, 0K parameters for Fe from literature [56], and adjust them to fit the experimentally observed magnetic properties of these films. The saturation magnetization is not expected to change between bulk Fe and Fe thin films, with a value of 1.71×10^6 Amps/meter. However, the strength, and sometimes even the direction of the magnetic anisotropy can vary with film thickness, crystallinity, temperature, and substrate due to the effects of shape and stress anisotropy, [57] as can the exchange stiffness [58]. Table 3.1 gives the value of each material parameter used in this thesis for both Fe thin films. The Gilbert damping parameter α does not affect the static properties of the material and will be discussed in section 3.3.

Table 3.1: Material parameters for micromagnetic simulations of Fe thin films

	$\mathbf{M_{sat}}$ (A/m)	$\mathbf{A_{ex}}$ (pJ/m)	$\mathbf{K}$ (kJ/m^3)	$\mathbf{u}$	$\boldsymbol{\alpha}$	$\boldsymbol{\alpha_{overdamped}}$
Epitaxial	1.71×10^6	2.5	1	(1,0,0)	0.0018	30
Amorphous	1.71×10^6	3	-1	(0,0,1)	0.0018	30

3.1.1 Material parameters for single-crystal Fe film

To determine the appropriate micromagnetic parameters for the single-crystal Fe film in this study, simulated hysteresis loops were compared to those of single crystal 50 nm Fe(200) films grown with DC magnetron sputtering on MgO. These films exhibit a coercive field (H_C) of approximately 25 Oe as measured by VSM and static MOKE spectroscopy. Mumax does not simulate atoms and cannot directly model the crystallinity of the film; however, the crystallinity can be accounted for by setting the magnetocrystalline anisotropy direction to the easy axis direction. In the experiments considered here, the easy axis of the film lies along the x-direction (see Figure 2.6b), hence u is set to (1,0,0). When using the bulk, 0K value for K (48 kJ/m^3) the coercive field of the film was found to be 400 Oe (gray curve in Figure 3.2), which is much larger than the experimentally observed 25 Oe (orange curve). This is partially due to a modification of the materials parameters by temperature and thin film geometry [57], as well as the interplay between magnetocrystalline anisotropy and exchange stiffness.

The exchange stiffness of bulk Fe at 0 K is given as 21 pJ/m. However, akin to magnetocrystalline anisotropy, this value results in a much higher coercivity of Fe films than experimentally observed. There could be multiple reasons for a higher simulated coercivity. One factor could be temperature. It is known that increased temperature can reduce the exchange stiffness of ferromagnetic materials [58], with some sources giving a value as low as 8 pJ/m for Fe at room temperature [59]. Another factor could be the exchange stiffness may be different for the thin films vs the bulk sample. A third factor could be the periodic boundary conditions used in the simulations. In order to account for the extremely large dimensions in x and y (5 mm) relative to z (50 nm) within the limits of computational power, periodic boundary conditions are used. These periodic boundary conditions cause a small simulated region (cell) to repeat in both the x and y directions, simulating a larger thin film [55]. However, these repetitions of the same cell can impose arbitrary boundaries on the size of magnetic domains within the system. These boundaries can also affect the way that K and A_{ex} are modeled. The significance of these boundaries to the values of K and A_{ex} can be understood in terms of domain wall theory. Magnetic domain walls are regions between two oppositely oriented domains (i.e., up and down domains), where the direction of magnetization changes. The width of these domain walls is determined by competition between the exchange energy, which favors wide domain walls, and the anisotropy energy, which favors narrow domain walls. In a large single-crystal, such as the

epitaxial film considered in this thesis, a very low coercivity is achieved because there are no defects or grain boundaries that prohibit or pin domain wall motion, allowing domain areas to be extremely large, potentially encompassing the entire film at saturation. Domain wall motion is considered the most efficient way to switch magnetization direction as an external field is applied. However, when modeling a single-crystal with periodic boundary conditions, if a domain forms within one cell, it must form in each of the 121 (11×11) cells created by the periodic boundary conditions in this thesis. The nucleation of this many small domains can require a significant penalty to the total exchange energy of the system. Additionally, the lack of true edges imposed by periodic boundary conditions makes nucleation of domains more difficult, as the strong demagnetizing field on the edges of a real sample facilitates formation of domains to minimize the demagnetizing field and lower the total energy. Thus, these three effects (temperature, bulk vs thin film, and periodic boundary conditions) may cause an increases in the coercivity of the simulated films. Lowering both K and A_{ex} can help compensate for this by reducing the energy penalty for the increased domain wall perimeter/area ratio. Specifically, lowering K reduces the energy penalty for magnetic moments outside of the magnetocrystalline easy axis, and reducing A_{ex} reduces the penalty for moments that are dissimilar to nearby moments.

Considering the effects of temperature, film thickness, and periodic boundary conditions, both K and A_{ex} were decreased to more closely model the experimentally measured static coercivity of the single-crystal Fe film. It should be noted that both K and A need to be reduced as they are two competing factors in nucleation and formation of domain walls. A value of $1\,kJ/m^3$ is chosen for K, and 2.5 pJ/m for A_{ex}. Under these conditions, the coercivity for the crystalline Fe film was found to be about 50 Oe. Further lowering the exchange stiffness can cause the magnetization to flip in two steps, perhaps due to a lack of sufficient exchange stiffness which keeps the moments aligned, whereas only lowering the magnetocrystalline anisotropy is not sufficient to significantly reduce the coercivity. Thus, in order to match the experimental results and maintain single-step switching, these micromagnetic parameters were used, despite the slightly higher coercivity (50 Oe) than that observed experimentally (25 Oe) as shown in Figure 3.2.

3.1.2 Material parameters for amorphous Fe film

For amorphous Fe films, the lack of crystallinity means that there is no easy magnetic axis. In micromagnetic simulations, this can be treated by using the magnetocrystalline anisotropy to define a hard axis. For an amorphous film, the hard axis is not truly due to magnetocrystalline anisotropy, but rather due to the shape anisotropy of a thin film material. Shape anisotropy is already accounted for in Muamx by the demagnetizing field term, however, with the lowered exchange stiffness, completely eliminating the magnetocrystalline

anisotropy can cause a complete lack of magnetic remanence in the system. Thus, a small, out-of-plane hard axis can be included in addition to the shape anisotropy to maintain the ferromagnetic behavior of the film while note defining a preferred in-plane magnetization direction. This is done by setting K to a negative number with u = (0,0,1). The strength of the anisotropy is set to $-1\,\mathrm{kJ/m^3}$; this value was chosen as it was large enough to induce magnetic remanence in the film, but not so large as to possibly cause pseudo-crystalline behavior. A similar approach was used by Vicario *et al.* [21].

Similar temperature and film thickness effects on the exchange stiffness of single-crystal Fe films will also apply to amorphous films. It should be further noted that amorphous Fe nanoparticles have been measured to have exchange stiffnesses up to 30% lower than that observed for crystalline Fe [60]. With these considerations, the exchange stiffness for the amorphous Fe film is set to $3\,\mathrm{pJ/m}$.

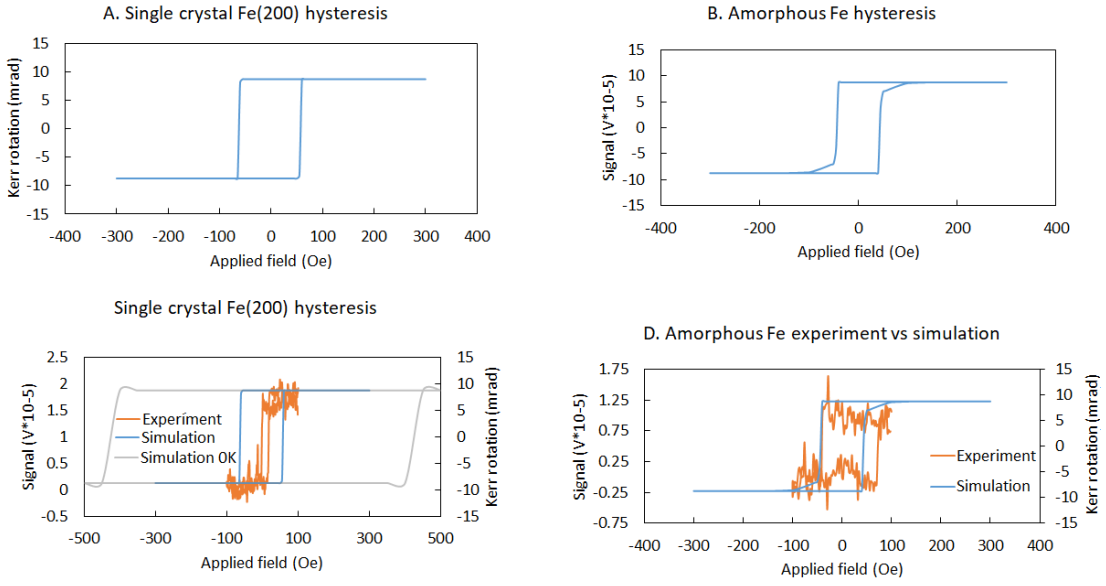

Figure 3.2: Hysteresis loops of single-crystal epitaxial and amorphous Fe films: Simulated hysteresis loops for (a) crystalline film and (b) amorphous film using the final materials parameters. c) A comparison of the single crystal Fe hysteresis for simulation with final parameters and bulk 0 K parameters, as well as the experimentally measured hysteresis. d) A comparison of experimental (MOKE) and simulated hysteresis loops of amorphous Fe.

3.1.3 Static hysteresis loops of Fe thin films

The experimental hysteresis loops of both single-crystal and amorphous Fe thin films collected via MOKE and the simulated hysteresis loops are shown in Figure 3.2. These material parameters were also used to simulate and compare dynamic behavior. In order to directly compare experiment and simulations, a conversion must be made between magnetization given by Mumax, and Kerr rotation which is measured

experimentally. As discussed in the previous Chapter, the strong B-field of the THz pulse can pull a component of the magnetization out of the sample plane. Hence, the Kerr rotation cannot be assumed to be related only to the longitudinal component of the magnetization of the sample. As the incident polarization of the laser used to measure Kerr rotation is p-polarized, equation 2.1 is used to obtain Kerr rotation from the magnetization data obtained by Mumax. In addition to the incident angle, polarization, and refractive index information necessary to obtain Kerr rotation, the magneto-optic parameter (Q_0) for Fe at 800 nm is necessary to estimate the exact angle of Kerr rotation. However, to date, no studies have calculated the value of Q_0 for Fe at this wavelength. The value used in this thesis was extrapolated from a study by Robinson [61] which measured the value of Q_0 for Fe at wavelengths between 360 - 616 nm. The wavelengths were converted to energies and the value of Q_0 as a function of energy was fit to a quadratic curve, from which a value of 0.065 was obtained for 800 nm (Figure 3.3)

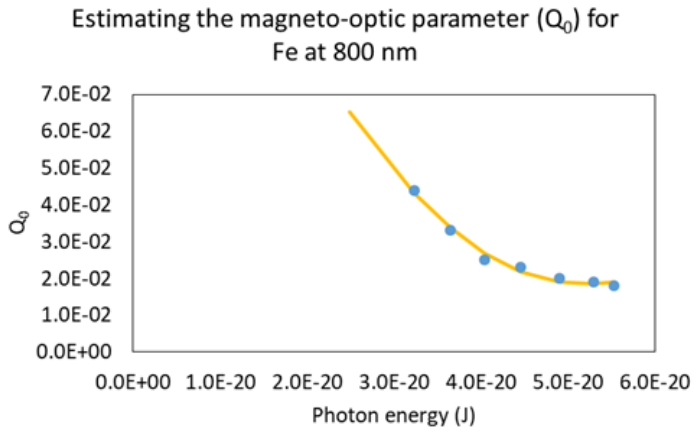

Figure 3.3: Determining the magneto-optic parameter (Q_0 for Fe: In order to estimate the magneto-optic parameter for Fe at 800 nm, values of Q_0 for Fe between 360-616 nm were taken from Robinson [61] These were plotted as a function of photon energy and fit to a quadratic curve ($Q_0 = 6.36 \times 10^{37} E^2 - 6.61 \times 10^{18} E + 0.19$, ($R^2 = 0.983$), where E is the photon energy in Joules. This curve was used to estimate the value of Q_0 at 800 nm (0.065).

Another complexity arises from the fact that the experiments do not directly track the Kerr rotation. The hysteresis loops for the THz pump-probe study measure the voltage which is proportional to the Kerr rotation. This is because the Wollaston prism/balanced diode used to measure change in polarization of the optical probe yields voltage data which is proportional to the Kerr rotation. To convert simulated Kerr rotation into voltage on a hysteresis loop, the maximum and minimum simulated Kerr rotations were taken to be the maximum and minimum voltages given by the experimentally measured static hysteresis loops, and all intermediate values were linearly extrapolated from these. While this works with hysteresis loops where

saturation is reached, for the time delay curves presented later (such as in Figure 3.5), no conversion can be made from Kerr rotation to voltage, due to lack of information regarding the detector gain. Therefore, the simulated data presented here will retain units of Kerr rotation. While this does not allow us to compare the relative magnitude of the response between simulation and experiment, it still allows us to compare the dynamics and timescales associated with THz-driven magnetization dynamics.

3.2 Mumax simulations of THz-driven dynamics

In order to test the effectiveness of the Mumax simulations developed in this thesis, we first applied the modeling to 10 nm amorphous Co thin films to compare our results with previous studies by Vicario *et al.* The parameters of the film and experimental geometry were chosen to correspond with those used in literature by Vicario *et al.* [21]. The magnetic parameters used for the film were: A_{ex} = 31 pJ/m, M_{sat} = 1.4×10^6 Amps/meter, K = $-1.6\,MJ/m^3$, and u = (0,0,1), with the Gilbert damping parameter α set to 0.005. The magnetization dynamics of this film were modeled with a THz pulse applied as a Zeeman field, with a peak field of 0.4 T. The THz pulse was modeled as a Gaussian multiplied by a sine wave, with two additional Gaussian functions as shown in Figure 3.4. A static Zeeman field of 0.01 T was also applied in the sample plane. This was done to achieve the same excitation conditions as Vicario *et al.* measurements. It should be noted that the coordinate system used for this Co film was chosen to be identical to that used by Vicario *et al.* and is distinct from that described for Fe films in Chapter 2. For the Co thin film, the x axis is chosen to be the in-plane direction of the applied static field, the y axis is out of the sample plane, and the z axis is in-plane and orthogonal to the applied static field. The THz field was applied with an incidence angle of 10° from the sample normal, with the B-field being oriented along the x-direction. Essentially, this is the coordinate axis described in Figure 2.6, but with the y and z axes swapped.

The dynamics of the Co film pumped by this THz pulse were modeled with both normal damping and no damping ($\alpha = 0$) as was done by Vicario *et al.* [21]. A comparison of the results using Mumax and those reported by Vicario *et al.* is shown in Figure 3.4. The magnetization dynamics observed using Mumax show a Zeeman-driven effect during the THz pulse, with the sample magnetization direction being mainly determined by the direction of the THz magnetic field. Strong, precession-dominated dynamics are also observed immediately after the THz pulse is switched off, in the z-direction (in the sample plane and perpendicular to the static applied field). The comparison of simulations by Vicario et al, and our Mumax simulations show similar behavior for all three directions. In addition, both the Mumax simulation performed here and the simulation done by Vicario *et al.* showed no difference between the normally-damped and undamped magnetization dynamics, indicating that damping effects seem to have little effect on the

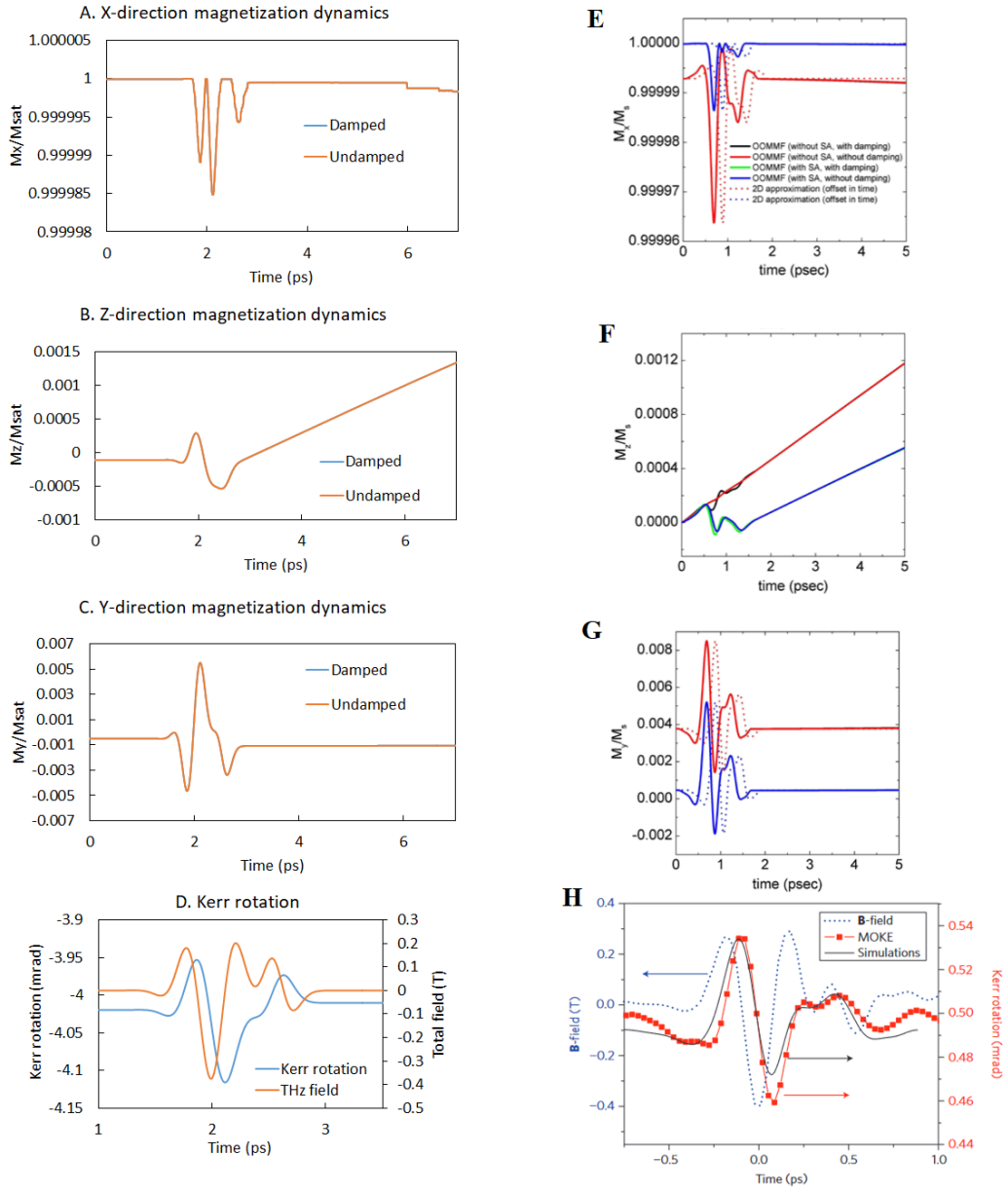

Figure 3.4: THz-pulse driven magnetization dynamics of Co film: A-D shows the results of the Mumax simulation. E-F gives the results of Vicario *et al.* [21]. As shape anisotropy was always considered in the Mumax simulations, the results should be compared with the blue and green curves of Vicario *et al.* The results show good agreement between our simulations and experimental as well as simulation study done by Vicario *et al.*

dynamics when the THz B-field is closely aligned with the initial magnetization of the sample. The simulated MOKE response from the Mumax simulation was calculated as described in Chapter 2, and using a value of 0.03 for Q_0 of Co, extrapolated from research by Ballantynet [62] as magneto-optic parameter was not provided by Vicario *et al.* The simulated MOKE response of the Co film in Mumax showed a coherent response to the THz pulse, offset by about 120 fs, similar to what Vicario *et al.* observed experimentally as well as from their simulation. There is a small difference in the magnitude of the Kerr rotation between Vicario *et al.* and the Mumax simulation which is likely due to differences in the magneto-optic parameter used for this study vs Vicario *et al.*

3.3 Simulating THz-driven response of Fe thin films

Having established Mumax as a reliable tool for modeling ultrafast THz-pulse induced magnetization dynamics, we can now use it to model the dynamics observed experimentally for Fe thin films. Both single-crystal epitaxial and amorphous Fe films have been experimentally shown to exhibit strongly coherent magnetization dynamics when pumped with similar THz pulses. However, while Vicario *et al.* [21] used a THz pulse with the B-field nearly parallel to the sample magnetization (offset by 10 °), in these experiments performed on Fe films, the angle between the THz B-field and the sample magnetization ranged from 45° to 90°. This necessitates consideration of the overdamped LL equation as described by Ruchert *et al.* [34]. As discussed in Chapter 2, we convert the LLG equation to the LL equation when overdamping the system.

Some studies have also observed demagnetization of amorphous magnetic films after pumping with intense single-cycle THz pulses [22, 23]. The LLG equation requires the magnitude of the magnetization vector to be constant, thereby making the modeling of transient demagnetization impossible. This has been addressed in other studies by adapting the magnetic magnitude used in the LLG equation to the measured magnitude (via MOKE) at a given time [23]. However, as demagnetization is not observed for any samples in these experiments, such a treatment is not considered here.

The parameters used to model each Fe film were already discussed in the first section of this chapter. As with the Co simulation, both the static applied field and the THz field were modeled as Zeeman fields. The strength of the static field applied is 0.01 T same as experiments. The direction of this field is the x-direction except for the transverse geometry experiments which will be discussed later in this chapter. For the THz pulse a peak E-field of 15 MV/m was used as measured by Reference [22] for this setup, which equates to a B-field of 0.05 T. This field was modeled in Mumax as a Gaussian with a full-width at half maximum of 1.7 ps multiplied by a sine wave with a frequency of 0.4 THz as described below:

$$H(t) = 0.05\ exp\left(\frac{(t-3)^2}{10^{12}}\right) \times sin[2\pi \times 0.4(t + 3.5 \times 10^{-13})] \tag{3.1}$$

This THz field was then applied to the Fe films at a 45° angle between the x and z axes to match the experimental excitation (Figure 2.6).

3.3.1 Overdamped vs normally damped magnetization dynamics in Fe thin films

The magnetization dynamics for single-crystal epitaxial and amorphous Fe films pumped with the THz pulse previously described were first modeled in Mumax using the normal Gilbert damping parameter for Fe ($\alpha = 0.0018$). The simulated Kerr rotation was calculated from the Mumax magnetization data and plotted as a function of time to compare with the experimentally observed dynamics. As shown in Fig. 3.5, the experimentally observed magnetization dynamics show that the magnetization evolution is coherent with the THz pulse, offset by a $\approx$ 80 fs delay for both the single-crystal and amorphous Fe films. However, the simulated dynamics of both films does not match the experimentally measured dynamics for the duration THz pulse is applied. Additionally, a strong precession is observed immediately after the THz pulse is turned off for the Mumax simulation, which is not observed experimentally. Thus, for experimental geometries where the THz B-field is not closely aligned with the sample magnetization, the normally-damped LLG equation fails to adequately describe the dynamics. As a next step we used the overdamped LL equation to simulate the behavior. The damping parameter was found to be correlated to the delay between the peak of the THz pulse and the peak of the simulated Kerr rotation, with a larger α corresponding to a smaller delay. In order to match the experimentally observed 80 fs delay between the THz field peak and the sample magnetization peak from the time-resolved MOKE, a value of 30 was chosen. The dynamics of both the single-crystal and amorphous Fe thin films with overdamping applied were found to agree with the experiments, with a high level of coherence between the magnetization and the applied THz , offset by an 80 fs delay. The amplitude of the response was also similar for crystalline and amorphous thin films ($\Delta\theta_K \approx 0.8$ mrad), indicating that crystallinity alone does not influence THz-driven response. The experimental, normally-damped, and overdamped Kerr rotations are plotted as a function of time in Figure 3.5.

In order to map out the evolution of magnetization following THz excitation, the path of the net magnetization of the sample over 100 ps is plotted in 3D for both the overdamped and normally damped cases for the epitaxial film and amorphous film in Figure 3.6. As the magnitude and direction of the THz field vector changes, the magnetization vector responds by moving directly towards the field, without precession. This is not unexpected, as precession frequencies of the LLG equation are typically on the order of GHz. This is

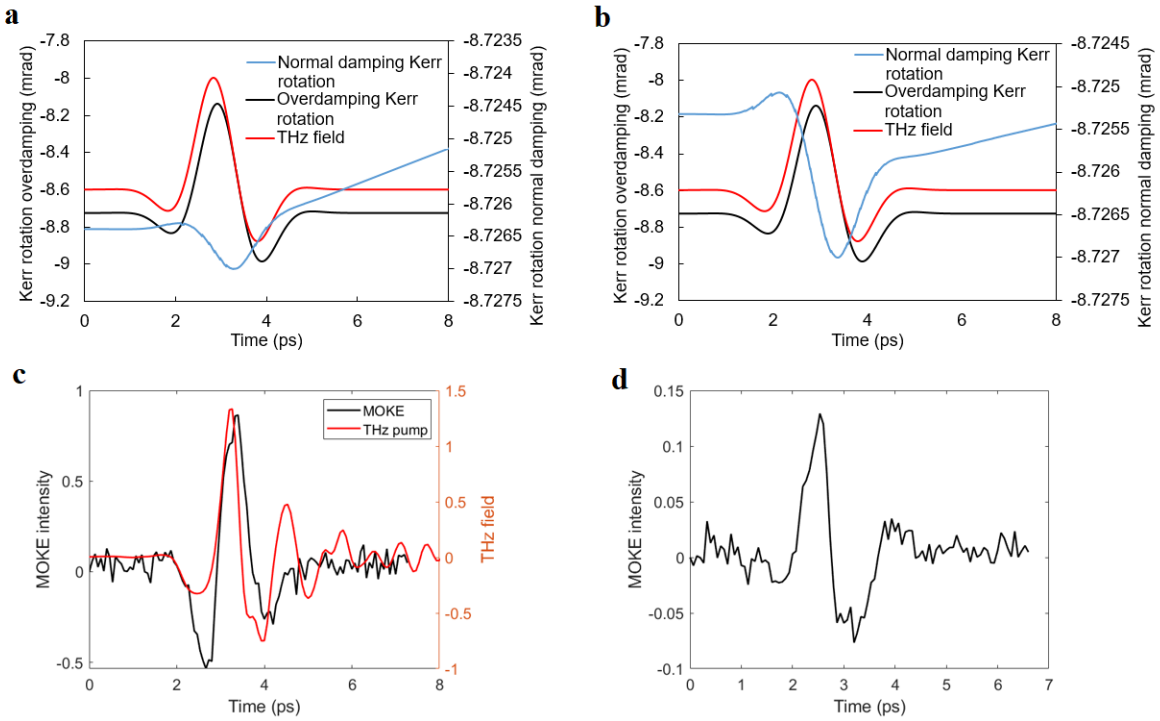

Figure 3.5: Simulated and experimentally measured magnetization dynamics of Fe films. Simulated dynamics for normally damped and overdamped LL equation for (a) crystalline Fe, and (b) amorphous Fe. The experimental dynamics obtained using ultrafast MOKE are shown for epitaxial Fe in (c) and amorphous Fe in (d). The red curve is the THz pulse used for excitation, and the black curve is the MOKE response. For the amorphous sample, the experimental THz pulse is not shown as no delay curve for the THz pulse was collected at a similar time as the MOKE curve for this sample. As day to day drift can be substantial, this was omitted.

simlar to what was observed by Vicario *et al.* [21] on thin Co films, where the dynamics during the THz pulse were entirely dominated by the Zeeman effect of the applied THz field. For the normally-damped dynamics, a precession of the magnetization follows the Zeeman-dominated dynamics during the THz pulse, which has not been measured experimentally. These results show that the observed THz-induced magnetization dynamics in the films can be modeled by an overdamped LL equation, with the strong damping component dominating the dynamics compared to the precession. Given the inability of the normally-damped LLG equation to describe the dynamics observed in these experiments, the overdamped LL equation will be considered for the remainder of this chapter.

An interesting result of these simulations is that the sample magnetization along the direction of the applied static field (x) does not necessarily follow the THz pulse coherently, even considering the aforementioned delay (Figure 3.6). As the magnetization is initially saturated in x and the LLG equation does not allow the magnitude of the magnetization vector to change, the absolute change in x-magnetization, while

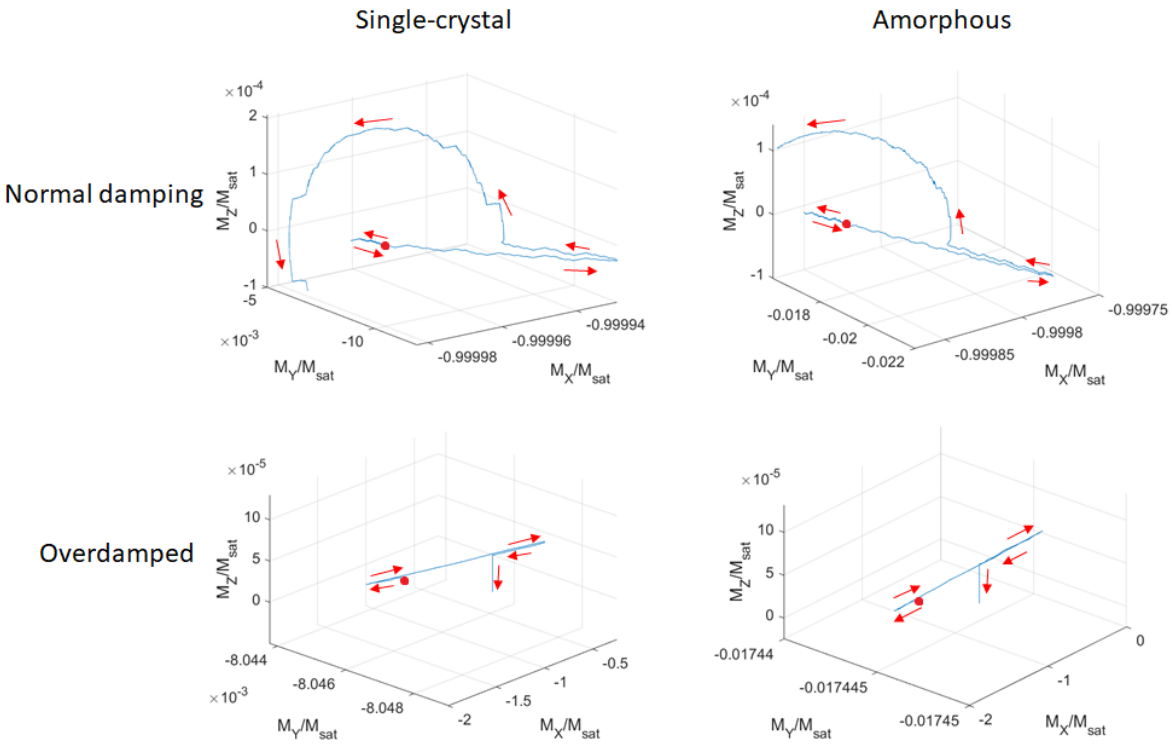

Figure 3.6: Magnetization evolution of Fe films using THz pump: The evolution of the average magnetization vector of the sample after pumping with a THz pulse and continuing for 100 ps. Both overdamped and normally damped cases are considered for single-crystal and amorphous Fe. A strong precession component can clearly be seen in the normally damped systems after the Zeeman dominated response during the THz pulse. The red arrows are given as guides for temporal evolution, with the red dot indicating the position at t_0.

incoherent, is relatively small. When magnetization along the xz direction (THz field orientation, 45° from the sample plane) is considered, the response is once again relatively coherent, albeit with the same delay.

Critically to these experiments, while both the amorphous and crystalline Fe thin films show a coherent magnetization response to the THz pump, no demagnetization is observed in either film. This indicates that at these THz pump fields, the lattice alone is not responsible for the demagnetization that has been observed in amorphous FeCoB alloy [22, 23] or in Co/Pt multilayers [24]. Rather, this demagnetization is possibly due to the influence of alloying or other multi-element interactions. For single-element films, the lack of demagnetization means the overdamped LL equation is sufficient to describe the magnetization dynamics, and the crystallinity does not have a significant effect ont he observed dynamics.

3.3.2 Influence of experimental and material parameters on magnetization dynamics

The applicability of the overdamped LL equation to the Fe systems studied here allow us to explore the influence of experimental and material parameters on the magnetization dynamics. As a first step, we studied the role of magnetic field direction both static and THz. Experimentally, when the direction of the applied static field or THz field is reversed, the observed magnetization dynamics are equal in magnitude, but opposite in direction for both crystalline and amorphous Fe. However, in simulations, the direction of the dynamics depends only on the direction of the THz field, and not the static field, with the static field only determining if the initial Kerr rotation before the THz pulse is positive or negative (Figure 3.7). This apparent discrepancy is explained by the calibration of the detector. The balanced diode setup used in the experimental studies records a voltage that is proportional to the Kerr rotation of the probe beam. For opposite saturation directions in a material, the Kerr rotation should be of equal magnitude but in opposite directions. However, for both positive and negative static fields, the experimentally measured voltage at the initial magnetization was negative. The results shown here were vertically transposed such that the initial voltage recorded was at 0 V. Thus, the positive and negative directions in the experimental data are actually flipped relative to each other, and the simulation and experiment are consistent.

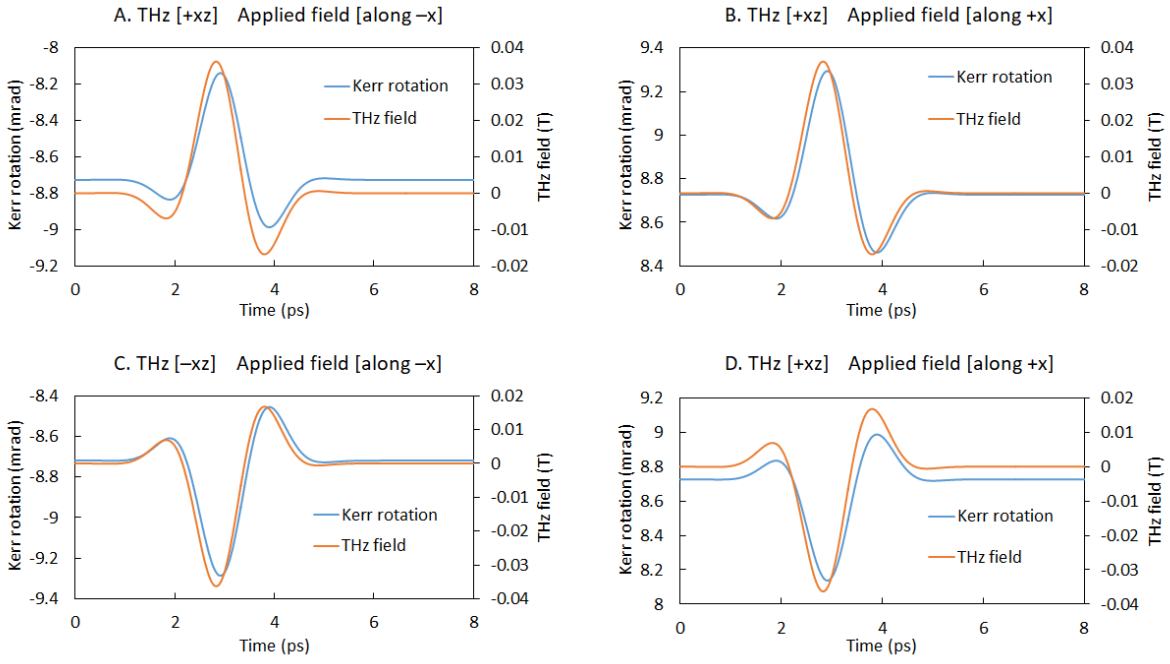

Figure 3.7: Ultrafast magnetization dynamics of single-crystal Fe film with varying direction of THz and static field: The direction of the simulated dynamics is determined by the direction of the THz field, whereas the initial Kerr rotation is determined by the static field direction. In each case, the observed dynamics are of equal magnitude and coherent with the THz field.

The dynamics driven by the THz pulse were also found to be independent of the exchange stiffness and magnetocrystalline anisotropy strength of the material. Within a relatively broad range of A_{ex} (from 2 pJ/m to 21 pJ/m,) the magnitude and coherency of the induced dynamics are unaffected, indicating that the dynamics driven have little dependence on the magnetic hardness of the material. Varying the anisotropy strength from $0.5\,kJ/m^3$ to $4.8\,kJ/m^3$ also did not effect the dynamics. In contrast, the strength of the THz field was found to be directly proportional to the ultrafast magnetization response of the system. By varying the magnitude of the THz B-field applied to the single-crystal Fe thin film, a linear relationship was found between the B-field strength and the value of $\theta^K_{max} - \theta^K_{min}$, where θ^K is the Kerr rotation. This result indicates the tunability of the magnetization control that can be achieved using single-cycle THz field strength, regardless of the magnetic parameters of the film. Figure 3.8 shows the dynamics of a single-crystal Fe film with varying exchange stiffness and THz field strength.

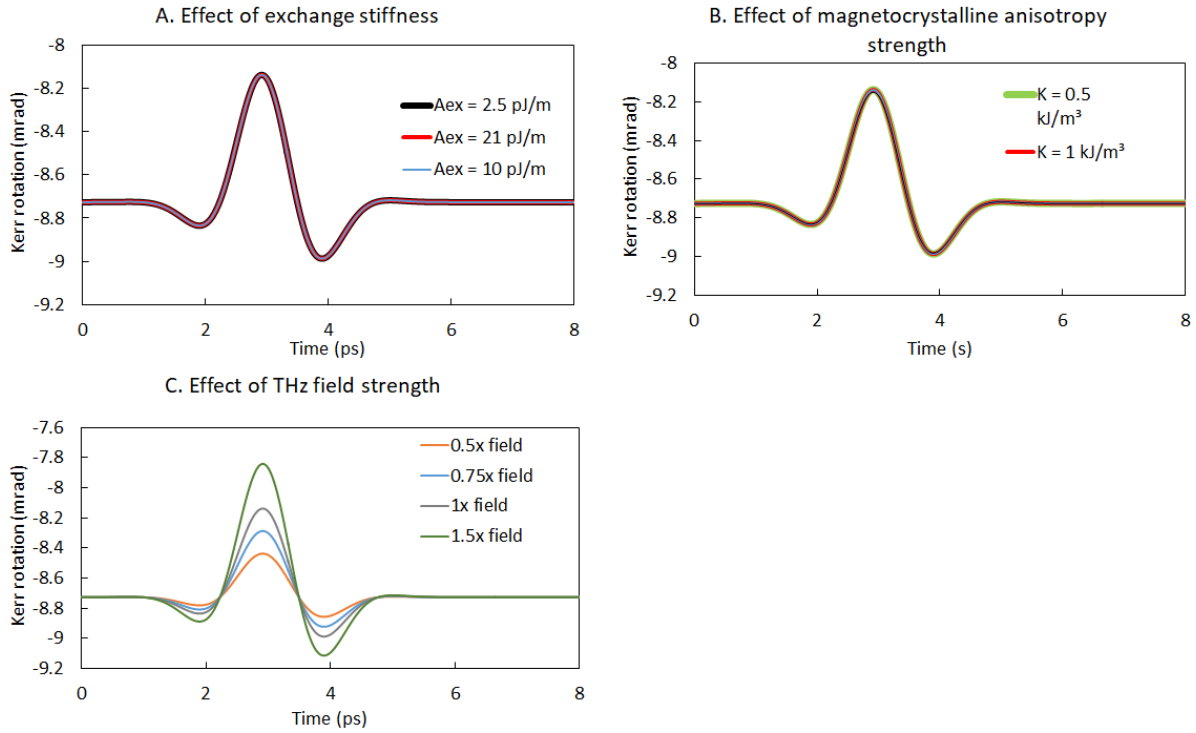

Figure 3.8: The effect of exchange stiffness, magnetocrystalline anisotropy, and THz field strength on the magnetization dynamics of a single-crystal Fe film. a) The exchange stiffness and b) the magnetocrystalline anisotropy strength do not affect the THz-induced magnetization dynamics. c) The strength of the THz field has a linear effect on the amplitude of the magnetization dynamics.

3.3.3 THz pump magnetization dynamics in the transverse geometry

The transverse MOKE geometry was used to measure the magnetic moment of a sample magnetized perpendicular to the direction of beam propagation. Unlike the polar and longitudinal geometries, transverse

MOKE does not induce a polarization rotation in the beam, but instead a change in reflectivity. However, in the case of a material magnetized in the transverse geometry, a polar/longitudinal MOKE signal can be observed if excited by a THz pulse, which will drive a component of the magnetization in either the polar or longitudinal direction or both. This behavior was observed experimentally for both crystalline and amorphous Fe films as shown in Figure 3.9.

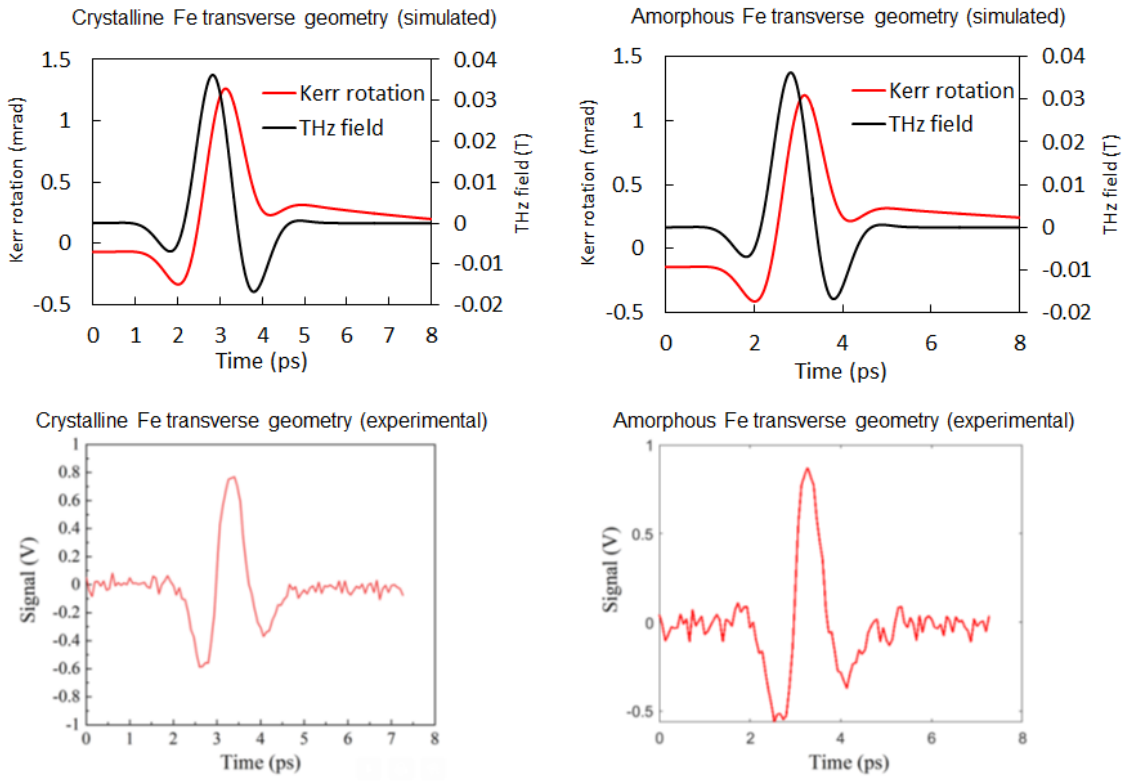

Figure 3.9: Magnetization dynamics of amorphous and crystalline Fe films in the transverse geometry: a) Coherent dynamics are observed following THz excitation of the epitaxial film. However, a higher delay from the THz pulse to the magnetization response is observed when compared to the longitudinal geometry (Figure 3.5). Stronger damping may need to be applied to model the now parallel B-field of the THz pulse. b) Similar dynamics are observed for the amorphous Fe film in the transverse geometry. c) The experimental dynamics of the epitaxial film excited in the transverse geometry. As with the simulation, coherent dynamics are observed in this geometry as well. d) The experimental dynamics for the amorphous film are similar to those of the epitaxial film.

THz-driven dynamics for transverse geometry was simulated using the Mumax code developed above. For the amorphous Fe thin film, the only difference was the change in the static field from the x-axis (parallel to beam propagation) to the y-axis (perpendicular). For the crystalline Fe thin film, some additional changes were required to account for the magnetocrystalline anisotropy of the material. Because the (100) and (010) planes of Fe are equivalent, both can be considered easy axes. Therefore, to model this system with uniaxial anisotropy, the direction of the magnetocrystalline anisotropy must also be switched to the y-axis. This

uniaxial assumption works well as long as the magnetization of the sample is considered to remain relatively close to the initial easy direction. As the absolute change in magnetization direction induced by the THz pump is small, and thus the magnetization is almost in the easy direction following THz excitation, this assumption was used for the simulations. The experimental and simulated magnetization dynamics for this geometry were shown in Figure 3.9. These results show that the overdamped LL equation is capable of accurately modeling the observation of dynamic polar/longitudinal MOKE in a transverse geometry. It is also interesting to note that the delay between THz pulse and the magnetization response in this case is increased from 80 fs to 300 fs, despite the overdamping being equal in both geometries ($\alpha = 30$). However, this delay needs to be experimentally confirmed. As the THz excitation pulse was not measured every time before the THz excitation, the exact delay between the THz pulse and sample response could have drifted slightly. For instance, the time delay of the peak of the THz pulse was found to vary as much as 1.3 ps during multiple days of measurement.

3.3.4 Dynamic hysteresis loops

While the magnetization dynamics of both single-crystal and amorphous Fe films are nearly identical in the time domain for both Mumax simulations and experiment, some differences arise when THz response is measured as a function of applied field. During the experiment, hysteresis loops were collected on amorphous and epitaxial single-crystal Fe films by incrementing a static field over the sample. This is similar to hysteresis loops measured under equilibrium conditions (referred to as static hysteresis loops in earlier sections), the only difference being, these dynamic loops are measured following THz excitation at a certain time delay. Figure 3.10 presents experimentally measured dynamic and static hysteresis loops which shows that dynamic hystersis loops are similar to static hysteresis loops for the crystalline films, but amorphous Fe films show somewhat higher coercivity with dynamic hysteresis. However, the repeatability of this effect on the amorphous film should be verified by further experiments.

To simulate these dynamic hysteresis loops, a static field is incremented between -400 to 400 Oe for both crystalline and amorphous films. At each static field, the system is allowed to relax using the Mumax relax() function before the THz pulse is applied. At the peak of the THz pulse (just before 3 ps), the magnetization of the sample is simulated. The THz field is then allowed to continue to run for a total of 6 ps, to ensure that any dynamics induced after the peak will be allowed to occur and to collect behavior over 6 ps. Following which, the static field is incremented and the system is allowed to relax again and the process is continued for all the field steps. Figure 3.10 compares these simulated dynamic hysteresis loops with those collected experimentally. The magnetization data in each loop is recorded at the peak of the THz field. Similar to

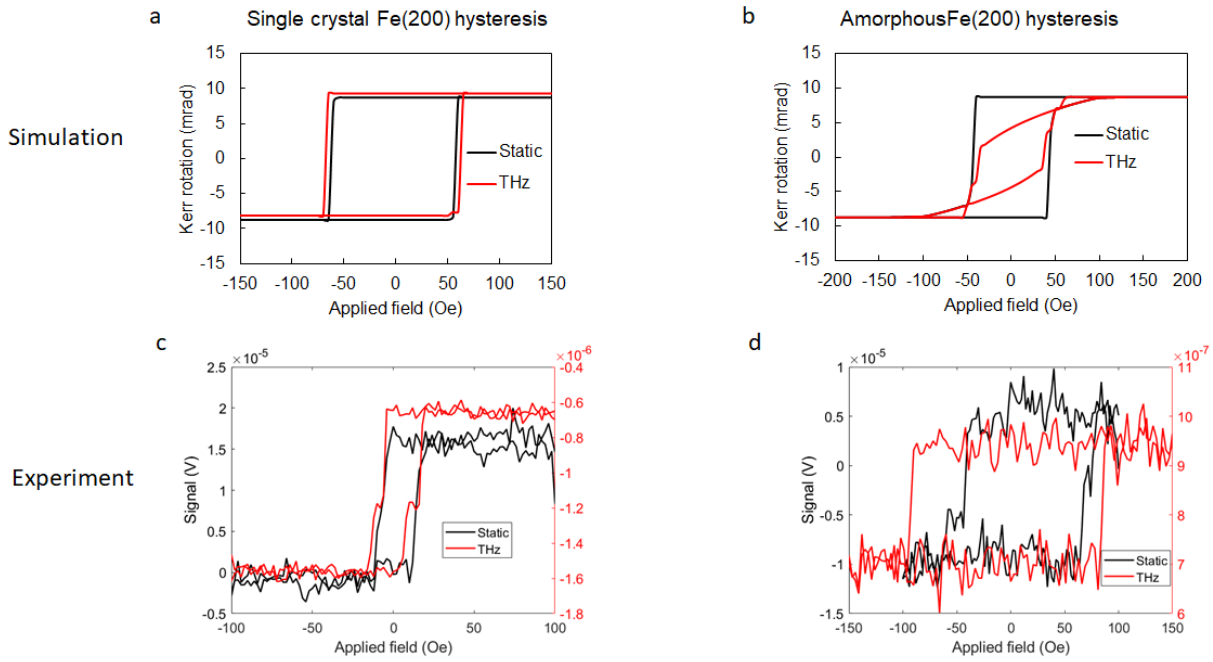

Figure 3.10: Dynamic hysteresis loops: Simulated dynamic hysteresis loops following THz excitation are compared with static hysteresis loops for both single crystalline (a) and amorphous (b) FE films. Similar hysteresis loops collected experimentally for single-crystal Fe (c) and amorphous Fe (d) are shown as a comparison. In each case, magnetization is recorded at the peak of the THz field. The slight asymmetry in the static hysteresis loop is caused by remanence in the electromagnet used to create the field.

what is observed experimentally, the dynamic hysteresis for single-crystal Fe is not significantly affected.

On the other hand, while the coercivity of the amorphous film appears to be slightly decreased, the most significant change in the hysteresis loop is the behavior at low applied fields. Even before reaching zero applied field, the THz field is able to significantly decrease the magnetic moment of the sample before switching occurs during THz-pumped hysteresis. This is in contrast to the increase in dynamic coercivity observed experimentally on amorphous films. The most likely cause for these simulated dynamics in the amorphous film are the lack of an easy magnetic axis. This means that there is little to prevent the THz Zeeman field from driving the magnetization towards itself, causing the magnetization vector along the applied field direction to decrease when the applied field is weak. This effect is illustrated in Figure 3.11 by looking at the directions of the spins in both the crystalline and amorphous films at critical points in the simulated hysteresis loop. In the epitaxial film, the magnetocrystalline anisotropy holds the magnetization in the easy axis direction until the coercive field is reached, which quickly flips the spins to the opposite easy axis direction, largely through out-of-plane motion. However, in the amorphous film, with no in-plane easy axis direction, the THz field is able to manipulate the spins into several domains with various in-plane magnetization directions when the applied field is sufficiently low, leading to the distinct simulated behavior

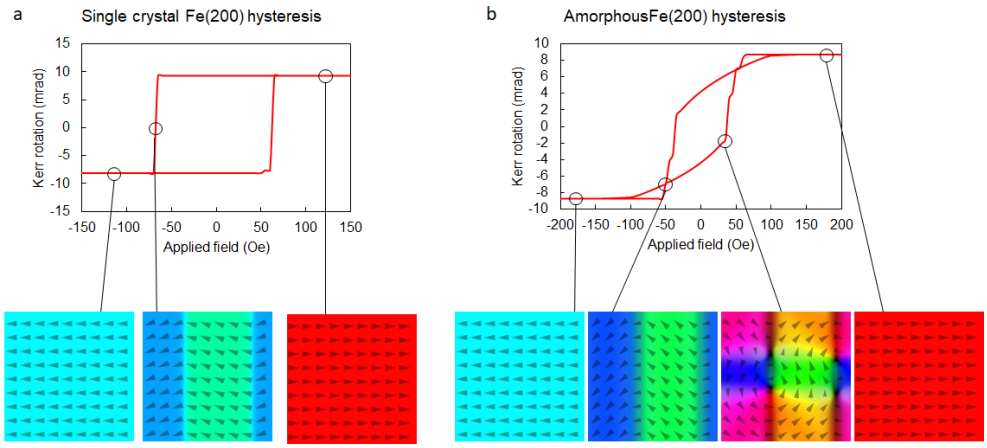

Figure 3.11: The spatial evolution of spins during dynamic hysteresis: a) The evolution of the spin structure of the epitaxial film during dynamic hysteresis. The magnetocrystalline anisotropy holds the in-plane component of the spins in the easy axis until the coercive field is reached, quickly flipping the spins to the opposite easy axis, causing the hysteresis loop observed to be similar to the static hysteresis behavior. b) The evolution of the spin structure of the amorphous film during dynamic hystereis. The lack of an in-plane easy axis direction allows the Thz field to manipulate the direction of the spins at low applied field, causing the unique behavior of the dynamic hysteresis in the simulated film. The arrows indicate the average in-plane spin direction across the depth of the film at their respective positions. Colors are used to differentiate magnetic domains.

of this film. While this model was successful for the epitaxial film, it is not sufficient to explain the observed dynamics in the amorphous film.

3.4 Conclusion

The overdamped LL equation has been demonstrated for modeling the ultrafast magnetization dynamics of Fe thin films pumped with ultrashort THz pulses. This is particularly evident in the time domain, where both single-crystal and amorphous films show magnetization evolution coherent with the B-field of the THz pulse both experimentally and in simulations. These dynamics are shown to be largely dependent on the field strength of the THz field, and not on the specific parameters of the magnetic material. This is in contrast to the normally-damped LLG equation, which does not show coherent dynamics in the geometry used in these experiments. The observed dynamics are found to be largely damping-driven, rather than precession-driven. The overdamped LL equation has now been shown to effectively model THz-pulse induced magnetization dynamics on elemental ferromagnetic films of Co and Fe. Despite the success of the overdamped LL equation in modeling the dynamics in the time domain, when a variable field is introduced, there are some observations that are not sufficiently treated by this model. For instance, while it is capable of reproducing the crystalline system well, it does not account for the increased coercivity of amorphous Fe films when pumped with THz

pulses in the longitudinal geometry. Further experiments will have to be done which carefully control the orientation to verify this result, and more advanced modeling techniques may be required to sufficiently explain this phenomenon.

Chapter 4

Optical laser-driven dynamics in LSCO across ferromagnetic to paramagnetic transition

This chapter investigates the ultrafast dynamics in an LSCO thin film across a ferromagnetic metal to paramagnetic semiconductor transition. In this chapter, I first layout the structural, magnetic and electrical characterization of the LSCO thin film as a function of temperature. Then, I present results of optical pump-probe studies on LSCO thin films where optical reflectivity was measured following 800 nm laser excitation on fs-ps timescales. The optical pump-probe studies were performed as a function of temperature across the ferromagnetic to paramagnetic transition. Finally, I compare the results to similar other perovksite systems.

4.1 Static characterization of LSCO thin film

An LSCO thin film (25 nm) was grown in the group of Professor Yayoi Takamura using pulsed laser deposition (PLD). The PLD growth conditions can be found in Rippy *et al.* [63]. Structural, magnetic and electrical characterization of $La_{0.7}Sr_{0.3}CoO_3$ thin film were performed to well characterize the ground state and the transition temperature prior to optical pump-probe measurements. X-ray diffraction (XRD) was performed to confirm that the LSCO was grown in the (100) orientation on the LSAT substrate, and the epitaxial nature was confirmed by Li *et al.* [64]. Magnetic behavior was measured using vibrating sample magnetometry by measuring magnetization as a function of temperature and field. The magnetization of the LSCO film was measured as a function of temperature during heat cycle in an applied field of 100 Oe. This was done from

low temperature to high temperature to mimic the temperature ramping (from low to high) that was used during optical pump-probe studies.

The results are presented in Figure 4.1. Figure 4.1 presents the x-ray diffraction showing the single crystal nature of the the deposited thin film. The magnetic moment gradually decreases as temperature is increased from 50 K. As Curie temperature is approached, the magnetization dropped more sharply, and finally above the Curie temperature the sample showed paramagnetic response. A Curie temperature of approximately 202 K was calculated based on the inflection point on the magnetic moment curve (Figure 4.1b.) Hysteresis loops were collected for several temperatures between 50-300K. Hysteresis behavior signifying ferromagnetic behavior was observed for temperatures below 200 K, while for temperatures above 200 K, linear paramagnetic response was observed. This further confirmed the magnetic phase transition occurring near 200K (Figure 4.1a). The electron transport option (ETO) of the vibrating sample magnetometer was used to measure the electrical resistance of the film as a function of temperature, with the same temperature range being used as for the magnetic moment curve. The resistance curve of LSCO has an inflection point at 200K, indicating that the metal to semiconductor transition occurs near 200K, which is approximately equal to the Curie temperature.

4.2 Optical pump-probe studies of LSCO thin film

Optical pump-probe studies of LSCO thin film were performed at the optical characterization facility in the Kukreja Laboratory. The wavelength of both the pump and the probe is 800 nm. A pump fluence of approximately 1 mJ/cm^2 was used. The diameter of the pump on the sample was 60 μm and that of the probe was 20 μm. The repetition rate of the pump and probe was 80 MHz. The penetration depth for undoped $LaCoO_3$ at 800 nm is $\approx$350 nm [65, 66], meaning the entire 25 nm sample is pumped and probed by the laser. The high degree of optical transparency of LSAT means substrate effects on the reflection should be minimized. Ultrafast optical transient reflectivity measurements were performed following the laser excitation for time delays of -8 ps to 200 ps as shown in Fig 4.2. These measurements were taken by sweeping the delay stage from -8 ps to 200 ps with a dwell time of 300 ms for each delay point. The step size for the delay stage is smaller for the lower time delays to capture faster dynamics with higher temporal resolution. Each curve was then collected 15-20 times and the averaged data was plotted. This process was repeated for different temperature values in the range of 5 K to 300 K as shown in Figure 4.2. This figure shows the full time delay of the transient reflectivity collected with each temperature being offset for clarity. Figure 4.3 shows the same data but only up to 12 ps of delay. This is to highlight the features at the beginning of the delay curve and show the relative amplitudes observed at each temperature. In each

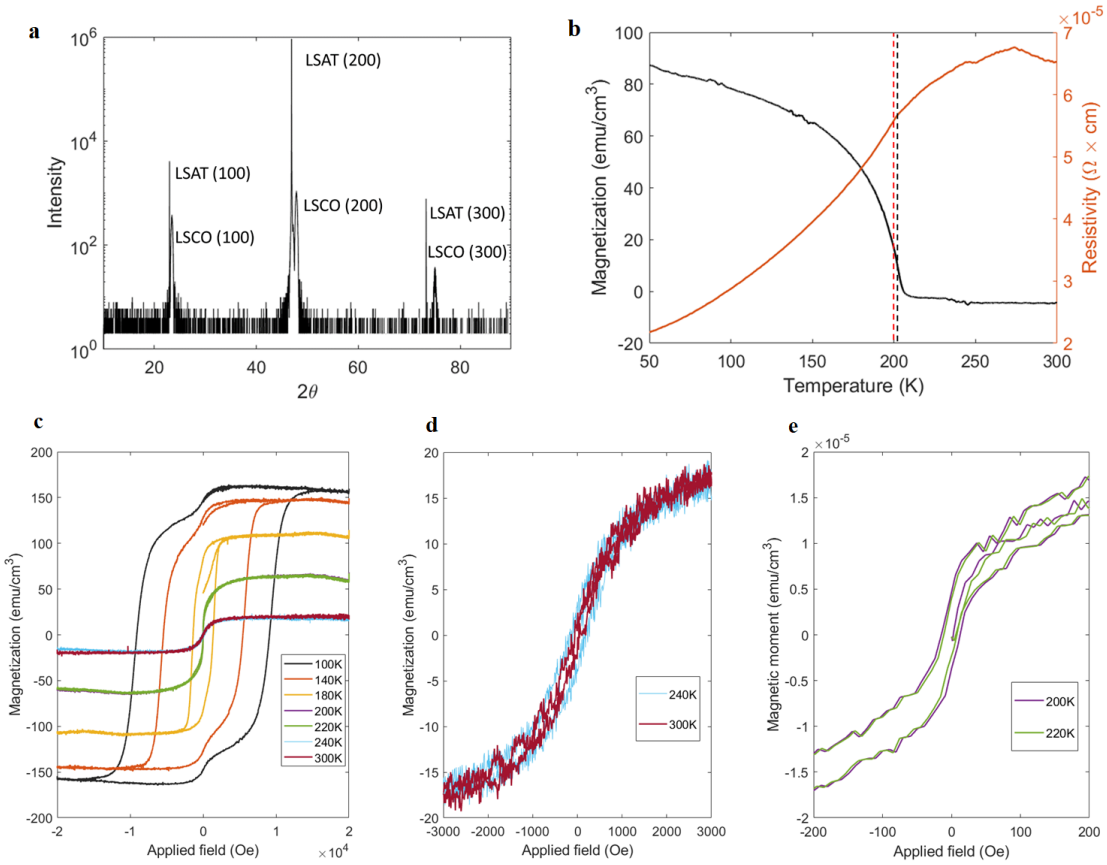

Figure 4.1: Structural, magnetic and electrical properties of LSCO: a) XRD of LSCO film showing the LSAT substrate and LSCO film (100), (200), and (300) peaks. b) Temperature dependent magnetic moment and resistance of the LSCO film. The black line shows a ferromagnetic to paramagnetic transition while heating the film in a 100 Oe field. The Curie temperature based on inflection point is estimated to be at 202K. The red line shows a metal to semiconductor transition at 200K. c) Hysteresis loops for LSCO between 100-300K. The curves up to 200K show ferromagnetic behavior, with the hysteresis loop being much more pronounced at lower temperatures. Beyond 200K, the behavior is much more linear and shows no hystersis, as expected from a paramagnetic material. d) Zoomed in figures showing LSCO hysteresis loops near and above the transition temperature (200-300K). By these temperatures, no appreciable hysteresis is observed. By 240K, the magnetization curve appears to be equal to that at room temperature (300K). e) Further zoomed in hysteresis loops to show slight difference between 200K and 220K.

figure, the points represent measured data, whereas the line is a fit which will be described later. It should be noted that negative time delay refers to the delay where probe arrives before the optical pump which provides information regarding the ground state. The flat behavior for the negative time delay implies that the film is fully recovered before the next excitation pulse arrives with a repetition rate of 80 MHz.

Figures 4.2 and 4.3 show that within the first ps following laser excitation, there is a sharp rise, followed by a fast decay within 1 ps as free carriers in the film are excited. This is followed by a slower rise (few ps) and subsequent decay followed by a longer decay back to equilibrium over 100s of ps. From Figure 4.3, it can be seen that for each temperature, similar features (presence of two peaks) are observed with no

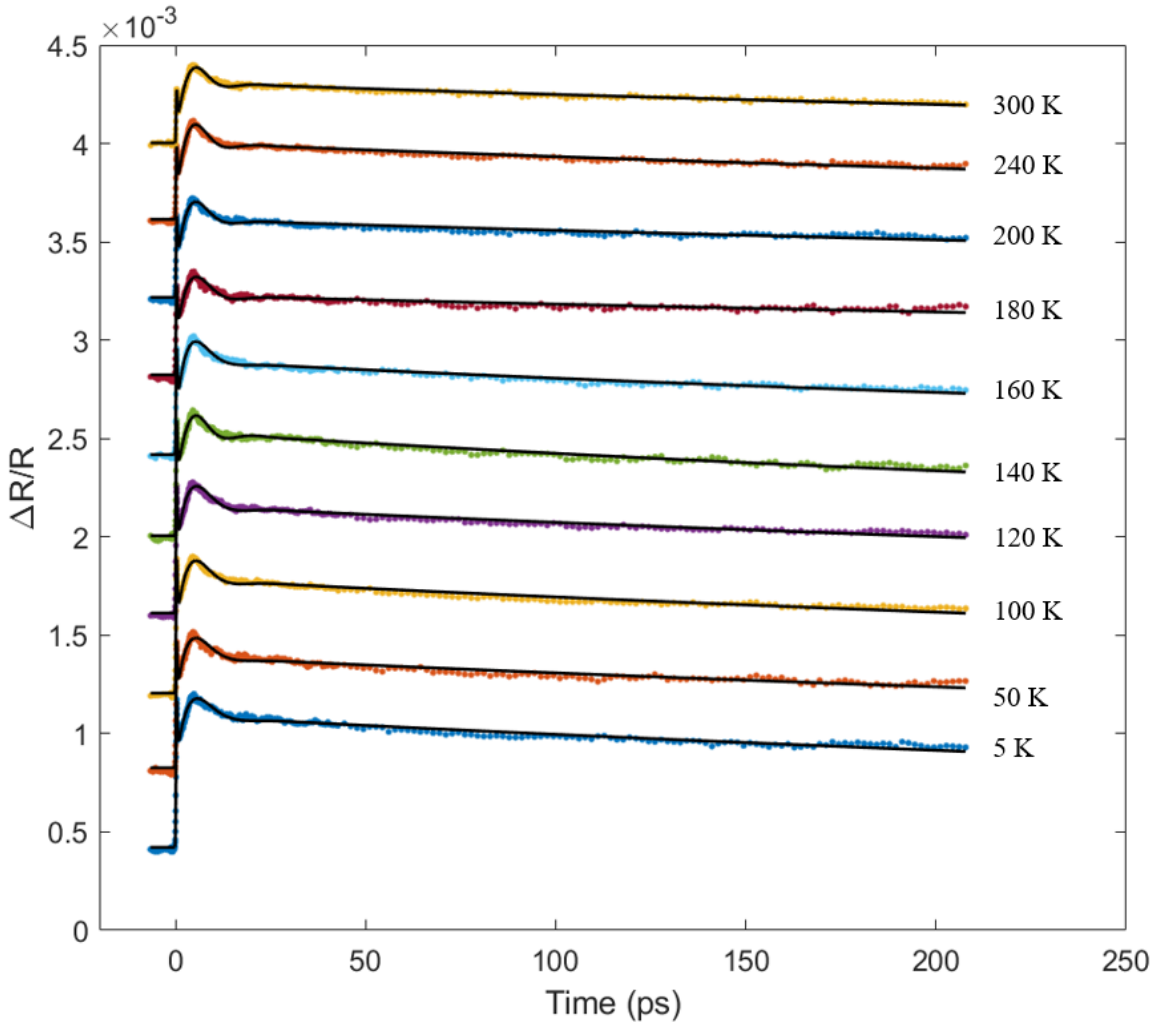

Figure 4.2: Transient reflectivity of the LSCO film: Transient reflectivity of the LSCO thin film at temperatures above and below the ferromagnetic to paramagnetic phase transition. This data was collected during heating cycle from 5K to 300K. The fit for this data (black line) was calculated using equation 4.1.

immediately obvious changes near the magnetic phase transition which is expected near a temperature of 200 K. However, the magnitude of the peaks as well as the ratio of the magnitude for the two peaks vary as a function of temperature. As the temperature increases, the magnitude of both peaks decreases, with a much stronger decrease observed in the magnitude of the first peak. These temperature dependent studies were performed using a cryostat to achieve the range of temperatures which accesses the phase transition. However, it should be noted that the measurement taken without the cryostat at room temperature (≈300 K) showed an additional weaker third peak after the second peak, which seems to indicate the presence of a strongly damped oscillating component in the signal. This data can be seen in Figure 4.4, with the additional oscillatory peak labeled with the arrow. The addition of the cryostat and the optical window of

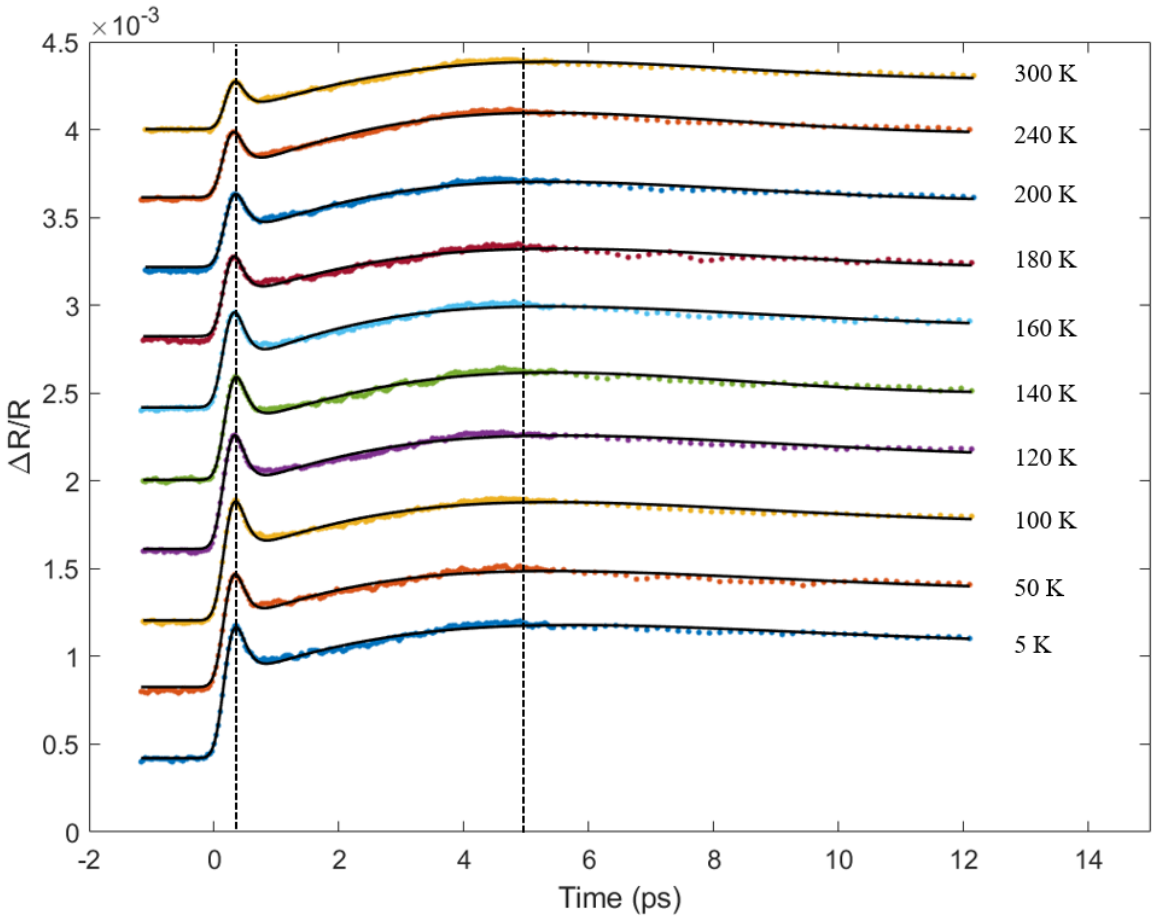

Figure 4.3: Transient reflectivity of LSCO at short time delays: Transient reflectivity of LSCO up to 12 ps time delay. The increase in signal amplitude with decreasing temperature can clearly be seen, as can the two peaks of the curve. The dashed lines show the location of the first and second peaks, which are largely unaffected by changes in temperature. The second peak is attributed to a polariton-phonon oscillation as described in other complex oxide materials [48, 67]

the cryostat likely attenuated this weak signal and this could be one of the reasons why it was not observed in Figure 4.2. It is also important to note that the LSCO film used without the cryostat was a different sample with a thickness of 34 nm. This difference in thickness may be another reason for not observing the third peak and also explains the slight shift (≈1.7 ps) in the position of the second peak with this sample.

Based on these observation, an oscillatory component was added to exponential decay fits to more accurately reproduce the data to extract time constants for the excitation and recovery processes. Two exponential functions, along with an oscillatory function multiplied to the exponential decay (to reproduce damped oscillations) were used for the fits as given by the equation below,

$$R(t) = \frac{1 + erf(t/\tau_r)}{2}[A_1 e^{(-t/\tau_1)} + A_2 e^{(-t/\tau_2)} + A_{osc} e^{-t/\tau_{DO}} sin(\frac{2\pi\omega_{osc}t}{1000} + 2\pi\phi)] \tag{4.1}$$

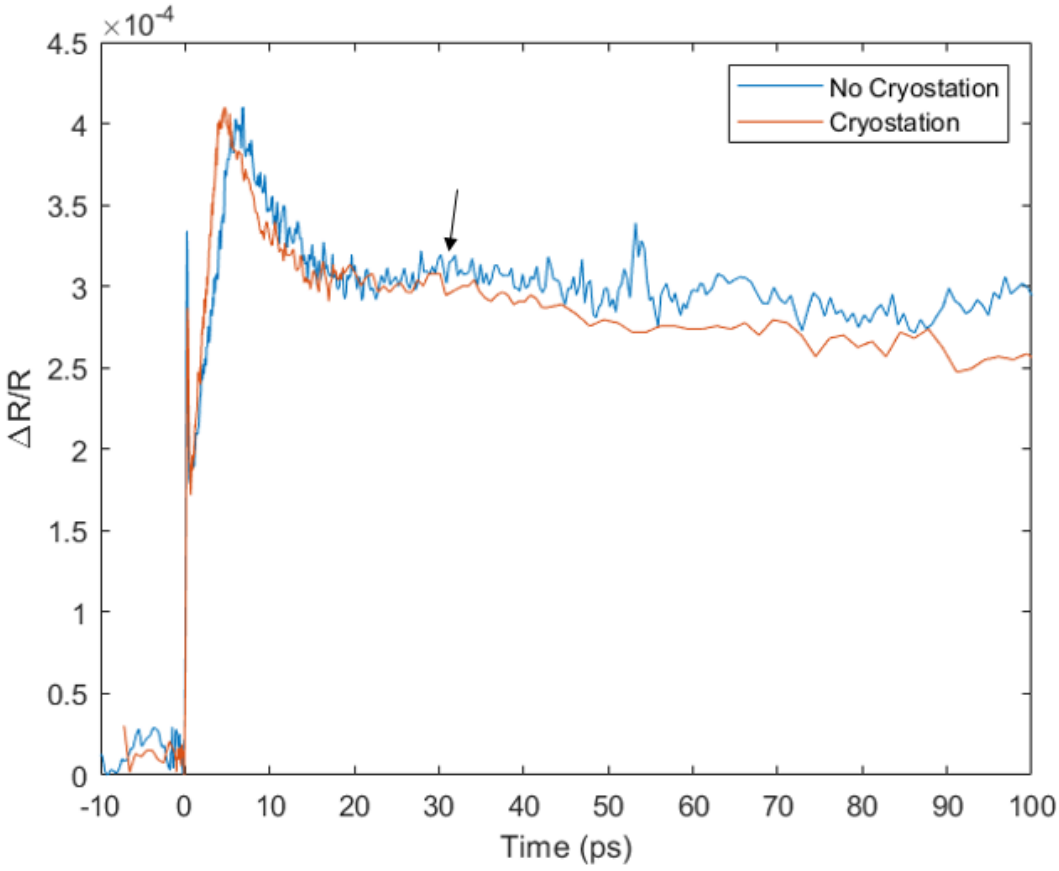

Figure 4.4: Transient reflectivity of two LSCO films: The transient reflectivity of two different LSCO films, a 25 nm film measured using cryostation, and a 34 nm film without the cryostat. With the cryostation removed, there is an additional weaker peak visible in the delay curve (black arrow), indicating that the second peak is likely due to an oscillating component. This additional peak is indicated with a red arrow. The slight offset in the delay of the second peak may be due to the different thicknesses of the films.

where $A_{1,2,DO}$ are the amplitudes of the fast (1) and slow (2) decays and the damped oscillation (DO), τ_r is the rise time, $\tau_{1,2,DO}$ are the decay times of the exponentials and oscillation, ω_{osc} is the oscillation frequency in GHz, and ϕ is the oscillation phase. The delay curves were then fit using a least squares curve fit in MatLab. Figure 4.5 shows each of the three components of the fit plotted separately to aid in the visualization of each of the fit components. The fitting parameters for each temperature are shown in Table 4.1.

It should be noted that various attempts were also made to fit the dynamics with only exponential decays without an oscillation, but none of these were capable of fitting with reasonable parameters or small enough error. Figure 4.6 shows the fit obtained using equation 4.1 and using a similar three exponential functions but with no oscillation. The exponential function was not able to model the behavior in detail, with the first peak being absent and the slow decay behavior significantly different than the data, indicating that

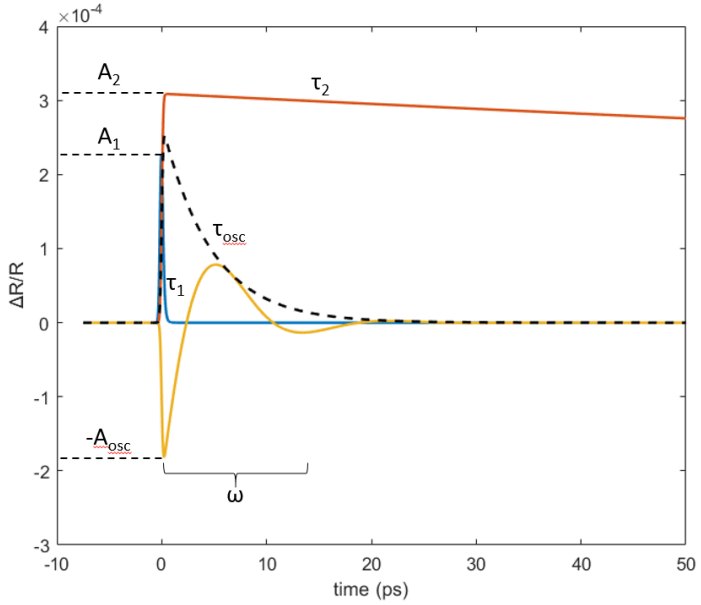

Figure 4.5: Components of the transient reflectivity fit: The blue curve (τ_1) is the fast decay responsible for the first peak of the delay curve. The orange curve is the long, slow decay (τ_2). The yellow curve is the decaying oscillation. The dashed line is the exponential decay portion of the yellow curve without the oscillation (this decay time is referred to as the oscillation decay (τ_{DO}) in this Chapter). The relevant fit parameters are labeled.

Table 4.1: Fit parameters obtained using equation 4.1 for transient reflectivity of LSCO

	$\mathbf{A_1}(10^{-5})$	$\mathbf{A_2}(10^{-5})$	$\mathbf{A_{osc}}(10^{-5})$	$\boldsymbol{\tau_1}$(fs)	$\boldsymbol{\tau_2}$(ps)	$\boldsymbol{\tau_{DO}}$(ps)	$\boldsymbol{\omega_{osc}}$(GHz)	$\boldsymbol{\phi}$
5K	103 ± 3	67 ± 0.5	42 ± 7	120 ± 6	658 ± 30	4.6 ± 0.4	39 ± 4	-0.08 ± 0.01
50K	91 ± 3	57 ± 0.5	45 ± 9	110 ± 8	627 ± 37	4.3 ± 0.4	39 ± 5	-0.07 ± 0.01
100K	98 ± 3	58 ± 0.4	38 ± 5	120 ± 6	582 ± 25	4.6 ± 0.4	46 ± 4	-0.09 ± 0.01
120K	95 ± 3	55 ± 0.4	40 ± 5	120 ± 6	587 ± 28	4.7 ± 0.4	44 ± 4	-0.15 ± 0.01
140K	86 ± 3	53 ± 0.3	27 ± 2	120 ± 8	423 ± 14	5.0 ± 0.4	63 ± 3	-0.08 ± 0.01
160K	84 ± 3	48 ± 0.4	47 ± 7	120 ± 8	483 ± 23	4.1 ± 0.3	39 ± 4	-0.09 ± 0.01
180K	69 ± 3	41 ± 0.4	33 ± 4	110 ± 10	844 ± 80	5.0 ± 0.5	48 ± 4	-0.11 ± 0.01
200K	65 ± 3	40 ± 0.4	34 ± 4	130 ± 10	653 ± 42	4.5 ± 0.4	52 ± 4	-0.13 ± 0.01
240K	58 ± 2	39 ± 0.3	33 ± 3	120 ± 8	489 ± 21	4.6 ± 0.3	58 ± 3	-0.13 ± 0.01
300K	44 ± 2	31 ± 0.2	27 ± 2	120 ± 10	438 ± 17	4.7 ± 0.3	60 ± 3	-0.14 ± 0.01

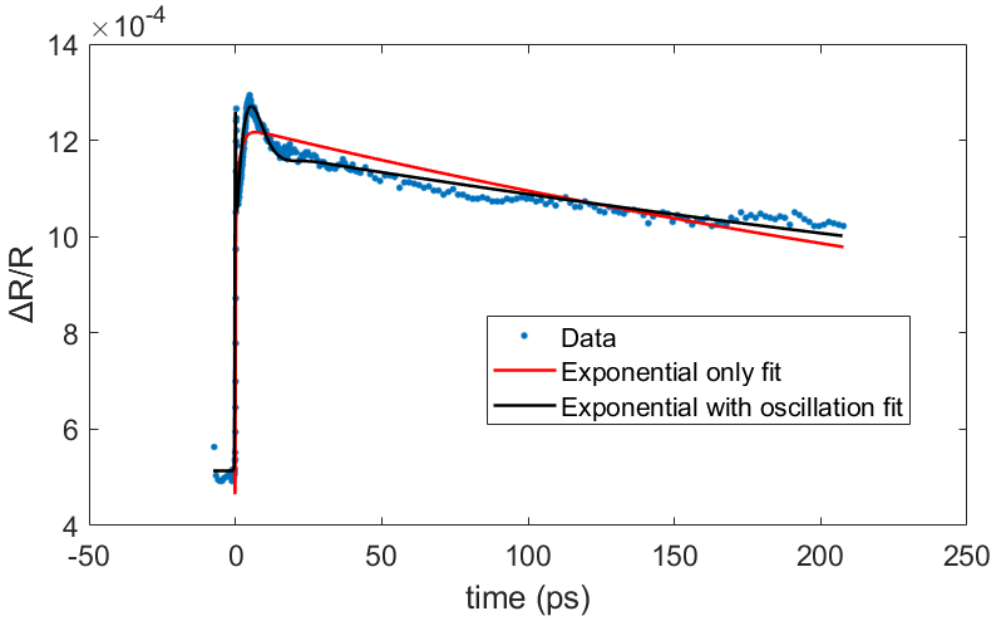

Figure 4.6: Transient reflectivity of LSCO at 5K fit with two functions: The transient reflectivity of LSCO at 5K is shown with two different fits. One (black) is the equation described in equation 4.1. The red fit uses the same equation, but without the oscillating component.

the second peak is caused by oscillatory dynamics. Similar behavior was fit for ultrafast spectroscopy of $La_{1-x}Ca_xMnO_3$ (LCMO) using the same function but with the sine function squared [67]. However, for this data, such a fit cannot appropriately capture both the rapid rise and rapid decay of the first peak due to the damped oscillation always being positive. However, Ren et al. [67] only fit the decay, which may have allowed for the use of this function. Attempts to fit the second peak separately using a double exponential function were also unsuccessful, indicating that the same excitation is responsible for the first and second peaks. It should be noted that beyond 50 ps the fits are somewhat less accurate. This may indicate that another slow relaxation processes might be occurring over longer timescales. It may also be caused by experimental drift which is the result of the pump beam moving unevenly through the probe beam as the delay is changed. This effect is more pronounced at lower temperatures.

In addition, the rise of the second peak and the exact peak position are not precisely fit using equation 4.1. This issue as well as the decreased accuracy beyond 50 ps, can be largely remedied by adding an additional exponential decay to the fit. This equation is given by

$$R(t) = \frac{1 + erf(t/\tau_r)}{2}[A_1 e^{(-t/\tau_1)} + A_2 e^{(-t/\tau_2)} + A_3 e^{(-t/\tau_3)} + A_{osc} e^{-t/\tau_{DO}} sin(\frac{2\pi\omega_{osc}t}{1000} + 2\pi\phi)] \qquad (4.2)$$

where $A_{1,2,3,DO}$ are the amplitudes of the fast (1) intermediate (2) and slow (3) decays and the damped

oscillation (DO), τ_r is the rise time, $\tau_{1,2,3,DO}$ are the decay times of the exponentials and oscillation, ω_{osc} is the oscillation frequency in GHz, and ϕ is the oscillation phase. The delay curves were then fit using a least squares curve fit in MatLab. The data fit with this additional exponential is shown in Figures 4.7 and 4.8. The values for the fitting parameters using this function are shown in Table 4.2. It can be seen that the addition exponential shows a decay time in the range of 5-15 ps dependent on temperature. This timescale was not captured in the previous equation 4.1 where the timescales were 120 fs and 400-800 ps for fast and slow processes respectively.

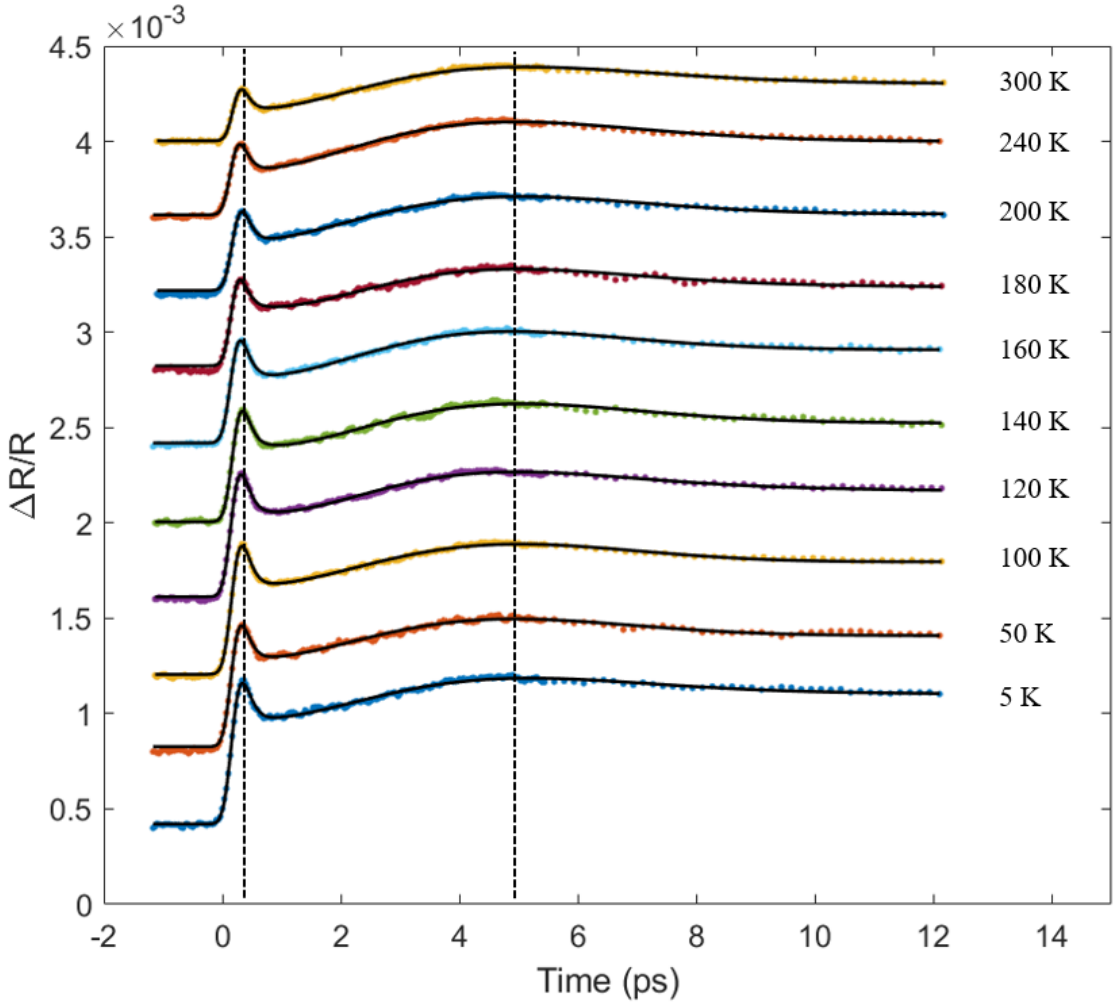

Figure 4.7: Transient reflectivity of LSCO fit with additional exponential: The data in this figure is the same as that of Figure 4.3 but fit with an additional exponential decay. This significantly improves the fit of the rise of the second peak and somewhat improves the fit peak position.

In order to investigate the evolution of amplitude and time as a function of temperature, Figure 4.9 shows the components of the fits plotted for each temperature extracted from equation 4.1 and shown in Table 4.1. Please refer to Figure 4.5 to visualize what each of these components represents. Each of the amplitudes

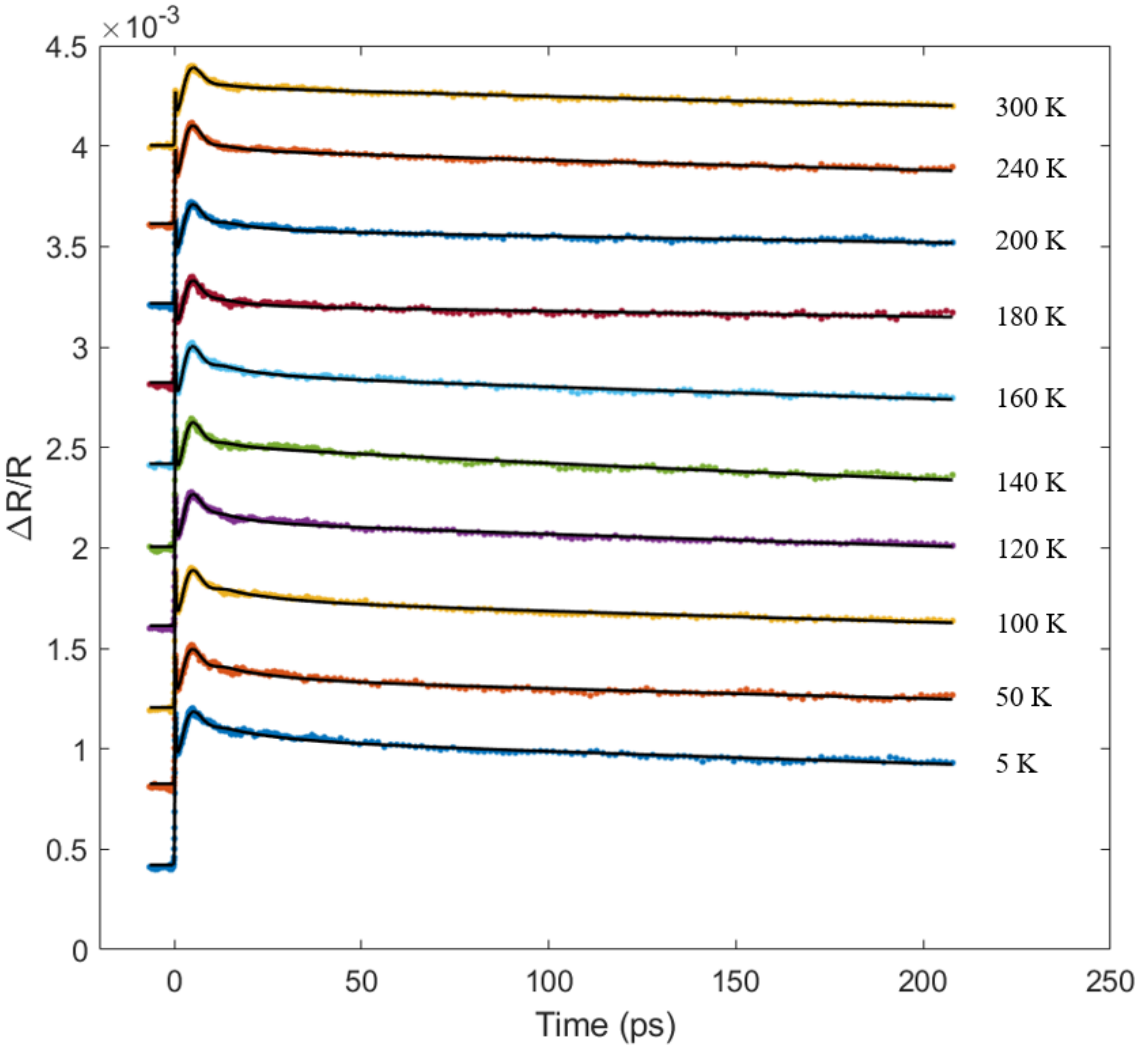

Figure 4.8: Full transient reflectivity fit with additional exponential: This is the same data and fit as Figure 4.7 shown over the full 200 ps collected. This fit is also more accurate over longer time delays when compared to the previous fit, but there is a risk of overfitting the data.

show a fairly linear temperature dependence, with higher amplitudes at lower temperatures. The frequency of the oscillation shows a slight temperature dependence, with greater frequency at higher temperatures; however, this increase is not very significant, and is likely due to the effect of changing lattice strain on phonon frequency between the film and the substrate as the temperature changes. Additionally, neither the amplitudes nor the frequency show any apparent change or sudden changes near the phase transition. The oscillation damping shows no dependence on temperature, but the long decay time does show interesting behavior near the transition temperature.

The decay constant for the slow decay (τ_2) decreases linearly from 5K to 120K (in the range of 600 ps, then drops at 140K, at which point it increases dramatically until 180K (up to 850 ps), before it begins

Table 4.2: Fit parameters using equation 4.2

	$\mathbf{A_1}(10^{-5})$	$\mathbf{A_2}(10^{-5})$	$\mathbf{A_3}(10^{-5})$	$\mathbf{A_{osc}}(10^{-5})$	$\boldsymbol{\tau_2}$(ps)	$\boldsymbol{\tau_3}$(ps)	$\boldsymbol{\tau_{DO}}$(ps)	$\boldsymbol{\omega_{osc}}$(GHz)
5K	92 ± 2	14 ± 1	63 ± 1	27 ± 3	15 ± 3	883 ± 72	3 ± 0.4	99 ± 6
50K	80 ± 3	14 ± 1	53 ± 1	24 ± 2	15 ± 3	901 ± 101	3 ± 0.4	105 ± 6
100K	87 ± 2	14 ± 1	54 ± 1	24 ± 2	14 ± 2	826 ± 56	3 ± 0.3	104 ± 4
120K	82 ± 2	17 ± 2	52 ± 0.5	33 ± 5	9 ± 1	727 ± 41	2 ± 0.3	104 ± 5
140K	75 ± 3	15 ± 4	51 ± 0.5	33 ± 6	6 ± 1	478 ± 20	3 ± 0.4	103 ± 5
160K	71 ± 2	14 ± 1	45 ± 0.5	29 ± 3	11 ± 1	603 ± 32	3 ± 0.3	106 ± 4
180K	57 ± 3	16 ± 3	39 ± 1	31 ± 6	8 ± 2	1241 ± 193	3 ± 0.5	104 ± 6
200K	57 ± 2	13 ± 1	37 ± 1	25 ± 2	11 ± 2	1035 ± 133	3 ± 0.4	98 ± 5
240K	49 ± 2	16 ± 3	37 ± 0.5	34 ± 5	6 ± 1	591 ± 30	3 ± 0.3	97 ± 4
300K	37 ± 2	15 ± 4	30 ± 0.5	33 ± 6	5 ± 1	510 ± 24	3 ± 0.3	93 ± 4

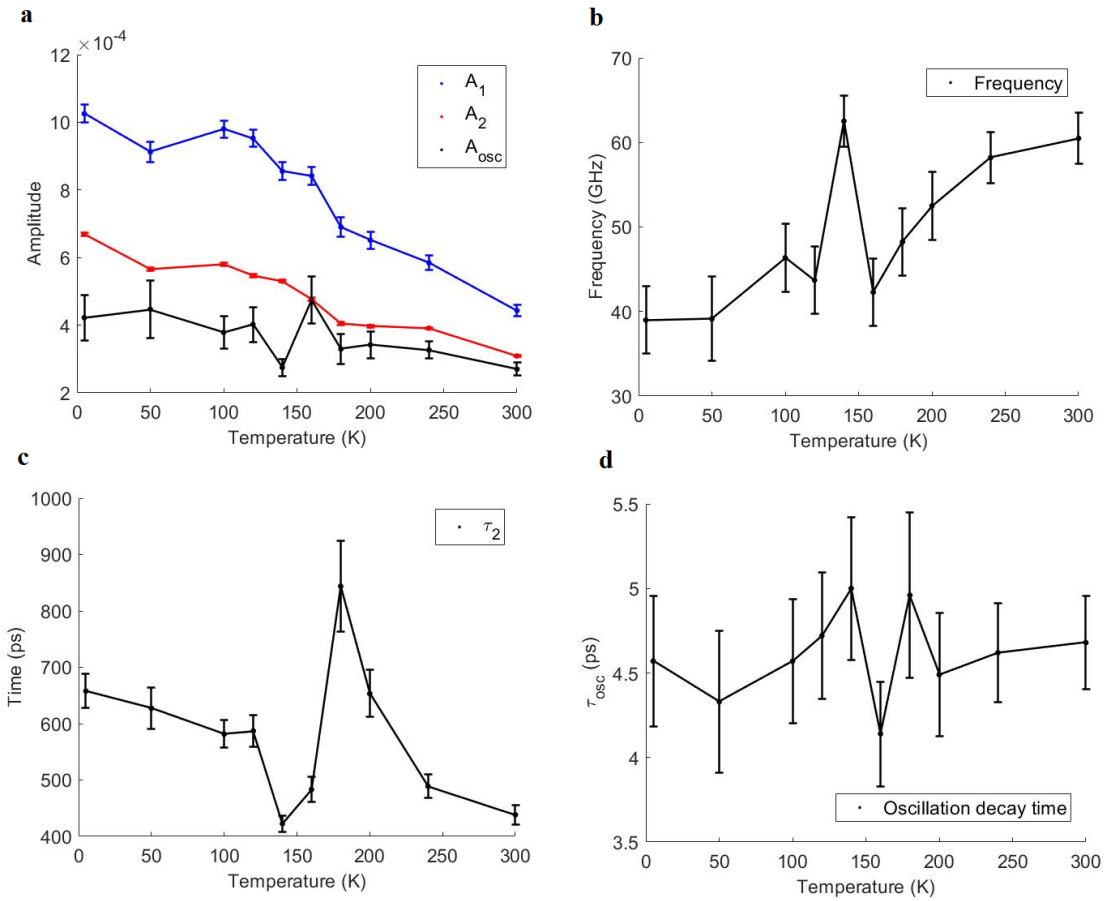

Figure 4.9: Fit parameters as a function of temperature: Each of the fit parameters are extracted from equation 4.1. a) The amplitude of the first decay (blue), second decay (red), and oscillation (black). In general, the amplitude decreases as the temperature increases. b) The fit of the frequency of the oscillation. Except for a spike at 140 K, the frequency appears to increase in a almost a linear manner as temperature increases. c) the decay constant of the second (slow) decay. The slow decay time gradually decreases until the phase transition temperature, where it suddenly increases before beginning to decrease with increasing temperature again. This is very likely due to a slow spin-state transition that occurs when the laser pump induces a magnetic phase transition in the LSCO film. d) The decay time of the oscillation. For all temperatures measured, there appears to be no temperature dependence on the decay time of the oscillation.

to resume a linear decrease near 240K. This change in relaxation behavior may be due to the electronic or spin-state transition which occurs between 180-200K. This would explain why this effect is only seen from 140-220K. At lower temperatures, there is insufficient pump energy for a photoinduced phase transition to occur, and at higher temperatures, the ground state is already in the paramagnetic phase. This effect is likely observed at lower temperatures than the phase transition (beginning at 140K) due to the heating effect of laser-absorption or photo-induced transition. The temperature of the photoexcited LSCO film can be estimated using:

$$Fluence(mJ/cm^2) = \rho(g/cm^3) \times Thickness(cm) \times C_p(mJ/g \times K) \times \Delta T \tag{4.3}$$

The density of the LSCO film can be calculated from the chemical composition of the LSCO film and the out-of-plane lattice parameter which was previously measured as 3.805 angstrom [68]. This gives a density of 6.9 g/cm^3 for the LSCO film, which is slightly greater than that reported for the closest available bulk stoichiometry of $La_{0.6}Sr_{0.4}CoO_{0.3}$ (6.22 g/cm^3). As no data for the heat capacity of LSCO exists, we estimated the temperature using the heat capacity of $LaCoO_3$, one of the parent compounds of LSCO. This was calculated across a range of temperatures by Shu *et al.* [69] and was found to be equal to about 70 J/mol $*$ K at the Curie temperature of 202K. This corresponds to a C_p of 306 mJ/g $*$ K. With a film thickness of 25 nm and a pump fluence of 1 mJ/cm^3, the change in temperature of the film is calculated to be 20 K. While this value overestimates the change in temperature by ignoring the reflection, it is still in line with the observed optically-pumped magnetic phase transition temperature being about 180 K, compared to 202K when measured statically.

The fit parameters of the four exponential fit are shown in Figure 4.10 which were extracted using equation 4.2 and presented in Table 4.2. The amplitudes shown in Figure 4.10a maintain a trend of either generally decreasing with increasing temperature, or not varying significantly. Interestingly, the additional intermediate exponential decay (Figure 4.10b) exhibits a slight decrease in decay time above 120 K. The frequency (Figure 4.10e) is higher (100 GHz) than that observed with the three exponential fit, and does not seem to vary substantially with temperature. The slow decay time in Figure 4.10c (τ_3 in this case) maintains the same trend as with the three exponential fit, but occurs over slightly longer timescales. The oscillation damping parameter (Figure 4.10d) is somewhat faster with the four exponential fit, but continues to show no significant temperature variation. Figure 4.10f shows the individual components of the fit given by equation 4.2. The blue curve represents the initial fast decay responsible for the first peak (τ_1). The orange curve is the new exponential in the four component fit (τ_2). The purple curve is the damped oscillation and the yellow curve is the long decay (τ_3).

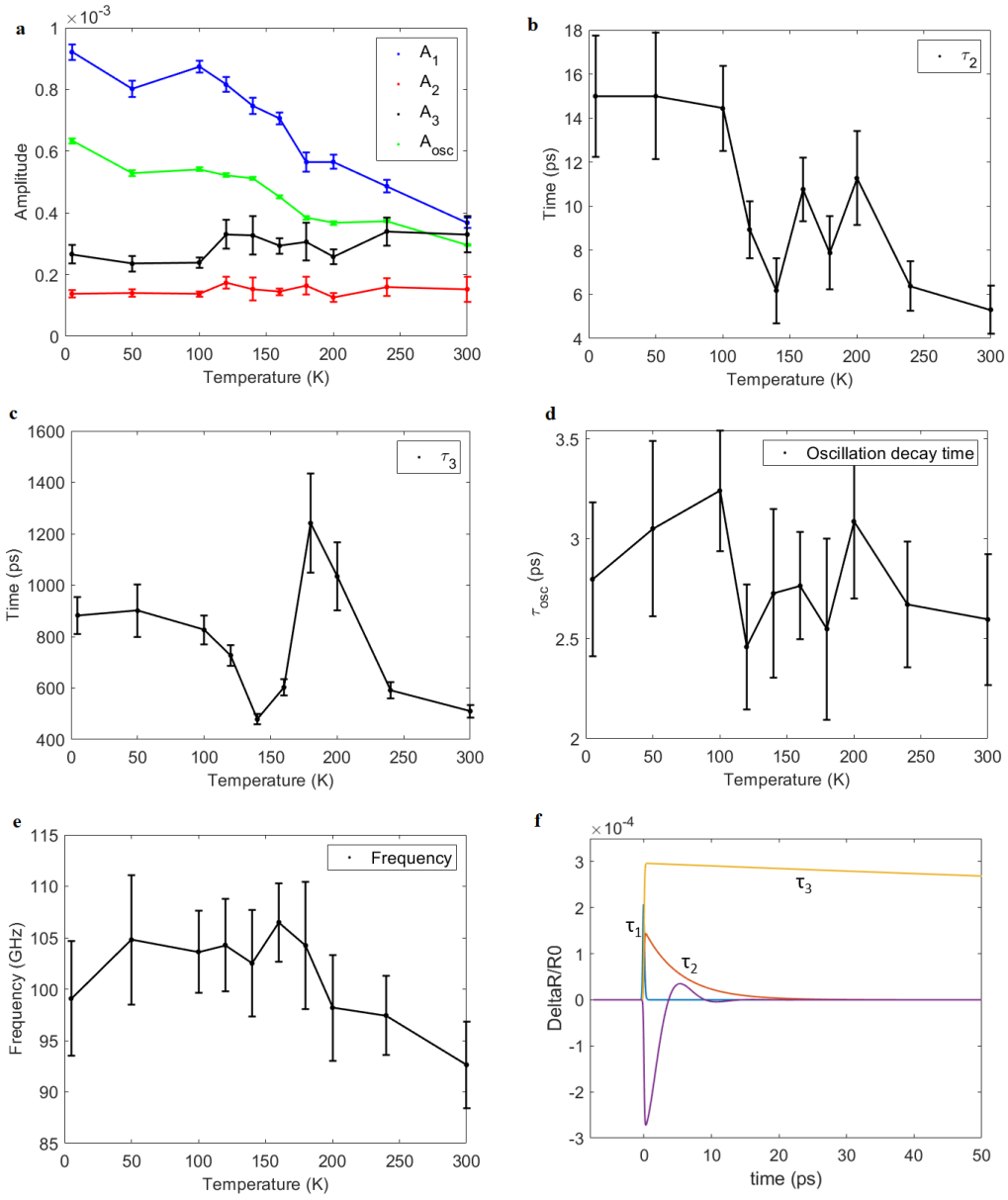

Figure 4.10: Selected components of the four component fit: a) The amplitudes of the three exponentials and the damped oscillation. b) The decay time of the new exponential (τ_2). This decay occurs on the order of the initial decay of the second peak. c) The long decay time, τ_3. As with the three component fit, there is a decrease in τ_3 immediately before the transition temperature, and a sharp increase at the transition temperature. d) The damping parameter for the damped oscillation is somewhat faster than that observed with the three component fit. e) The frequency of the damped oscillation. In the four component fit, the frequency is higher than that of the three component fit, but shows no significant temperature dependence. f) The four components of the fit plotted separately. The error bars for each component are calculated as 95% confidence intervals from the least square analysis.

4.2.1 Discussion

The observed dynamics in the LSCO thin film is similar to those observed for other perovskite oxide thin films such as $NdNiO_3$ (NNO) [48], $La_xCa_{1-x}MnO_3$ (LCMO) [67], $La_xSr_{1-x}MnO_3$ (LSMO) [70, 71], and $Gd_{0.5}Sr_{0.45}MnO_3MnO_3$ [46], with a few key differences. It should also be noted that different interactions between films and substrates could affect the comparisons between these materials. For instance, substrate clamping has been shown to constrain thermal expansion of thin films to the out-of-plane direction, which can alter the structural as well as magnetic and electronic properties of compelx oxide materials [72, 73, 74, 75]. However, these effects require careful studying of the substrate and the film and have not yet been extensively considered. The transient reflectivity of NNO and LCMO are shown in Figure 4.11 for reference. The fast initial decay of LSCO within a ps is similar to that observed in similar materials such as NNO (τ=0.5 ps) [48], LCMO [67] (τ=0.5-4 ps), LSMO [70] (<1 ps), and $Gd_{0.5}Sr_{0.45}MnO_3MnO_{33}$ (<1 ps) [46]. However, for both LCMO and NNO, the magnitude of the first peak demonstrates critical behavior at the transition temperature. For instance, in LCMO, the intensity of the first peak reaches a maximum at the transition, and in NNO, the intensity shows a sharp decrease at the transition temperature. In the LSCO film studied here, there is only a general decrease in the peak intensity as the temperature increases, with no change in the trend at T_C. In LCMO, the intensity of the first peak peaking at the transition temperature was attributed to Jahn-Teller distortions in the insulating phase whose energy aligned with that of the pump pulse [67]. In the experiments done on NNO, there is no absorption band overlapping the pump energy; however, the critical behavior is attributed to a "bottleneck effect" where excited carriers pile up at the bottom of the excitation band, although this theory was not confirmed [48]. The lack of abrupt changes in amplitude could be potentially due to the fact that LSCO the phase transition from ferromagnetic metal to paramagnetic insulator while in NNO the phase transition is from antiferromagnetic insulator to paramagnetic metal. In addition, both LSMO [76] and NNO [77] are known to undergo structural transitions at the magnetic transition temperature; however, this has not yet been investigated in LSCO. If no structural transition is present in LSCO at T_C, this may also play a role in the lack of critical behavior observed in the amplitude of the LSCO transient reflectivity.

The second, oscillatory peak has also been observed in LCMO [67] and NNO [48] and was attributed to polariton-phonons, a quasi-particle in which a phonon mode in the material couples to the electromagnetic field of the laser pulse. However, the presence of a secondary oscillatory peak after the initial excitation was only observed in higher temperature phases for NNO, (see Figure 4.11), whereas in LCMO and LSCO, this feature was observed in both the high and low temperature phases. For NNO, the disappearance of the second peak was attributed to its being obscured by the increase in the amplitude of the first peak,

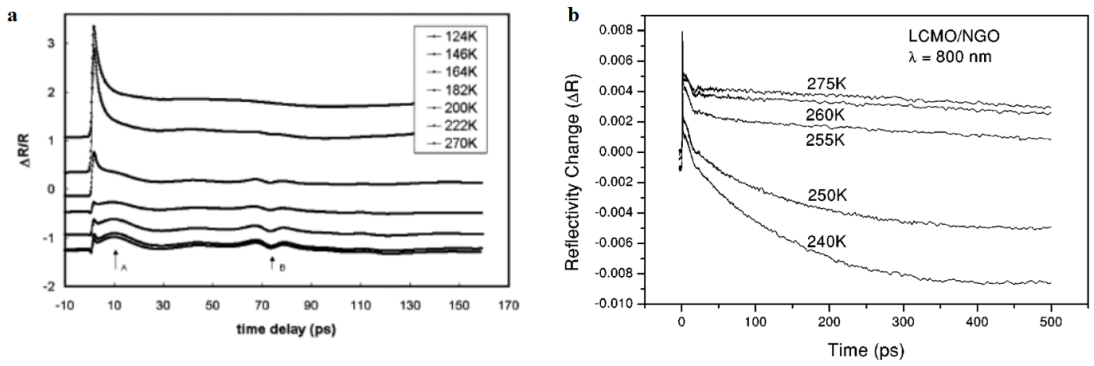

Figure 4.11: Transient reflectivity of NNO and LCMO: a) Transient reflectivity of NNO across the antiferromagnetic insulator to paramagnetic metal transition [48], with temperature decreasing moving up the plot. The presence of an oscillatory mode, attributed to a polariton-phonon is observed in the higher temperature phase, but not the lower, due to the increase in amplitude of the initial excitation. This is in contrast to what we observe in LSCO, with the oscillatory mode being present in both phases. b) Transient reflectivity of LCMO above and below the transition temperature (255 K) [67]. The low temperature phase contains a negative amplitude component that persists over long timescales (up to 1 ms), which is distinct from what we observe for LSCO. For both phases, a polariton-phonon oscillation is observed, as is the case for LSCO.

however the increase in the amplitude of the first peak does not show such critical behavior for LSCO. In LSMO, similar oscillations are observed but are much stronger and less damped, and were attributed to longitudinal acoustic phonons [71]. To better determine the source of this oscillation in the LSCO film, a higher intensity pump would be needed to resolve additional peaks. This would allow for a more accurate determination of the beating period of this mode, which would indicate the polariton or phonon character of the oscillation. However, using the oscillation frequency from equation 4.1, an estimate of 40-60 GHz can be obtained. Coupled with the strong damping observed in LSCO, this would be consistent with a strongly polariton-like polariton-phonon mode according to Ren *et al.* [67]. However, unlike Ren *et al.*, no softening of the oscillation is observed near the Curie temperature. Additionally, the second peak of the 34 nm LSCO film measured without the cryostation is slightly delayed relative to that observed for the 25 nm LSCO film discussed here. Although further investigation would have to be conducted with several film thicknesses, this may indicate that the oscillation is caused by a longitudinal acoustic phonon, whose frequency is a function of the thickness of the film.

An interesting feature of the ultrafast dynamics of the LSCO film is the timescale of the slow decay (τ_2), which ranged from 438 ± 17 ps to 844 ± 80 ps for LSCO and showed critical behavior that was not observed in other similar materials. In the case of LCMO, this decay occured over a timescale of 100s of μs [67], whereas in $Gd_{0.5}Sr_{0.45}MnO_3MnO_{33}$, this decay occurs in as little as 4 ps, with separately measured spin dynamics occuring on a timescale of 50 ps [46]. Additionally, the long decay of LCMO in the ferromagnetic metal phase has a negative amplitude, causing $\Delta R/R$ to be negative well after a 1 ms delay time [67]. Experiments

on NNO did not measure the exact decay time of the slow component, but estimated it to be in the hundreds of ps range, similar to what we observe for LSCO; however, the phase transition investigated in NNO was from an antiferromagnetic insulator to a paramagnetic metal. For LCMO and LSMO materials, a slowly decaying component that drives δR negative over a 100 ps to ms timescale is attributed to a slow spin-lattice relaxation [67, 70], and a similar spin-lattice relaxation has also been proposed as an explanation for the slow decay dynamics of NNO [48]. Thus, this slow timescale in LSCO potentially corresponds to spin-lattice relaxation timescales. It should be also noted that the temperature range for the dramatic increase in τ_2 is consistent with a spin state transition, occurring near the Curie temperature of the LSCO film. However, it is possible that this trend is simply due to thermal effects or additional factors that supercede the spin state transition at T_C. Further, detailed measurements with sample thickness, doping and fluence would be needed to substantiate this idea. On the other hand, when considering the four exponential fit, the decrease in τ_2 at 120 K remains unexplained. While there is no electronic or magnetic phase transition in this temperature range, there may be a potentially transient change in the electronic structure induced by the pump beam. LSCO and similar materials show multiple spin states for Co^{3+} and Co^{4+} as well as Jahn-Teller distortions in the Co electronic bands [78] following laser excitation. Again, while a change in either of these may be responsible for this observation, further research would need to be done on the system.

4.3 Conclusion

In conclusion, the ultrafast dynamics of the ferromagnetic paramagnetic phase transition of $La_{0.7}Sr_{0.3}CoO_3$ were investigated. Across both phases, a sub-ps excitation was observed with a quickly decaying oscillation. This oscillation is likely a polariton-phonon mode as is observed in transient spectroscopy of several other perovskite oxides. The height of the first peak and the oscillation peak are found to be strongly dependent on temperature, but with no apparent difference for the two phases. However, the relaxation back to equilibrium, which occurs over several hundred ps is found to be strongly influenced by the phase transition, with the decay time constant growing from 500 ps to over 800 ps during the transition. This decay timescale is significantly longer than similar magnetic perovskite oxides, and the increased relaxation time during the phase transition may be due to a slow spin state transition. However, the strong overlap of electronic, structural, and magnetic properties in correlated materials like LSCO means further experiments with other techniques would be required to more clearly elucidate the mechanisms of this phase transition.

Chapter 5

Summary and Future work

Understanding the dynamics of magnetism at ultrafast timescales is critical for advancing spintronic and magnetic memory applications, especially as these technologies move towards higher speeds. An important area of current research is investigating methods to control magnetism and modify magnetic properties at ps and sub ps timescales. In this thesis, I used micromagnetic simulations to investigate the magnetization dynamics of single-crystal and amorphous Fe thin films pumped with ultrashort THz pulses, as well as the ultrafast dynamics across a ferromagnetic to paramagnetic phase transition in an LSCO thin film. Ultrashort THz pulses have been shown experimentally to coherently modify the magnetization of ferromagnetic films, including the Fe films considered in this thesis. While the traditional LLG equation is not able to capture the coherent dynamics observed in these Fe films, renormalizing and overdamping the LLG equation, as has been suggested for systems where the THz B-field is perpendicular to the sample magnetization, successfully captures the ultrafast dynamics, provided that no demagnetization is observed. In our studies, for both amorphous and crystalline films, the evolution of the magnetization on a ps timescale is identical in both phase and magnitude, and no demagnetization was observed in either material. The magnitude of the magnetic response to THz pulses was also found to depend linearly on the strength of the THz pulse, and was not dependent on the magnetic hardness of the material. Despite the success in modeling time-dependent dynamics, the field dependent dynamics for amorphous Fe could not be matched using the overdamped LL equation.

The ultrafast dynamics of an LSCO thin film across a magnetic phase transition revealed behavior distinct from that observed in other perovskite oxide materials. While excitation dynamics occur on a sub-ps timescale, similar to other materials, relaxation timescales are substantially longer than those of LCMO and $Gd_{0.5}Sr_{0.45}MnO_3MnO_{33}$, and on the same order as those of NNO. Interestingly, when the relaxation

occurs across the paramagnetic to ferromagnetic transition, the relaxation time increases sharply, likely indicating a slow spin state relaxation occuring over several hundred ps. Further experiments such as time-resolved MOKE should be able to further elucidate the interplay between the electronic and magnetic states of LSCO during the induced phase transition and relaxation.

5.1 THz-driven magnetization dynamics in metallic thin films

While the work presented here shows that the field-independent time-domain magnetization dynamics of Fe films pumped with ultrashort THz pulses is independent of crystallinity, there are still questions that remain to be answered. In this thesis, no demagnetization was observed for either crystalline or amorphous Fe, showing that THz-induced demagnetization does not depend solely on the crystallinity of the film. However, the root cause of the ultrafast demagnetization sometimes observed remains unknown. It may well be a function of THz fluence and a combination of factors related to the chemical makeup of the studied material, as it has thus far only been observed in metallic alloys such as CoPt [24] and CoFeB [22, 23]. Studies on single-element systems such as the Fe films investigated here with varying THz field strength should be able to give an indication of whether THz fluence can cause demagnetization in such a material, or if the phenomenon is strictly tied to multi-element systems. The THz-driven magnetization dynamics of multilayer ferromagnetic thin film systems may also uncover novel dynamics, and has not yet been studied.

Another area for future research would be to compare crystalline and amorphous film dynamics using the inertial LLG (ILLG) equation. The ILLG equation has recently emerged for modeling magnetization dynamics on the ultrafast timescale. The ILLG equation introduces a nutation frequency to account for the fact that angular momentum may be out of equilibrium during ultrafast dynamics, but must still be conserved. This can be thought of as a rocking frequency that occurs during precession. The ILLG equation takes the form

$$\frac{d\mathbf{M}}{dt} = \gamma \mathbf{M} \times [\mathbf{H_{eff}} - \eta(\frac{d\mathbf{M}}{dt} + \tau \frac{d^2\mathbf{M}}{dt^2})] \tag{5.1}$$

where η is similar to the Gilbert damping coefficient α from the LLG equation, and τ represents a nutation time. This model has been succesfully applied to model modifications to ferromagnetic resonance that could occur at THz frequencies [33], however the solution for this equation is much more complex than that of the LLG equation.

All of the simulations presented in this thesis consider crystalline Fe as having uniaxial magnetocrystalline anisotropy; however, in reality, single-crystal Fe has cubic anisotropy with easy, medium, and hard axes. Experimental research has been done on the THz-induced magnetization dynamics of single-crystal

Fe magnetized along both the easy and medium directions. Simulations which take into account the cubic anisotropy of Fe would be able to model those dynamics in both the time and field domains, as has been done for the easy axis in this thesis.

5.2 Future avenues for ultrafast magnetization in LSCO

There are still many avenues remaining to explore the ultrafast phase-transition dynamics of LSCO. This thesis lays out one of the first optical pump-probe studies performed on LSCO. However, detailed measurements are required to fully understand the ultrafast behavior of LSCO thin films. An interesting experiment would be to disentangle the spin and electron systems during the transition. Transient reflectivity primarily gives information about the electronic state of the material, particularly for electrons near the Fermi level. In order to obtain information about the spin state of the sample, time-resolved MOKE spectroscopy could be performed. For such an experiment, the sample would be placed in a magnetic field, before being pumped by the laser. The probe beam would then be allowed to pass through a Wollaston prism before being collected on a balanced diode, similar to measurements described earlier in this thesis for Fe thin films. Such a setup would give a signal proportional to the polarization rotation of the probe pulse, which is proportional to the magnetization of the sample via the magneto-optic Kerr effect. This would be particularly interesting in this experiment as it would allow us to track the transition from a ferromagnetic to a paramagnetic state (and vis-versa during relaxation) independent of any electronic-state transitions. Similar experiments have been done on $Gd_{0.55}Sr_{0.45}MnO_3$ [46]. The lattice degree of freedom during the phase transition could also be explored using time-resolved XRD. With the advent of x-ray free electron lasers, such a measurement could be performed with sub-ps time resolution [79, 80]. While NNO [77] and LSMO [76] are both known to exhibit structural changes at T_C, this has not yet been investigated in LSCO. Because of the strong correlation between lattice, spin, orbital, and charge in complex oxide materials, a differing timescale for each degree of freedom during a phase transition may lead to a transient state with properties not observed at thermodynamic equilibrium.

Another aspect that remains unexplored is the degree to which the phase transition can be driven by an optical pump. This could be resolved by performing experiments in which the pump fluence incident on the sample is varied. This would, however, require an amplifier to allow the pump fluence to reach values beyond those currently accessible with only an oscillator cavity. An increase in the pump fluence would also allow additional oscillation peaks to be resolved. By measuring the effect of film thickness on the frequency of the oscillation, the source of the oscillation could be determined. If it is in fact a polariton phonon, then the film thickness should have no effect on the frequency. However, if the oscillatory mode is a

longitudinal acoustic phonon, then the beating period should increase with increasing thickness. The 34 nm LSCO sample discussed in Figure 4.4 did have a slightly delayed second peak, which could indicate that the beating period was increasing with the thickness. However, the differing laser alignment and addition of the cryostat for the 25 nm LSCO sample means additional studies must be done before such a conclusion can be made. Additionally, varying Sr concentration could yield interesting results for ultrafast phase transitions in complex oxides materials. Because Sr concentration plays such an important role in the spin/electronic states and transitions in LSCO, as well as the structural parameters of LSCO, different dynamics should be observed at both higher and lower levels. Above x = 0.35, LSCO is predicted to remain metallic even above the Curie temperature, whereas below x = 0.2, a low temperature insulating state exists. Because photo-excitation can also lead to the creation of new, thermally inaccessible states, ultrafast pumping of LSCO with various Sr concentrations could lead to discovery of a rich landscape of transient spin and charge states.

Bibliography

[1] J. C. Slonczewski. "Current-driven excitation of magnetic multilayers". In: *Journal of Magnetism and Magnetic Materials* 159.1-2 (1996), pp. L1–L7. ISSN: 0304-8853. DOI: 10.1016/0304-8853(96)00062-5.

[2] L. Berger. "Emission of spin waves by a magnetic multilayer traversed by a current". In: *Phys. Rev. B* 54 (13 1996), pp. 9353–9358. DOI: 10.1103/PhysRevB.54.9353. URL: https://link.aps.org/doi/10.1103/PhysRevB.54.9353.

[3] Everspin Technologies. *Spin-transfer torque DDR products, url = https://www.everspin.com/spin-transfer-torque-ddr-products, urldate = 2022-02-22.*

[4] David P Bernstein et al. "Nonuniform switching of the perpendicular magnetization in a spin-torque-driven magnetic nanopillar". In: *RAPID COMMUNICATIONS PHYSICAL REVIEW B* 83.4 (2011), pp. 180410–180411. DOI: 10.1103/PhysRevB.83.180410.

[5] E. Beaurepaire et al. "Ultrafast Spin Dynamics in Ferromagnetic Nickel". In: *Phys. Rev. Lett.* 76 (22 1996), pp. 4250–4253. DOI: 10.1103/PhysRevLett.76.4250. URL: https://link.aps.org/doi/10.1103/PhysRevLett.76.4250.

[6] A. Fognini et al. "Ultrafast reduction of the total magnetization in iron". In: *Applied Physics Letters* 104.3 (2014), p. 032402. DOI: 10.1063/1.4862476. eprint: https://doi.org/10.1063/1.4862476. URL: https://doi.org/10.1063/1.4862476.

[7] C Boeglin et al. "Distinguishing the ultrafast dynamics of spin and orbital moments in solids". In: *Nature* 465.7297 (2010), pp. 458–461. ISSN: 1476-4687. DOI: 10.1038/nature09070. URL: https://doi.org/10.1038/nature09070.

[8] N Bergeard et al. "Ultrafast angular momentum transfer in multisublattice ferrimagnets". In: *Nature Communications* 5.1 (2014), p. 3466. ISSN: 2041-1723. DOI: 10.1038/ncomms4466. URL: https://doi.org/10.1038/ncomms4466.

[9] Kohei Yamamoto et al. "Ultrafast demagnetization of Pt magnetic moment in L10-FePt probed by magnetic circular dichroism at a hard x-ray free electron laser". In: *New Journal of Physics* 21.12 (2019), p. 123010. ISSN: 1367-2630. DOI: 10.1088/1367-2630/ab5ac2. URL: http://dx.doi.org/10.1088/1367-2630/ab5ac2.

[10] Dennis Rudolf et al. "Ultrafast magnetization enhancement in metallic multilayers driven by superdiffusive spin current". In: *Nature Communications* 3 (2012), p. 1037. URL: http://www.nature.com/ncomms/journal/v3/n9/abs/ncomms2029.html.

[11] Emrah Turgut et al. "Controlling the Competition between Optically Induced Ultrafast Spin-Flip Scattering and Spin Transport in Magnetic Multilayers". In: *Physical Review Letters* 110.19 (May 2013), p. 197201. ISSN: 0031-9007. DOI: 10.1103/PhysRevLett.110.197201. URL: http://link.aps.org/doi/10.1103/PhysRevLett.110.197201.

[12] C. D. Stanciu et al. "All-Optical Magnetic Recording with Circularly Polarized Light". In: *Phys. Rev. Lett.* 99 (4 2007), p. 047601. DOI: 10.1103/PhysRevLett.99.047601. URL: https://link.aps.org/doi/10.1103/PhysRevLett.99.047601.

[13] Sabine Alebrand et al. "Light-induced magnetization reversal of high-anisotropy TbCo alloy films". In: *Applied Physics Letters* 101.16 (2012), p. 162408. ISSN: 00036951. DOI: 10.1063/1.4759109/1.4759109.MM.ORIGINAL.V1.MOV. URL: https://aip.scitation.org/doi/abs/10.1063/1.4759109.

[14] C. H. Lambert et al. "All-optical control of ferromagnetic thin films and nanostructures". In: *Science* 345.6202 (2014), pp. 1337–1340. ISSN: 10959203. DOI: 10.1126/SCIENCE.1253493/SUPPL_FILE/LAMBERT.SM.PDF. URL: https://www.science.org/doi/abs/10.1126/science.1253493.

[15] Patrick W. Granitzka et al. "Magnetic Switching in Granular FePt Layers Promoted by Near-Field Laser Enhancement". In: *Nano Letters* 17.4 (2017), pp. 2426–2432. ISSN: 15306992. DOI: 10.1021/ACS.NANOLETT.7B00052. URL: https://pubs.acs.org/doi/full/10.1021/acs.nanolett.7b00052.

[16] G. P. Zhang and W. Hübner. "Laser-Induced Ultrafast Demagnetization in Ferromagnetic Metals". In: *Phys. Rev. Lett.* 85 (14 2000), pp. 3025–3028. DOI: 10.1103/PhysRevLett.85.3025. URL: https://link.aps.org/doi/10.1103/PhysRevLett.85.3025.

[17] C. Stamm et al. "Femtosecond modification of electron localization and transfer of angular momentum in nickel". In: *Nature Materials 2007 6:10* 6.10 (2007), pp. 740–743. ISSN: 1476-4660. DOI: 10.1038/nmat1985. URL: https://www.nature.com/articles/nmat1985.

[18] K. Carva, M. Battiato, and P. M. Oppeneer. "Ab Initio Investigation of the Elliott-Yafet Electron-Phonon Mechanism in Laser-Induced Ultrafast Demagnetization". In: *Phys. Rev. Lett.* 107 (20 2011), p. 207201. DOI: 10.1103/PhysRevLett.107.207201. URL: https://link.aps.org/doi/10.1103/PhysRevLett.107.207201.

[19] K. Carva et al. "Ab initio theory of electron-phonon mediated ultrafast spin relaxation of laser-excited hot electrons in transition-metal ferromagnets". In: *Phys. Rev. B* 87 (18 2013), p. 184425. DOI: 10.1103/PhysRevB.87.184425. URL: https://link.aps.org/doi/10.1103/PhysRevB.87.184425.

[20] Spencer Jeppson and Roopali Kukreja. "Capturing ultrafast magnetization phenomenon using femtosecond x rays". In: *APL Materials* 9.10 (2021), p. 100702. ISSN: 2166532X. DOI: 10.1063/5.0054006. URL: https://aip.scitation.org/doi/abs/10.1063/5.0054006.

[21] C. Vicario et al. "Off-resonant magnetization dynamics phase-locked to an intense phase-stable terahertz transient". In: *Nature Photonics 2013 7:9* 7.9 (2013), pp. 720–723. ISSN: 1749-4893. DOI: 10.1038/nphoton.2013.209. URL: https://www.nature.com/articles/nphoton.2013.209.

[22] S. Bonetti et al. "THz-Driven Ultrafast Spin-Lattice Scattering in Amorphous Metallic Ferromagnets". In: *Phys. Rev. Lett.* 117 (8 2016), p. 087205. DOI: 10.1103/PhysRevLett.117.087205. URL: https://link.aps.org/doi/10.1103/PhysRevLett.117.087205.

[23] Matthias Hudl et al. "Nonlinear Magnetization Dynamics Driven by Strong Terahertz Fields". In: *Phys. Rev. Lett.* 123 (19 2019), p. 197204. DOI: 10.1103/PhysRevLett.123.197204. URL: https://link.aps.org/doi/10.1103/PhysRevLett.123.197204.

[24] Debanjan Polley et al. "THz-driven demagnetization with perpendicular magnetic anisotropy: towards ultrafast ballistic switching". In: *Journal of Physics D: Applied Physics* 51.8 (2018), p. 084001. ISSN: 0022-3727. DOI: 10.1088/1361-6463/AAA863. arXiv: 1711.01234. URL: https://iopscience.iop.org/article/10.1088/1361-6463/aaa863https://iopscience.iop.org/article/10.1088/1361-6463/aaa863/meta.

[25] *Magnetism*. Springer Berlin Heidelberg, 2006. DOI: 10.1007/978-3-540-30283-4. URL: https://doi.org/10.1007%2F978-3-540-30283-4.

[26] T. L. Gilbert and J. M. Kelly. "Anomalous rotational damping in ferromagnetic sheets". In: *Conf. Magnetism and Magnetic Materials* (1955), pp. 253–263.

[27] T.L. Gilbert. "A phenomenological theory of damping in ferromagnetic materials". In: *IEEE Transactions on Magnetics* 40.6 (2004), pp. 3443–3449. DOI: 10.1109/TMAG.2004.836740.

[28] D. A. Garanin. "Fokker-Planck and Landau-Lifshitz-Bloch equations for classical ferromagnets". In: *Phys. Rev. B* 55 (5 Feb. 1997), pp. 3050–3057. DOI: 10.1103/PhysRevB.55.3050. URL: https://link.aps.org/doi/10.1103/PhysRevB.55.3050.

[29] O. Chubykalo-Fesenko et al. "Dynamic approach for micromagnetics close to the Curie temperature". In: *Phys. Rev. B* 74 (9 Sept. 2006), p. 094436. DOI: 10.1103/PhysRevB.74.094436. URL: https://link.aps.org/doi/10.1103/PhysRevB.74.094436.

[30] N. Kazantseva et al. "Towards multiscale modeling of magnetic materials: Simulations of FePt". In: *Phys. Rev. B* 77 (18 May 2008), p. 184428. DOI: 10.1103/PhysRevB.77.184428. URL: https://link.aps.org/doi/10.1103/PhysRevB.77.184428.

[31] Chih Hao Hsia, Tai Yen Chen, and Dong Hee Son. "Size-dependent ultrafast magnetization dynamics in iron oxide (Fe 3O 4) nanocrystals". In: *Nano Letters* 8.2 (2008), pp. 571–576. ISSN: 15306984. DOI: 10.1021/NL072899P/SUPPL_FILE/NL072899PSI20080114_024300.PDF. URL: https://pubs.acs.org/doi/full/10.1021/nl072899p.

[32] Ryunosuke Takahashi et al. "Ultrafast demagnetization in NiCo2O4 thin films probed by time-resolved microscopy". In: *Applied Physics Letters* 119.10 (2021), p. 102404. DOI: 10.1063/5.0058740. eprint: https://doi.org/10.1063/5.0058740. URL: https://doi.org/10.1063/5.0058740.

[33] E. Olive et al. "Deviation from the Landau-Lifshitz-Gilbert equation in the inertial regime of the magnetization". In: *Journal of Applied Physics* 117.21 (2015), p. 213904. DOI: 10.1063/1.4921908. eprint: https://doi.org/10.1063/1.4921908. URL: https://doi.org/10.1063/1.4921908.

[34] *[1209.1280] Field-driven femtosecond magnetization dynamics induced by ultrastrong coupling to THz transients*. URL: https://arxiv.org/abs/1209.1280 (visited on 01/11/2022).

[35] W. R. Roach and I. Balberg. "Optical induction and detection of fast phase transition in VO2". In: *Solid State Communications* 9.9 (1971), pp. 551–555. ISSN: 0038-1098. DOI: 10.1016/0038-1098(71)90144-X.

[36] Daniel Wegkamp and Julia Stähler. "Ultrafast dynamics during the photoinduced phase transition in VO2". In: *Progress in Surface Science* 90.4 (2015), pp. 464–502. ISSN: 0079-6816. DOI: 10.1016/J.PROGSURF.2015.10.001.

[37] Amal El-Ghazaly et al. "Progress towards ultrafast spintronics applications". In: *Journal of Magnetism and Magnetic Materials* 502 (2020), p. 166478. ISSN: 0304-8853. DOI: 10.1016/J.JMMM.2020.166478.

[38] A P Ramirez. "Colossal magnetoresistance". In: *Journal of Physics: Condensed Matter* 9.39 (1997), pp. 8171–8199. DOI: 10.1088/0953-8984/9/39/005. URL: https://doi.org/10.1088/0953-8984/9/39/005.

[39] Jon A. Onrubia-Calvo, Beñat Pereda-Ayo, and Juan R. González-Velasco. "Perovskite-Based Catalysts as Efficient, Durable, and Economical NOx Storage and Reduction Systems". In: *Catalysts* 10.2 (2020). ISSN: 2073-4344. DOI: 10.3390/catal10020208. URL: https://www.mdpi.com/2073-4344/10/2/208.

[40] J. Wu and C. Leighton. "Glassy ferromagnetism and magnetic phase separation in $La_{1-x}Sr_xCoO_3$". In: *Phys. Rev. B* 67 (17 2003), p. 174408. DOI: 10.1103/PhysRevB.67.174408. URL: https://link.aps.org/doi/10.1103/PhysRevB.67.174408.

[41] TeraokaYasutake et al. "OXYGEN PERMEATION THROUGH PEROVSKITE-TYPE OXIDES". In: *http://dx.doi.org/10.1246/cl.1985.1743* 14.11 (2006), pp. 1743–1746. ISSN: 0366-7022. DOI: 10.1246/CL.1985.1743. URL: https://www.journal.csj.jp/doi/abs/10.1246/cl.1985.1743.

[42] T. Nagai, W. Ito, and T. Sakon. "Relationship between cation substitution and stability of perovskite structure in SrCoO3–δ-based mixed conductors". In: *Solid State Ionics* 177.39-40 (2007), pp. 3433–3444. ISSN: 0167-2738. DOI: 10.1016/J.SSI.2006.10.022.

[43] S. Yamaguchi, Y. Okimoto, and Y. Tokura. "Local lattice distortion during the spin-state transition in $LaCoO_3$". In: *Phys. Rev. B* 55 (14 1997), R8666–R8669. DOI: 10.1103/PhysRevB.55.R8666. URL: https://link.aps.org/doi/10.1103/PhysRevB.55.R8666.

[44] C. Zobel et al. "Evidence for a low-spin to intermediate-spin state transition in $LaCoO_3$". In: *Phys. Rev. B* 66 (2 2002), p. 020402. DOI: 10.1103/PhysRevB.66.020402. URL: https://link.aps.org/doi/10.1103/PhysRevB.66.020402.

[45] Y. H. Ren et al. "Ultrafast photoinduced reflectivity transients in doped manganite". In: *Journal of Chemical Physics* 121.1 (2004), pp. 436–440. ISSN: 00219606. DOI: 10.1063/1.1755661.

[46] M. Matsubara et al. "Ultrafast Photoinduced Insulator-Ferromagnet Transition in the Perovskite Manganite $Gd_{0.55}Sr_{0.45}MnO_3$". In: *Phys. Rev. Lett.* 99 (20 2007), p. 207401. DOI: 10.1103/PhysRevLett.99.207401. URL: https://link.aps.org/doi/10.1103/PhysRevLett.99.207401.

[47] Vincent Esposito et al. "Dynamics of the photoinduced insulator-to-metal transition in a nickelate film". In: *Structural Dynamics* 5.6 (2018), p. 064501. DOI: 10.1063/1.5063530. eprint: https://doi.org/10.1063/1.5063530. URL: https://doi.org/10.1063/1.5063530.

[48] P. Ruello et al. "Optoacoustical spectrum of the metal–insulator transition compound NdNiO3: Subpicosecond pump–probe study". In: *Physica B: Condensed Matter* 363.1-4 (2005), pp. 43–54. ISSN: 0921-4526. DOI: 10.1016/J.PHYSB.2005.03.003.

[49] A. D. Caviglia et al. "Photoinduced melting of magnetic order in the correlated electron insulator $NdNiO_3$". In: *Phys. Rev. B* 88 (22 2013), p. 220401. DOI: 10.1103/PhysRevB.88.220401. URL: https://link.aps.org/doi/10.1103/PhysRevB.88.220401.

[50] S. De Jong et al. "Speed limit of the insulator-metal transition in magnetite". In: *Nature Materials* 12.10 (2013), pp. 882–886. ISSN: 14764660. DOI: 10.1038/NMAT3718.

[51] J. Zhang and R.D. Averitt. "Dynamics and Control in Complex Transition Metal Oxides". In: *Annual Review of Materials Research* 44.1 (2014), pp. 19–43. DOI: 10.1146/annurev-matsci-070813-113258. eprint: https://doi.org/10.1146/annurev-matsci-070813-113258. URL: https://doi.org/10.1146/annurev-matsci-070813-113258.

[52] Pu-Ting Dong and Ji-Xin Cheng. "Pump–Probe Microscopy: Theory, Instrumentation, and Applications". In: *Spectroscopy*. Spectroscopy-04-01-2017 32.4 (2017), pp. 24–36. URL: https://www.spectroscopyonline.com/view/pump-probe-microscopy-theory-instrumentation-and-applicationshttps://www.spectroscopyonline.com/view/pump-probe-microscopy-theory-instrumentation-and-applicationsLK-https://www.spectroscopyonline.com.

[53] Chun Yeol You and Sung Chul Shin. "Derivation of simplified analytic formulae for magneto-optical Kerr effects". In: *Applied Physics Letters* 69.9 (1998), p. 1315. ISSN: 0003-6951. DOI: 10.1063/1.117579. URL: https://aip.scitation.org/doi/abs/10.1063/1.117579.

[54] M.N. Deeter and D. Sarid. "Magnetooptical characterization of multilayers by incident-angle analysis". In: *IEEE Transactions on Magnetics* 24.6 (1988), pp. 2470–2472. DOI: 10.1109/20.92144.

[55] Arne Vansteenkiste et al. "The design and verification of MuMax3". In: *AIP Advances* 4.10 (2014), p. 107133. ISSN: 21583226. DOI: 10.1063/1.4899186. arXiv: 1406.7635. URL: https://aip.scitation.org/doi/abs/10.1063/1.4899186.

[56] J. M. D. Coey. *Magnetism and Magnetic Materials*. Cambridge University Press, 2010. DOI: 10.1017/CBO9780511845000.

[57] Yu. V. Goryunov et al. "Magnetic anisotropies of sputtered Fe films on MgO substrates". In: *Phys. Rev. B* 52 (18 1995), pp. 13450–13458. DOI: 10.1103/PhysRevB.52.13450. URL: https://link.aps.org/doi/10.1103/PhysRevB.52.13450.

[58] Kodai Niitsu. "Temperature dependence of magnetic exchange stiffness in iron and nickel". In: *Journal of Physics D: Applied Physics* 53.39 (2020), 39LT01. DOI: 10.1088/1361-6463/ab9672. URL: https://doi.org/10.1088/1361-6463/ab9672.

[59] R Skomski. "Micromagnetic Spin Structure". In: *Spin Electronics*. Ed. by Michael Ziese and Martin J Thornton. Berlin, Heidelberg: Springer Berlin Heidelberg, 2001, pp. 204–231. ISBN: 978-3-540-45258-4. DOI: 10.1007/3-540-45258-3_10. URL: https://doi.org/10.1007/3-540-45258-3_10.

[60] Mark W. Grinstaff, Myron B. Salamon, and Kenneth S. Suslick. "Magnetic properties of amorphous iron". In: *Phys. Rev. B* 48 (1 1993), pp. 269–273. DOI: 10.1103/PhysRevB.48.269. URL: https://link.aps.org/doi/10.1103/PhysRevB.48.269.

[61] C. C. Robinson. "Longitudinal Kerr Magneto-Optic Effect in Thin Films of Iron, Nickel, and Permalloy*". In: *JOSA, Vol. 53, Issue 6, pp. 681-689* 53.6 (1963), pp. 681–689. ISSN: 0030-3941. DOI: 10.1364/JOSA.53.000681. URL: https://www.osapublishing.org/viewmedia.cfm?uri=josa-53-6-681&seq=0&html=truehttps://www.osapublishing.org/abstract.cfm?uri=josa-53-6-681https://www.osapublishing.org/josa/abstract.cfm?uri=josa-53-6-681.

[62] J M Ballantynet. "Kerr Magneto-Optic Effect in Thin Cobalt Films". In: *Journal of the Optical Society of America* 54.11 (1964), pp. 1352–1353. URL: https://opg.optica.org/view_article.cfm?gotourl=https%3A%2F%2Fopg.optica.org%2FDirectPDFAccess%2FCB495B91-4D18-4AF4-8EE22437E9A7A8E0_52515%2Fjosa-54-11-1352.pdf%3Fda%3D1%26id%3D52515%26seq%3D0%26mobile%3Dno&org=UniversityofCaliforniaDavis%28CDL%29.

[63] Geoffery Rippy et al. "X-ray nanodiffraction studies of ionically controlled nanoscale phase separation in cobaltites". In: *Phys. Rev. Materials* 3 (8 2019), p. 082001. DOI: 10.1103/PhysRevMaterials.3.082001. URL: https://link.aps.org/doi/10.1103/PhysRevMaterials.3.082001.

[64] Binzhi Li et al. "Unconventional switching behavior in La0.7Sr0.3MnO3/La0.7Sr0.3CoO3 exchange-spring bilayers". In: *Applied Physics Letters* 105.20 (2014), p. 202401. DOI: 10.1063/1.4902115. eprint: https://doi.org/10.1063/1.4902115. URL: https://doi.org/10.1063/1.4902115.

[65] Manuel Izquierdo et al. "Monitoring ultrafast metallization in LaCoO3 with femtosecond soft x-ray spectroscopy". In: *Communications Physics* 2.1 (2019), p. 8. ISSN: 2399-3650. DOI: 10.1038/s42005-019-0109-9. URL: https://doi.org/10.1038/s42005-019-0109-9.

[66] L V Nomerovannaya et al. "The influence of the Cosup3/supspin state on the optical properties of LaCoOsub3/suband HoCoOsub3/sub". In: *Journal of Physics: Condensed Matter* 16.28 (2004),

pp. 5129–5136. DOI: 10.1088/0953-8984/16/28/030. URL: https://doi.org/10.1088/0953-8984/16/28/030.

[67] Y. H. Ren et al. "Observation of strongly damped GHz phonon-polariton oscillations in $La_{0.67}Ca_{0.33}MnO_3$". In: *Phys. Rev. B* 64 (14 2001), p. 144401. DOI: 10.1103/PhysRevB.64.144401. URL: https://link.aps.org/doi/10.1103/PhysRevB.64.144401.

[68] Ian Rippy. "X-ray Nano-Diffraction Imaging and Characterization of the Nanoscale Morphology in Anionic Controlled Cobaltite Heterostructures". MS. University of California, Davis, 2-19.

[69] Guo Jiun Shu, Pei Chieh Wu, and F. C. Chou. "The spin–orbit–phonon coupling and crystalline elasticity of LaCoO3 perovskite". In: *RSC Advances* 10.70 (2020), pp. 43117–43128. ISSN: 2046-2069. DOI: 10.1039/D0RA09675J. URL: https://pubs.rsc.org/en/content/articlehtml/2020/ra/d0ra09675jhttps://pubs.rsc.org/en/content/articlelanding/2020/ra/d0ra09675j.

[70] Ahmed I. Lobad et al. "Spin-lattice interaction in colossal magnetoresistance manganites". In: *Applied Physics Letters* 77.24 (2000), pp. 4025–4027. ISSN: 00036951. DOI: 10.1063/1.1329324.

[71] Y. H. Ren et al. "Generation and detection of coherent longitudinal acoustic phonons in the La0.67Sr0.33MnO3 thin films by femtosecond light pulses". In: *Applied Physics Letters* 90.25 (2007), p. 251918. DOI: 10.1063/1.2751130. eprint: https://doi.org/10.1063/1.2751130. URL: https://doi.org/10.1063/1.2751130.

[72] A. D. Caviglia et al. "Ultrafast Strain Engineering in Complex Oxide Heterostructures". In: *Phys. Rev. Lett.* 108 (13 2012), p. 136801. DOI: 10.1103/PhysRevLett.108.136801. URL: https://link.aps.org/doi/10.1103/PhysRevLett.108.136801.

[73] Haidan Wen et al. "Electronic Origin of Ultrafast Photoinduced Strain in $BiFeO_3$". In: *Phys. Rev. Lett.* 110 (3 2013), p. 037601. DOI: 10.1103/PhysRevLett.110.037601. URL: https://link.aps.org/doi/10.1103/PhysRevLett.110.037601.

[74] M Först et al. "Spatially resolved ultrafast magnetic dynamics initiated at a complex oxide heterointerface". In: *Nature Materials* 14.9 (2015), pp. 883–888. ISSN: 1476-4660. DOI: 10.1038/nmat4341. URL: https://doi.org/10.1038/nmat4341.

[75] M. Först et al. "Multiple Supersonic Phase Fronts Launched at a Complex-Oxide Heterointerface". In: *Phys. Rev. Lett.* 118 (2 2017), p. 027401. DOI: 10.1103/PhysRevLett.118.027401. URL: https://link.aps.org/doi/10.1103/PhysRevLett.118.027401.

[76] Polina Yu. Vanina et al. “Temperature evolution of the magnetic properties of lanthanum-strontium manganites”. In: *St. Petersburg Polytechnical University Journal: Physics and Mathematics* 2.3 (2016), pp. 175–180. ISSN: 2405-7223. DOI: https://doi.org/10.1016/j.spjpm.2016.08.001. URL: https://www.sciencedirect.com/science/article/pii/S2405722316301207.

[77] S Catalano et al. “Rare-earth nickelates ¡i¿R¡/i¿ NiO ¡sub¿3¡/sub¿ : thin films and heterostructures”. In: *Reports on Progress in Physics* 81.4 (2018), p. 046501. ISSN: 0034-4885. DOI: 10.1088/1361-6633/aaa37a. URL: https://iopscience.iop.org/article/10.1088/1361-6633/aaa37a.

[78] P. Ravindran et al. “Itinerant metamagnetism and possible spin transition in LaCoO3 by temperature/hole doping”. In: *Journal of Applied Physics* 91.1 (2002), pp. 291–303. DOI: 10.1063/1.1418001. eprint: https://aip.scitation.org/doi/pdf/10.1063/1.1418001. URL: https://aip.scitation.org/doi/abs/10.1063/1.1418001.

[79] T. Henighan et al. “Generation mechanism of terahertz coherent acoustic phonons in Fe”. In: *Physical Review B* 93.22 (2016), p. 220301. ISSN: 2469-9950. DOI: 10.1103/PhysRevB.93.220301. URL: http://link.aps.org/doi/10.1103/PhysRevB.93.220301.

[80] C. Dornes et al. “The ultrafast Einstein–de Haas effect”. In: *Nature* 565.7738 (2018), pp. 209–212. ISSN: 0028-0836. DOI: 10.1038/s41586-018-0822-7. URL: http://dx.doi.org/10.1038/s41586-018-0822-7.